1-1-2007

Aspects of environmental degradation and fracture in polymer films and fibers.

Peter J. Walsh
University of Massachusetts Amherst

ASPECTS OF ENVIRONMENTAL DEGRADATION AND FRACTURE IN POLYMER FILMS AND FIBERS

A Dissertation Presented

By

PETER J. WALSH

Submitted to the Graduate School of the
University of Massachusetts Amherst in partial fulfillment
Of the requirements for the degree of

DOCTOR OF PHILOSOPHY

September 2007

Polymer Science and Engineering

UMI Number: 3289223

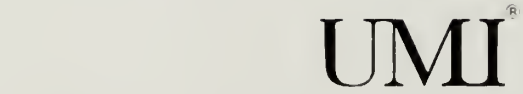

UMI Microform 3289223

ProQuest Information and Learning Company
300 North Zeeb Road
P.O. Box 1346
Ann Arbor, MI 48106-1346

ASPECTS OF ENVIRONMENTAL DEGRADATION AND FRACTURE IN POLYMER FILMS AND FIBERS

A Dissertation Presented

By

PETER J. WALSH

Approved as to style and content by:

_____
Alan J. Lesser, Chair

_____
James A. Donovan, Member

_____
Richard J. Farris, Member

_____
Shaw Ling Hsu, Department Head
Polymer Science & Engineering

ASPECTS OF ENVIRONMENTAL DEGRADATION AND FRACTURE IN POLYMER FILMS AND FIBERS

A Dissertation Presented

By

PETER J. WALSH

Approved as to style and content by:

Alan J. Lesser, Chair

James A. Donovan, Member

Richard J. Farris, Member

Shaw Ling Hsu, Department Head
Polymer Science & Engineering

DEDICATION

Kim, Katy, Dave and Josh

ACKNOWLEDGEMENTS

I would first like to thank Professor Alan Lesser for being such a great mentor during my work here at Polymer Science and Engineering. He has helped me grow as a scientist by consistently giving me freedom, encouragement and resources to try new ideas while insisting on rigorous evaluation of both idea and result. He fosters a very open, collaborative and creative atmosphere within his research group, a theme that I hope to continue in my further scientific endeavors. He has also provided me with many opportunities to present my work within the scientific community and with great patience and kindness taught me the skills of simple and effective communication.

The members of my committee, Professors James Donovan and Richard Farris have been exceptionally helpful. James Donovan has been a mentor to me since I was an undergraduate and is one of the people responsible for getting me interested in this fascinating field of materials science. His experience with environmental stress cracking has greatly improved this thesis and I am very grateful to him. Richard Farris has also given unstintingly of his time and wide experience in high performance fibers. His enthusiasm for science is often expressed in a low key but to careful listeners it is no less vital and inspiring and I thank him for his help.

I am also grateful to Professors Alan Crosby, Shaw Ling Hsu, Tom McCarthy and Ted Atkins for their help in learning the techniques of contact adhesion testing, IR spectroscopy, siloxane chemistry and diffraction physics.

Xianbo Hu, a postdoc in the Lesser Research Group, was instrumental in the work on PBO fiber and I owe him a great debt of gratitude. Other past and present Lesser

group and PS&E students I would like to thank for their assistance with research are: Manuel Garcia-Leiner, Kishore Indukuri, Donna Wrublewski, Mellisa Light, Kevin Calzia, Mohit Mamodia, Joonsung Yoon, Scott Eastman, Andrew Detwiler, Jared Archer, Kaoru Aou, C. J. Rand, Brad Seurer and Matt Misner. Ryan Murphy, Chris Forey and Doug Holmes are great to talk science with and can also make some nice music.

My acknowledgements to CUMIRP cluster M members for funding support, specifically Essilor Corporation for support of the ESC work and Natick U. S. Army Soldier Systems Center, and the International Association of Fire Fighters for support of the PBO work. MRSEC also materially assisted this research, providing great characterization facilities and knowledgeable professional staff to help with their use. Thank you John Domian, Lou Raboin, Sekar Dhanasekaran and Stephen Eyles.

None of this would have been possible without the help of the Polymer Science & Engineering admininstrative staff who have collectively solved so many problems for me in the past four years. Thank you Sophie Hsu, Anne Brainerd and especially Vivien Venskowski.

Finally I would like to thank my family for their material and emotional support through this academic journey. My father Dave did not get to see this happen but he has been with me all along. My mother Katy and stepfather Josh have been constant in providing love and support. My brothers Sam, Dennis, Liam and Brendan and sister Lorien have been wonderful. Most importantly my wife Kim who has given her love made many sacrifices and done so much to make this possible.

ABSTRACT

ASPECTS OF ENVIRONMENTAL DEGRADATION AND FRACTURE IN POLYMER FILMS AND FIBERS

SEPTEMBER 2007

PETER J. WALSH B.S., UNIVERSITY OF MASSACHUSETTS AMHERST

M.S., UNIVERSITY OF MASSACHUSETTS AMHERST

Ph.D., UNIVERSITY OF MASSACHUSETTS AMHERST

Directed by: Professor Alan J. Lesser

This thesis is focused in three areas: An investigation of a thermodynamic criterion for failure by environmental stress cracking using observations of the wetting behavior of stress-cracking liquids on glassy polymer substrates; Determination of the dominant chemical and physical degradation mechanisms associated with exposure of poly-*p*-phenylenebisbenzoxazole fiber to moisture moisture and UV-Vis spectrum light; And finally, the effect of constraint on fracture at a bi-material interface is investigated using a model epoxy-metallic adherend specimen

The wetting behavior of an ESC liquid on polycarbonate substrates has been evaluated as a function of substrate stress using a variation of Contact Adhesion Testing, a novel method of measuring small contact angles by refraction and conventional goniometry. The inelastic and elastic strain condition and time to the onset of crazing were also observed. A normalization of the time to onset of crazing using stress state,

solubility difference and diffusion coefficients was shown to collapse the kinetic observations.

A comprehensive study of the degradation mechanisms of PBO AS fiber exposed in a controlled manner to challenging chemical environments, moisture and UV-Visible spectrum light was undertaken. Fibers were characterized using a broad range of mechanical and physical tests including tensile testing, Elemental Analysis, scanning electron microscopy, small angle X-ray diffraction, wide angle X-ray diffraction and attenuated total reflectance infrared spectroscopy. Degradation by moisture is found to be primarily due to a loosening of the fiber's fibrillar structure. Degradation by UV-Visible spectrum light is found to be chemical in nature involving hydrolytic disruption of the oxazole ring and possible subsequent conversion to an amide bond.

Approaches to alleviation of PBO AS fiber degradation were studied including super-critical carbon dioxide extraction of residual acid, the use of UV-Vis blocking coatings, compaction of the fiber microstructure and PBO AS/Siloxane composites prepared in super-critical carbon dioxide.

Finally, the effect of constraint on fracture at the interface between a polymer and adherend having orders of magnitude larger stiffness was studied using a model epoxy/metallic adherend system. Fracture energy was measured using an Elastic Wedge Opened Double Cantilevered Beam test and the process zone imaged using photoelastic methods

CONTENTS

ACKNOWLEDGEMENTS v

ABSTRACT vii

LIST OF TABLES xiv

LIST OF FIGURES xvi

LIST OF SCHEMES xxv

CHAPTER

1. INTRODUCTION 1

Environmental Stress Cracking in Glassy Thermoplastics 1
Environmental Degradation of Poly-p-phenylenebenzobisoxazole Fibers 2
Stabilization of Poly-p-phenylenebenzobisoxazole Fibers 3
Fracture in Constrained Geometries 5
Dissertation Overview 6

2. ENVIRONMENTAL STRESS CRACKING IN GLASSY THERMOPLASTICS 8

Introduction 8

Background on the Phenomena of Environmental Stress Cracking 9
Elastic Criterion for Failure by ESC 10
Gent's Hypothetical Crazing Mechanism 13
Wetting behavior as an indicator of unbounded swelling 15

Experimental 18

Materials 18

Contact Adhesion Testing 18
Contact angle with respect to substrate stress observations: 18
Crazing Kinetics Under Fixed Displacement Conditions 20

Methods 21

Contact Adhesion Testing 21
Mass uptake of ESC Liquids 23
Contact Angle By Refraction 23
Contact Angle by Goniometry 29

Crazing Kinetics Under Fixed Displacement Conditions 31

Results and Discussion 33

CAT: Effect of Substrate Stress on Solid-Vapor Surface Energy 33
Evaluation of Gent ESC Criterion Using Observations of Contact Angle 37

Contact angle as an indicator of swelling.....37
Contact angle with respect to stress: Refraction.....40
Contact Angle with Respect to Stress: Goniometry 46

Strain Condition at Crazing Under Constant Stress conditions.....48
Total strain at crazing.....50
Kinetics of Crazing Under Fixed Load Conditions 52
Crazing Kinetics Under Fixed Displacement Conditions 53

Conclusions 56

3. ENVIRONMENTAL DEGRADATION OF POLY-P-PHENYLENE BENZOBISOXAZOLE FIBERS 60

Introduction 60

Potential Mechanisms of Degradation 61

Physical Mechanisms of Fiber Degradation.....62
Chemical Mechanisms of Fiber Degradation 63

Experimental 65

Materials.....65
Methods.....65

Liquid and vapor water exposure.....65
Phosphoric acid exposure.....65
UV-Visible light exposure.....66
Tensile testing.....67
Scanning Electron Microscopy.....68
ATR-FTIR.....69
SAXD, WAXD 69
Elemental analysis 69

Results & Discussion.....71

Liquid and vapor phase water exposure results.....71

Effects of Residual Phosphoric acid 77
Chemical exposure results 78
UV-Visible light exposure 80
UV-Visible light exposure/Phosphoric acid exposure 85

Conclusions 87

4. STABILIZATION OF POLY-P-PHENYLENE BENZOBISOXAZOLE FIBERS 90
Introduction 90

Super-Critical Fluid Extraction of Phosphoric Acid 91
UV-Vis Blockers 92
Compaction 92
PBO Polysiloxane composites 93

Experimental 94

Materials 94

PBO AS Fiber 94
Extraction and Neutralization of Phosphoric Acid 94
UV-Vis Blockers 95
Polymethylvinylsiloxane-polydimethylsiloxane Prepolymer (PVMS) 95
Sylgard 184 Polydimethysiloxane Resin 96
Sylgard 184 Polydimethylsiloxane Crosslinker 96

Methods 96

Super-Critical Carbon dioxide Extraction 96
Preparation of PBO AS/Crosslinked PDMS Composites in $scCO_2$ 97
UV-Vis Exposure 98
UV-Vis Spectroscopy 98
Tensile Testing 98
SEM 99
ATR-FTIR 99
SAXD 99
Elemental Analysis 99
MALDI-TOF 99
NMR 99

Results and Discussion 100

Extraction of Residual Phosphoric Acid in Super-Critical Carbon Dioxide 100
Neutralization and Extraction of Residual Phosphoric Acid 104
UV-Vis Blockers 110
Compaction of Fiber Microstructure 114

Super-critical Fluid Approach to PBO AS/Polysiloxane Composites 119

Preparation of Vinyl Substituted PVMS prepolymer 120
Polymerization of PBO AS/Crosslinked PDMS composites in $scCO_2$ 123

Conclusions 129

5. FRACTURE IN CONSTRAINED GEOMETRIES 133

Introduction 133

Background 137
Experimental approach 141

Experimental 142

Materials 142
Methods 146

Photoelastic Imaging of Process Zone 146
Determination of G_c under constant load and constant displacement conditions 149
Determination of G_c using EWODCB testing geometry 152

Stability criterion 155

Results and Discussion 158

Stability of EWODCB specimens during testing 158
Residual Stress in EWODCB specimen 159
Fracture energy from EWODCB testing 162
Photoelastic imaging of process zone 163

Conclusions 168

Relative merits of EWODCB and FPB specimens 168
Residual Stress in EWODCB specimens 169
Effect of constraint on G_c and stress distribution near the crack tip 169

6. CONCLUSIONS AND SUGGESTIONS FOR FUTURE WORK 171

ESC of Glassy Thermoplastics 171
Environmetal Degradation and Stabilization of Poly-p-phenylenebenzobisoxazole Fibers 172
Fracture in Constrained Geometries 174

APPENDICES

A. EPOXIDE CONVERSION IN INCOMPLETELY CROSSLINKED EDA/DMEDA EPOXY NETWORKS 175
B: ESTIMATE OF NOMINAL M_C 380 G/MOL NETWORK BULK PROPERTIES FROM T_G 177
C. FRACTURE ENERGY AND STABILITY CRITERION FOR FOUR POINT BEND TEST 179

BIBLIOGRAPHY 182

LIST OF TABLES

Table Page

1: Some physical properties of ESC materials 19

2: Some physical properties of materials used ESC kinetics observations 21

3: Estimate of maximum error (E_{max}) and uncertainty (U) in contact angle for oleic acid-polycarbonate system. Probable limiting precision of the refraction technique approximately ±0.5°. 28

4. Polycarbonate-dibutyl phthalate data for contact angle with respect to spherical component of stress. Angles are the mean of three observations on separate samples observed by video goniometer. 47

5. Polycarbonate-oleic acid data for contact angle with respect to the spherical component of stress acting on the sample. Angles are the mean of three observations observed using a video goniometer. 48

6: Results of Guinier plot and SAXD analysis for liquid water exposed PBO fiber. The increase in the average cross sectional area (S3) of the voids suggests a loosening of the fibrillar bundle on exposure to water 75

7: Results of Guinier plot and SAXD analysis for PBO AS fiber exposed to UV-Visible light. 84

8: Weight percentage of residual phosphorus remaining in PBO AS fiber washed in $scCO_2$ under varying conditions of temperature, pressure 101

9: Change in equatorial and meridonal Guinier correlation length with increasing $scCO_2$ fluid pressure for PBO AS/vinyl substituted prepolymer PDMS composites fabricated in $scCO_2$ 125

10: Change in equatorial and meridonal Guinier correlation length with increasing $scCO_2$ fluid pressure for PBO AS/Sylgard 184 PDMS Composites fabricated in $scCO_2$ 127

11: Structures and molecular weights of monomers used in the DGEBA/EDA/DMEDA epoxy system. 143

12: Bulk properties, and estimated plastic zone radius. of bisphenol-A/EDA/DMEDA epoxy systems with postcure at Tg + 50 K according to molecular weight between

crosslinks [[a]161], and estimated bulk properties and plastic zone radius of partially cured bisphenol-A/EDA/DMEDA networks [[b]155,156,157].....146

13: Estimate of hydrostatic tension due to change in volume during cure using adherend deflection at L/2 for a population of 1.5mm and 3.25mm thick Mc380 g/mol EDA epoxy EWODCB specimens. L/2 deflection standard deviations given in parenthesis 161

14: Epoxide conversion in Mc 380 g/mol EDA/DGEBA epoxy network with respect to curing temperature. The % epoxide conversion is calculated based on FTIR spectra of an unreacted mixture of EDA and DGEBA and networks crosslinked at varying temperatures [162].....176

LIST OF FIGURES

Figure Page

1: Schematic of Sternstein's crazing criterion. The spherical component of stress increases mobility and the stress bias term promotes orientation [64].....12

2: Plot of Gent's generalization of the Flory-Huggins equilibrium swelling relationship 15

3: Caskey's preliminary data for contact angle as a function of stress. The oleic acid/polycarbonate system shows a drop in angle with increasing stress [70].....17

4: Sessile drop force balance.....17

5: Gent hypothesis prediction of critical stress for unbounded swelling. (A) polycarbonate/oleic acid and (B) polycarbonate/dibutyl phthalate.....20

6: Schematic of JKR theory based Contact Adhesion Test used to measure effect of uniaxial stress on solid-vapor surface energy. 22

7: Schematic of refraction geometry showing refraction of incident LASER through sessile drop lens and substrate material. 26

8: Schematic of refraction device showing tensile sample, sessile drop, means of applying load, environmental enclosure, detector and LASER source.....27

9: (A) Oleic acid/polycarbonate refraction pattern showing measurands Z_α, and Z_β. (B) Reflectance mode optical micrograph of oleic acid/polycarbonate sessile drop edge viewed from above. 27

10: A) Refraction image prior to the onset of crazing. B) Refraction image after onset of crazing. Diffraction fringes in refraction image indicate growth of craze to a length scale commensutrate with the 632 nm wavelength LASER.....29

11: Video goniometer images showing application of oleic acid to polycarbonate substrate and the advance and recession of the three-phase line.....30

12: Plot of contact angle wrt to time for a fixed uniaxal strain oleic acid-polycarbonate sample. Note plateau of equilibrium advancing angle during $16s<t<25s$ interval. Advancing angles are taken as the average of the plateau region for three separate samples.....31

13: Two-Point bending jig for fixed strain ESC testing. Maximum strain at midpoint is calculated using Equation 14 [80].....32

14: Load-displacement curves for polycarbonate-polydimethylsiloxane contact during Contact Adhesion Testing. Polycarbonate substrate is at zero strain. Large degree of hysteresis and large maximum pull-off force indicates relatively large adhesion forces.....34

15: Images of contact area for polycarbonate-polydimethylsiloxane during Contact Adhesion Testing. (A) maximum contact area. The lack of interference fringes at the perimeter indicates that the PDMS suface ia approximately normal to the PC substrate material as in the diagram to the left. (B) composite of contact areas during loading and unloading.....35

16: Work of adhesion (W_{adh}) and critical energy to create surface (G_{crit}) vs. spherical component of stress for contact between a uniaxially stressed polycarbonate substrate and a PDMS hemisphere. Both quantities indicate that the energy release rate and hence the interfacial energies acting on the PC substrate are independent of substrate stress.....35

17: Load-displacement curves for PC-PC contact during Contact Adhesion Testing. Polycarbonate substrate is at zero strain. The small magnitude of hysteresis and small maximum pull-off force indicate very low adhesive forces between the surfaces. 36

18: Images of contact area for polycarbonate-polycarbonate contact during Contact Adhesion Testing. (A) maximum contact area. The presence of interference fringes indicates tangent-tangent interface at the contact area perimeter as in the diagram to the left. (B) composite of contact areas during loading and unloading. Distortion of the hemispherical probe is due to swelling during the solution casting of the polycarbonate coating.....36

19: Plot of solid-vapor surface energy with respect to the spherical component of stress of a uniaxially loaded polycarbonate sample as determined from Contact Adhesion Testing. Small degree of adhesion for polycarbonate-polycarbonate contact increases the variability of surface energy determined from GJKR and WADH. Surface energy derived from GCrit is similar to that measured using conventional contact angle studies (42 mJ/m2). GCrit is taken as the most appropriate indicator and shows that γSV is constant with increasing stress.....37

20: Mass uptake for polycarbonate in dibutyl phthalate. At ~8% solvent uptake the PC sample lost physical integrity and could no longer be weighed accurately.....38

21: Plot of mass uptake with respect to time for polycarbonate immersed in oleic acid. The data indicates that no significant amount of oleic acid is absorbed during the 70 day duration of the observation. The PC sample remained optically clear throughout the observations.....39

22: Static contact angle with respect to time for a sessile drop of dibutyl phthalate on a polycarbonate substrate. Strong decay with time is due to spontaneous swelling of substrate. Each data point is the mean of five observations and the error bars indicate one standard deviation on the mean. 39

23: Plot of contact angle with respect to time for a sessile drop of oleic acid on a polycarbonate substrate. No significant decay in contact angle with time is observed. Each data point is the mean of five observations and the error bars indicate one standard deviation on the mean. 40

24: Initial and equilibrium contact angle as a function of spherical stress for dibutyl phthalate on a polycarbonate substrate. 41

25: Contact angle as a function of spherical stress for oleic acid on a polycarbonate substrate. Each data point is the mean of five samples and the error bars indicate 1 standard deviation on the mean. The data show a weak trend toward a minima at ~7MPa spherical stress but given the magnitude of error contact angle must be considered approximately constant with substrate stress. 42

25: Plot of contact angle with respect to relative humidity for polycarbonate/oleic acid. Three phase line advances as humidity increases and recedes as humidity drops. 44

26: Advancing and receding refraction images from Figure 2.23 observations of advance and recession of three-phase line driven by vapor phase relative humidity. Advancing β-refraction spot shows that the advancing three-phase line is more uniform than the receding three-phase line. 45

27: Contact angle hysteresis of polycarbonate/oleic acid driven by cycled relative humidity. Magnitude of contact angle hysteresis is on the order of 2° and is constant with substrate stress. 45

28: Advancing contact angle as a function of spherical stress for a polycarbonate-dibutyl phthalate sample under fixed displacement uniaxial tension. Angles are the mean of three observations on separate samples observed by video goniometer. 46

29: Advancing contact angle as a function of spherical stress for a polycarbonate-oleic acid sample under fixed displacement uniaxial tension. Angles measured by video goniometer. The filled squares denote the mean of three observations and the error bars indicate 1 standard deviation on the mean. There is a trend to a minima at ~15 MPa but given the precision of this method, usually considered to be ±2-5°, the data do not indicate the Gent hypothesis transition to unbounded swelling. 47

30: A) Refraction image prior to the onset of crazing. B) Diffraction fringes in refraction image indicate growth of craze to a length scale commensutrate with the 632 nm wavelength LASER. 49

31: Fixed uniaxial load strain response of polycarbonate samples used in contact angle-stress observations, time to craze initiation and strain at crazing experiments. Labels indicate the spherical component of stress acting on the tensil specimen. For the 1800 second duration of the experimental observations substrate creep is significant only for spherical stresses above 9MPa. 49

32: overall strain at crazing for oleic acid-polycarbonate and dibutyl phthalate-polycarbonate samples. 51

33: Inelastic component of strain for oleic acid-polycarbonate and dibutyl phthalate-polycarbonate samples. 51

34: Time to onset of crazing for polycarbonate-oleic acid and polycarbonate-dibutyl phthalate systems. Crazing indicated by appearance of diffraction fringes. 52

35: Plot of spherical stress on a PC substrate normalized by the square of the solubility difference between ESC liquid and polymer plotted vs the time to initiation of crazing under fixed displacement loading in a two point bend test. The $\sigma ii/(\Delta\delta)2$ term is representative of the thermodynamic potential for swelling. The plot shows that in addition to thermodynamic potential, the size of the ESC liquid molecule is an important factor in crazing kinetics. A large molecule at high swelling potential crazes in a similar time as a smaller molecule at lower swelling potential. 54

36: Estimate of the relationship of diffusion coefficient to the ratio of physical crosslink molar volume (V_m^P) and ESC liquid molar volume (V_m^S). A power law fit indicates that diffusion coefficient varies roughly in proportion to $(VmP/ VmS)^{5.8}$. 55

37: Plot of $(V_m^P/V_m^S)^{5.8} \bullet \sigma_{ii}/(\Delta\delta)^2$ with respect to time to crazing for a homolgous series of ESC liquids on a polycarbonate substrate. 55

38: Irradiation spectrum of the Suntest CPS + weatherometer used in PBO fiber degradation studies. 66

39: Instron 5800 system compliance (C_s). Determined from a plot of the initial slope of the fiber force displacement curve with respect to fiber gauge length normalized by cross sectional area. Ten PBO AS fiber samples were tested at each gauge length (20mm, 40mm, 60mm, 80mm. 100mm, 120 mm and 150mm) The intercept of the line is Cs (1.152x10-4 m/N) and the slope is 1/E for the as received PBO AS fibers tested (E≈196 GPa). 68

40: Tensile data for PBO fiber exposed to liquid water and 90% relative humidity at 50°C 74

41: SEM micrographs: (A)PBO AS control, (B)PBO AS fiber exposed to liquid water (C) PBO AS fiber exposed to 90% relative humidity. 74

42: SAXD diffraction pattern and Guinier plot for PBO fiber exposed to liquid water....75

43:ATR-FTIR spectra for PBO fiber exposed to liquid water. There is no significant alteration of the chemical structure at or near the surface of the fibers. Spectra of fiber exposed to water vapor showed similar results.....76

44: WAXD results for PBO AS fiber exposed to liquid water showing no effect on the crystalline structure of the fiber. Peaks in the diffraction have been assigned according to the work of Fratini et al. [92].....77

45: Tensile testing results for PBO fiber at 24 hour exposure to increasing concentrations of aqueous phosphoric acid solution. 79

46: SEM results for PBO fiber exposed to 1.8M phosphoric acid. 80

47: ATR-FTIR results for PBO Fiber exposed to increasing concentrations of phosphoric acid.....80

48: Tensile testing results for three series of PBO AS fiber exposed to UV-Vis light at an intensity of 750 W/m2. Error bars on modulus indicate one standard deviation about the mean value. 83

49: SEM results for UV-Visible light exposed PBO AS fiber.....83

50: ATR-FTIR results for UV-Vis exposed PBO AS fiber. 84

51: Mechanical properties of phosphoric acid exposed PBO AS fibers with UV-Visible light.....86

52: Schematic of device used for super-critical CO_2 extraction of residual phosphoric acid.....97

53: Schematic of the device used in preparing PBO AS/Crosslinked PDMS composites in a super-critical carbon dioxide environment. The high-pressure reaction vessel is removed after pressurization with CO2 and placed in an oven to maintain temperature and pressure above the critical point. 98

54: Tenacity of PBO AS fibers washed with scCO2 at 5 LPM flow rate and varying conditions of temperature and pressure compared to pristine control fiber. Whiskers denote minimum and maximum, box denotes median and standard deviation and the open diamond denotes the mean.....102

55: SEM of scCO2 washed PBO AS fiber (A) compared to control fiber (B).....103

56: Tenacity of scCO2 washed PBO AS fibers exposed to UV-Vis light at 750 W/m^2 compared to pristine control fiber. 103

57: Comparison of initial tenacity for control PBO AS fiber and fiber treated with trimethyl phosphate (TMP), pyridine (PYR) and morpholine (MOR). Whiskers denote minimum and maximum, box denotes median and standard deviation and the open diamond denotes the mean. 106

58: Tensile testing results for PBO AS fibers treated with pyridine, morpholine and trimethyl phosphate. 106

59: Tensile testing results for PBO AS fibers treated with pyridine in an scCO2 environment 107

60: ATR-FTIR spectra of PBO AS fibers treated with phosphoric acid, pyridine, morpholine and trimethyl phosphate compared to spectra of pristine fibers and water exposed fibers 109

61: SEM of (A) graphite and (B) carbon black coated PBO AS fibers. 111

62: Tensile testing results for carbon black, graphite and TiO2 coated fibers exposed to UV-Vis light. 113

63: UV-Vis absorption of TiO_2 sol-gel and dried glassy TiO_2 film. 113

64: SEM of TiO_2 coating showing a thin film with thickness on the order of ~100's of nanometers. 114

65: Tensile testing results showing effect of twist on fiber tenacity. Error bars indicate 1 standard deviation on the mean. 117

66: Tensile testing results showing effect of hydrostatic pressure on fiber tenacity 118

67: SEM micrographs of PBO AS fiber surfaces after compaction in $scCO_2$ and silicon oil. 118

68: Tensile testing results showing effect comparing the tenacity of untreated PBO AS fiber with PBO AS fiber held at 40cN tension and PBO AS fiber held at 40 cN tension and soaked in a sub-critical CO_2 environment under 5000 psi hydrostatic pressure. Error bars indicate 1 standard deviation on the mean 119

69: NMR spectra of vinyl substituted PDMS prepolymer. Peaks near 6 ppm shift are associated with vinyl protons, peaks near 0 ppm are associated with methyl protons. Integration indicates a 13.5:1 ratio of dimethyl siloxane repeats to methylvinyl siloxane repeats. Peak near 1.5 ppm is water 122

70: MALDI-TOF molecular weight distribution for vinyl substituted PDMS prepolymer. M_n is 1003 g/mol. 123

71: SAXD diffraction pattern for PBO AS control fibers compared to PBO AS/crosslinked PVMS composites fabricated in $scCO_2$ 125

72: SAXD diffraction pattern for PBO AS control fibers compared to PBO AS/Sylgard 184 PDMS composites fabricated in $scCO_2$ 126

73: SEM micrographs of PBO AS control fiber surfaces 127

74: SEM micrograph of PBO AS control fiber kink bands 128

75: SEM micrograph of PBO AS fiber surfaces after soaking and crosslinking of PVMS monomer in $scCO_2$ environment. P=1500 psi, T=50 C. 128

76: SEM images of PBO AS fiber kink band after soaking and crosslinking of Sylgard 184 PDMS in $scCO_2$ environment. P=1500 psi, T=50 C. 128

77: Photoelastic image showing the process zone of a crack propagating through a bulk thermoplastic [148] 135

78: Schematic of fracture process zone at a bi-material interface 136

79: Kinloch's results for energy release rate with respect to adhesive thickness for a ductile rubber toughened epoxy (circles) and brittle epoxy (squares) adhesives with aluminum adherend boundaries [146]. 138

80: Qualitative effect of bond thickness on the plastic zone size of a crack propagating in an adhesive layer proposed by Kinloch et. al. [140,150], figure after Ikeda [151] 138

81: Schematic of the effect of constraint on plastic zone volume. Imposing constraint on material movement at the adherend boundary causes a stress concentration. As the stiff boundary approaches the length scale of the unperturbed process zone further stress concentration occurs and a larger volume of material near the crack tip yields. 139

82: Ikeda's determination of distribution of plastic zone around crack tip from FEM and BEM methods [147]. 140

83: Elastic Wedge Opened Double Cantilever Beam (EWODCB) Specimen. DGEBA/EDA/DMEDA epoxy is cured between metallic adherends separated by PTFE spacers. The free surfaces of the epoxy are covered with glass plates during cure to give a smooth molded surface. 143

84: Schematic of a plane polariscope [164]. 148

85: Schematic of a circular polariscope [164].....148

86: Simulation of isochromatic fringes around a crack tip for mode I, mode II and mixed mode fracture [165].....149

87: Schematic of Load-Displacement curves for linear-elastic crack propagation under (A) constant load and (B) constant displacement conditions.....151

88: Elastic Wedge Opened Double Cantilevered Beam test used to determine critical energy release rate (G_c) of a bi-material interface under constant displacement conditions. 154

89: Four Pont Bend Test specimen consisting of two stiff adherends separated by a polymer interlayer. One of the adherends is notched at the midpoint and a pre-crack is incorporated using a release film.....157

90: Force displacement curve recorded during EWODCB test showing the plateau in force when crack propagation has reached a steady state.....158

91: Estimation of hydrostatic tension present in EWODCB specimens due to contraction during cure at elevated temperature using adherend deformation. 161

93: Plot of G_c with respect to the ratio t/r_p as measured using the EWODCB specimen based on nominal molecular weight between crosslinks of 380 g/mol and 818 g/mol ..163

94: Circular polariscope images of the distribution of distortional stress around propagating crack tip for M_c=380 g/mol EDA epoxy system with varying thickness bondlines ($0.7<t/rp<8.3$). The crack is propagating from the lower left corner of each image. The crack tip region is indicated by white arrows. 165

95: Plane polariscope images of the distribution of disortional stress around propagating crack tip for M_c=380 g/mol EDA epoxy system with varying thickness bondlines ($0.7<t/rp<8.3$). The crack is propagating from the lower left corner of each image arrows show direction of polarizer and analyzer axes. 165

96: Circular polariscope images of the distribution of distortional stress around propagating crack tip for M_c=818 g/mol DMEDA epoxy system with varying thickness bondlines ($2<t/rp<12.5$). The crack is propagating from the lower left corner of each image.....167

97: Plane polariscope images of the distribution of disotrtional stress around propagating crack tip for M_c=818 g/mol DMEDA epoxy system with varying thickness bondlines ($2<t/rp<12.5$). The crack is propagating from the lower left corner of each image.....167

98: Curve fit of the epoxide conversion data from Table 14 176

99: Correlation of compressive yield stresses and glass transition temperatures for a series of EDA/DMEDA/DGEBA networks with varying crosslink densities [156,158,161]...178

100: Four Pont Bend Test specimen consisting of two stiff adherends separated by a polymer interlayer. One of the adherends is notched at the midpoint and a pre-crack is incorporated using a release film.....179

101: Free body diagram and bending moment diagram of Four Point Bend Test specimen. 181

LIST OF SCHEMES

Scheme Page

1. Polycondensation of a 1,3-diamino-4,6-dihydroxybenzene dihydrochloride (DADHB) and terephtrhalic acid (PTA) phosphoric acid solution to form PBO polymer.....62

2. Preparation of low MW vinyl substituted siloxane prepolymer.....96

3. pKa values for dissociation of phosphoric acid protons.....100

4. Small molecules used to treat PBO AS fibers: pyridine, morpholine and trimethylphosphate.....105

5. Preparation of PBO AS/crosslinked PDMS Composites in $scCO_2$ environment.....120

CHAPTER 1

INTRODUCTION

Environmental degradation and fracture are critical issues for the use of polymer materials in a wide variety of applications from thermoplastic engineering components to micro-electronics devices and packaging to high performance textiles and composites. Within this broad subject area the research described here is focused in three areas: An investigation of a thermodynamic criterion for failure by environmental stress cracking using observations of the wetting behavior of stress-cracking liquids on glassy polymer substrates; The dominant chemical and physical degradation mechanisms associated with exposure of poly-*p*-phenylenebisbenzoxazole fiber to moisture and solar radiation have been determined and approaches to alleviation of fiber degradation formulated and tested. Finally, the effect of constraint on fracture at a bi-material interface is investigated using a model epoxy-metallic adherend specimen in which the relative dimensions of the adhesive thickness and process zone can be manipulated, fracture energy measured and process zone observed.

Environmental Stress Cracking in Glassy Thermoplastics

Environmental Stress Cracking or ESC is one of the leading causes of premature in service failure for engineering components made of thermoplastics [1, 2]. Although there are empirical models to predict failure [3-6] there is no generalized mechanism describing the physics of ESC. This research explores a hypothetical crazing mechanism proposed by Alan Gent [7] that relates a critical stress for swelling to the difference in cohesive energy density between the polymer and an ESC liquid. Gent's mechanism is

interesting in that it at least qualitatively captures many of the phenomena observed during failure by ESC and is based on thermodynamic considerations. This is significant because ESC is a kinetic event; once a polymer is exposed to environmental conditions favorable to ESC long periods of time may pass prior to failure. At the present the most common industrial screening tests for ESC involve observations over these long time scales. If the critical swelling stress embodied in Gent's hypothesis can be observed using a thermodynamic indicator such as wetting behavior of the ESC liquid there is the potential to use it as the basis of a short time-scale screening test for polymer-liquid pair susceptibility to ESC.

This thesis investigates the wetting behavior of ESC liquids on polycarbonate substrates as a function of substrate stress state. An accurate and objective technique for measuring small contact angles using the refraction of light has been developed. The elastic and inelastic strain conditions at crazing and the time to crazing were also observed. A change in inelastic strain response at stress levels commensurate with the Gent hypothesis critical stress and a normalization of the time to crazing by solubility difference and diffusion coefficient are presented and discussed.

Environmental Degradation of Poly-p-phenylenebenzobisoxazole Fibers

Poly-p-phenylenebenzobisoxazole (PBO) is one of a family of lyotropic liquid crystalline polymers that orient easily into extended chain configurations producing fibers with excellent strength and modulus. This class of materials including poly-p-phenylene terepthalamide (Aramid) and poly-p-phenylenebenzobisthiazole (PBZT) was originally developed to replace metals in space and aviation applications for its excellent, thermal stability and chemical resistance [8,9]. At this time they are the strongest commercially

available organic polymeric fibers [10-12]. Research and development into the morphology [13-15]and structure-property relationships of PBO and similar materials was actively pursued throughout the 1980's [16-19] . More recently research for specific applications of PBO fiber in high-performance composites, protective garments, and personnel ballistic armors has been undertaken [20, 21]. In late 2001, Toyobo Corporation, the manufacturer of PBO Fiber, published some disconcerting results regarding the susceptibility of the material to degradation when exposed to relatively mild conditions of moisture, temperature and ultra-violet/visible light spectrum radiation [12]. Subsequently, news reports reiterating these concerns in PBO products have been reported [22]. There has not previously been a great deal of research into the specific degradation mechanisms of PBO fiber due to UV-Visible spectrum light and moisture [23, 24] though thermal degradation pathways have been well studied [25-27]

This thesis discusses the chemical and physical processes of PBO fiber degradation by chemical environments, moisture and UV-Visible light spectrum radiation.

Stabilization of Poly-p-phenylenebenzobisoxazole Fibers

Fibers made from this class of lyotropic liquid crystalline polymers are typically spun from an acid solution, coagulated in a water bath and subsequently heat treated to compact and increase order in the the fiber structure which is generally an interconnected fibrillar network with fibril diameters on a length scale of 10's of nm [28-30].

Previous work in the degradation of aramid fiber by Morgan has focused on the role of residual acids remaining after the spinning process [31-33]. It has been assumed that residual phosphoric acid in PBO fiber combined with aqueous conditions may cause

hydrolytic degradation and chain scission similar to that proposed by Morgan in Kevlar fibers. The conjugated chemical structure of the PBO mer may be intrinsically susceptible to degradation by UV-Vis spectrum radiation [34]. Fiber strength is often dominated by the number and size of defects present in the fiber [35]. The axially oriented needlike voids contained in the interconnected fibrillar network morphogy of PBO represent preferential sites for fracture initiation. In addition the chemical structure of the PBO backbone is such that there are only weak inter-fibrilar and inter-chain forces. Compaction of fibrillar structure and increase in the load transfer between fibrillar elements should have a positive impact on fiber tenacity.

In this thesis several approaches to densify the fiber microstructure were undertaken. The first involves applying a twist to single fibers. A second approach is to apply hydrostatic pressure to the fiber in an $scCO_2$ environment with the intent to compact the fiber microstructure and allow the plasticizing ability of scCO to aid in the reduction of defects. Finally fibers were exposed to high temperature, tension and hydrostatic pressure in a $scCO_2$ environment simultaneously.

Prevention of swelling of the PBO AS fiber by moisture and maintenance of externally imposed compaction of the fiber morphology may have the effect of increasing the fiber's initial tenacity and resistance to degradation by moisture. The introduction of inter-fibrillar stabilizing forces has previously been studied with the aim of improving the low transverse mechanical properties of lyotropic LC rigid rod polymers; Approaches include infiltration of the fiber with a high modulus glassy filler [36, 37], infiltration with an organic polymer phase during the coagulation step of the spinning process [38], creation of an interpenetrating rigid rod fibril-amorphous polymer network by spinning a

fiber from a solution containing both a LC rigid rod polymer and an amorphous organic polymer [39, 40] and cross-linking the material in adjacent fibrillar regions using heat [41, 42].

The work undertaken in this thesis is directed at improving the environmental stability of PBO AS fiber by introduction of inter-fibrillar adhesive forces. The thesis work has been primarily pointed toward post-spinning processes applicable to stabilization of commercially produced PBO fiber. Toward this end composites of PBO AS fiber and polysiloxanes crosslinked in a hydrosilation reaction have been prepared in super-critical carbon dioxide environment. Changes in the fiber morphology are evaluated and discussed.

Fracture in Constrained Geometries

The effect of constraint on the fracture behavior of a bi-material interface is relevant to the design of structural adhesives and bond geometries, composite materials and the fabrication of robust microelectronics devices and packaging in which thin laminates with alternating layers of glassy inorganic oxides, ductile metals and polymers are common [43]. A great deal of work has been done within the context of structural adhesives looking at the effects of bond-line thickness on mode I fracture for cracks propagating within the adhesive layer [44-48] but little work has been done to directly examine the effects of inter-layer thickness on a cracks propagating at the bi-material interface.

This thesis evaluates the effect of process zone constraint on the fracture energy and stress distribution of a crack propagating at a bi-material interface. A model epoxy/metallic adherend sample has been developed that allows manipulation of the ratio

of bondline thickness to plastic zone radius and the strength of the polymer-metal interface. The critical energy release rate is measured relative to the ratio of plastic zone radius to bondline thickness using an Elastic Wedge opened Double Cantilevered Beam sample and testing procedure. The process zone of the propagating crack is imaged during the EWODCB test using photoelastic methods to qualitatively evaluate the effect of constraint on the fracture mode mixity and process zone volume and shape.

Dissertation Overview

In Chapter 2 the wetting behavior of ESC liquids on polycarbonate substrates have been investigated as a function of substrate stress. A variation of Contact Adhesion Testing (CAT) has been used to evaluate the effect of substrate stress on the solid-vapor surface energy. Contact angle and contact angle hysteresis have been evalauated as function of substrate stress and an accurate and objective method of measuring very small contact angles using refraction of light has been developed. In addition the elastic strain, inelastic strain, and time at the onset of crazing have been observed. The observations of crazing times has been combined with estimates of diffusion coefficients of ESC liquids to normalize the kinetic response of each ESC liquid/Polymer pair using stress state, solubility difference between the ESC liquid and polymer and diffusion coeficient.

In Chapter 3 the chemical and physical processes of PBO fiber degradation by chemical environments, moisture and UV-Visible light spectrum radiation are studied. PBO AS fibers were exposed to challenging chemical environments, moisture and UV-Visible spectrum radiation in a controlled manner. Fiber properties structure and composition were then characterized using a characterized using a broad range of mechanical and physical tests including tensile testing, Elemental Analysis, scanning

electron microscopy, small angle X-ray diffraction, wide angle X-ray diffraction and attenuated total reflectance infrared spectroscopy. The probable pathways of degradation by moisture and UV-Vis light are presented.

Chapter 4 describes some approaches to environmental stabilization of PBO fiber including super-critical carbon dioxide extraction and neutralization of residual phosphoric acid left in the fiber by the spinning process. The mechanical response of so treated fibers is evaluated and discussed. A number of UV-Vis blockers have been used including exfoliated graphite, carbon black and glassy titanium dioxide prepared using sol-gel chemistry have been evaluated. Compaction of the fiber microstructure to decrease the number and size of defects was undertaken using twist, hydrostatic pressure in an $scCO_2$ environment and combined hydrostatic pressure, tension and heat. The effects on the mechanical properties are presented Composites of PBO AS fiber and polysiloxanes crosslinked in a hydrosilation reaction have been prepared in super-critical carbon dioxide environment. Evidence of changes in the fiber morphology due to infiltration by the siloxane polymer are presented and discussed.

Chapter 5 describes the effect of constraint on the interfacial fracture response of a model metallic adherend/epoxy system. The critical energy release rate for fracture was evaluated using an Elastic Wedge Opened Double Cantilever Beam specimen geometry. The size and shape of the process zone around the propagating crack tip was evaluated using photoelastic methods. Results for a brittle epoxy interlayer and a more ductile epoxy interlayer are presented and discussed relative to previous work exploring the effect of constraint on fracture within a polymer interlayer.

CHAPTER 2

ENVIRONMENTAL STRESS CRACKING IN GLASSY THERMOPLASTICS

Introduction

Environmental Stress Cracking or ESC is one of the leading causes of premature in service failure for engineering components made of thermoplastics. Although there are empirical models to predict failure there is no generalized mechanism describing the physics of ESC. This research explores a hypothetical crazing mechanism proposed by Gent [49] that relates a critical stress for swelling to the difference in cohesive energy density between the polymer and an ESC liquid. Gent's mechanism is attractive in that it predicts many of the phenomena observed during ESC and is based on thermodynamic considerations. This is significant because ESC is a kinetic event; once a polymer is exposed to environmental conditions favorable to ESC long periods of time may pass prior to failure. At the present the most common industrial screening tests for ESC involve observations over these long time scales. If the critical swelling stress embodied in Gent's hypothesis can be observed using a thermodynamic indicator there is the potential to use it as the basis of a short time scale screening test for polymer-liquid pair susceptibility to ESC. One potential thermodynamic indicator of the solid-liquid interaction is wetting of the ESC liquid on the polymer substrate.

In this work the wetting behavior of ESC liquids on a polymer substrate has been observed as a function of the stress acting on the polymer substrate. The effect of substrate stress on the solid-vapor surface energy of the polymer substrate has been observed using a variation of JKR based Contact Adhesion Testing (CAT). Three-phase contact angle and contact angle hysteresis of the ESC liquid-polymer substrate pair has

been measured using both conventional goniometry methods and a new technique involving the refraction of light through a sessile drop of the challenging ESC liquid. Comparison of mass uptake experiments and observations of contact angle were used to test the effectiveness of contact angle as a metric for swelling. In addition the elastic and inelastic strain condition at the onset of crazing and the time at the onset of crazing were observed.

Background on the Phenomena of Environmental Stress Cracking

Failure by ESC is characterized by the development of crazes or planar regions of highly elongated, sometimes porous material oriented perpendicular to the direction of stress. Crazing can occur in dry polymers but the majority of failures involve amorphous or partially amorphous polymers at service temperatures below the glass transition temperature (T_g), and in contact with relatively low molecular weight liquids. The stress level at the initiation of crazing is well below the bulk yield stress of the polymer material and once a craze has formed it will become an initiation site for subsequent brittle fracture. Common stress cracking liquids include oils, fatty acids, surfactants, plasticizers, paints and adhesives. In most cases of failure by ESC there is some component of tensile stress associated with the loading of the polymer material.

Formation of a craze involves a localized transition of the material response from elastic to shear flow. The material within the craze may contain a large volume fraction of voids or simple be a region of highly drawn material [50]. In cases where voids are present cavitation occurs at an early stage and the length scale of that cavitation is thought to be ~30 nm [51]. The thickness of a craze near the tip is approximately 1000 nm and the total thickness of a craze varies with polymer material and stress cracking

liquid, but is typically on the order of 10-100 um [51]. In the majority of cases crazing does not result in chemically degraded material though chain scission has been observed insome environments [52].

While the exact mechanism of ESC is not known it is thought to be a surface initiated phenomenon in which localized flaws on the polymer surface act as initiation sites. In the presence of an ESC liquid both plasticization and decrease in the surface energy associated with cavitation can be expected to make the formation of a craze more thermodynamically favorable [53]. It is also known that crazing has both stress-time and temperature-time dependence. Increased stress and increased temperature will both reduce the time to failure [51]. As the molecular weight of the polymer is increased resistance to ESC increases [54], and orientation of the polymer tends to encourage craze growth such that the craze plane is parallel to the axis of orientation [50].

Elastic Criterion for Failure by ESC

Because ESC is such a prevalent industrial problem there has been a great deal of work in developing models to predict the ESC response of polymer-liquid pairs. Kambour's extensive work evaluating the plasticizing potential of the liquid and a critical level of strain to initiate polymer flow shows good correlation between critical strain and the Hildebrand solubility parameter of the liquid but it does not describe the physical mechanisms of ESC [55,56,57]. Despite this shortcoming, Kambour's technique, in which a specimen is bent over an elliptical strain jig and immersed in a series of challenge liquids, is at present the most commonly used industrial test for ESC. This is an effective screening technique however it does require that samples be exposed to the challenge liquid for long periods of time. Hansen and Wyzgoski have similarly related

the critical strain for crazing to the relative energy density of the polymer liquid pair and applied the two-dimensional Hansen solubility parameter approach to account for liquid-polymer pairs with dispersion, dipole, and hydrogen bonding interactions and mixtures of ESC liquids [58,59,60]. Arnold has suggested that critical inelastic strain, which is said to describe longer time scale segmental relaxations, is an appropriate craze criterion [61]. Kawagoe and coworkers have proposed that diffusion of the challenge liquid into the polymer creates a swelling gradient which they propose is the primary driving force for ESC [62,63]. This is plausible in cases where the liquid is a relatively good solvent for the polymer but ESC is evident in many systems in which the liquid does not swell the bulk polymer appreciably and no swelling gradient is present.

Recognizing that cavitation and shear flow are frequently both involved in the formation of a craze, Sternstein has proposed a crazing criterion based on both the spherical and deviatoric components of stress for crazing in biaxially stressed dry poly(methylmethacrylate) (PMMA) [64]. Sternstein's criterion is described in Equation 1 and schematically in Figure 1. It states that a bias stress (σ_b) that is dependent on temperature, time and the 1st invariant of the stress tensor (I_1) promotes orientation in the direction of the largest principal stress. The criterion is attractive from a physical perspective in that the spherical component of stress might be associated with softening of the polymer followed by cavitation and the bias stress with the promotion of shear flow. Oxborough and Bowden, pointing out that Sternstein's definition of a critical bias stress loses physical meaning in a triaxial stress state, have suggested a qualitatively similar criterion, which they interpret in terms of a maximum critical strain [65].

Eq 1) $$\sigma_b = |\sigma_1 - \sigma_2| = A(T,t) + \frac{B(T,t)}{I_1}$$

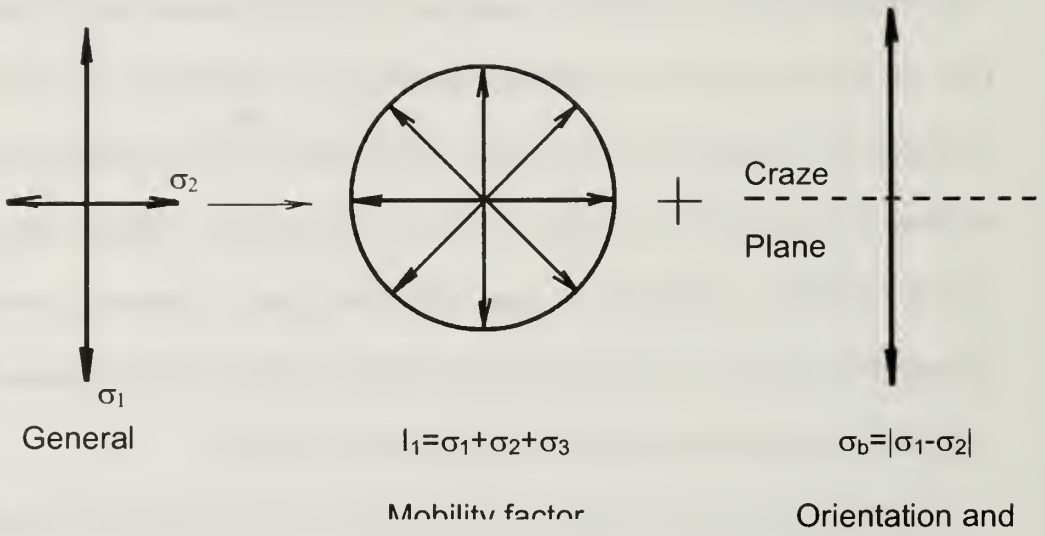

Figure 1: Schematic of Sternstein's crazing criterion. The spherical component of stress increases mobility and the stress bias term promotes orientation [64].

While the relative solubility of the liquid/polymer system describes the specific interaction between liquid and polymer well within a thermodynamic context, and is useful as a guide for materials selection, the correlation of solubility parameter differences with strain does not adequately connect the molecular polymer-liquid interactions to a continuum description of the deformation process. The crazing criteria of Sternstein and Oxborough and Bowden do take the continuum mechanics and temperature into consideration but do not describe the molecular interactions. A hypothetical crazing mechanism proposed by Gent nicely fuses the elements of these two criteria [49].

Gent's Hypothetical Crazing Mechanism

Gent's hypothesis proposes a stress-activated transition from the glassy to rubbery state that occurs at sites of stress concentration due to existing flaws in the polymer material. Consider crazing in the absence of an ESC liquid. Gent supposes that similarly to the Sternstein and Oxborough criteria, the spherical component of stress locally increases free volume at the flaw tip, thereby increasing segmental mobility and locally depressing T_g. This leads to cavitation and shear flow at a reduced stress level. Gent's contribution is to consider the glassy polymer to be a physically crosslinked network, and to apply the Flory-Huggins analysis of the equilibrium swelling of a crosslinked network by a solvent [66,67], to link the stress state of the polymer to the polymer-liquid molecular interactions. The analysis is based on the Helmholtz free energy of the network and considers the entropy and enthalpy of mixing and the elastic strain energy as described by the left hand side of equation (2). The right hand side term accounts for the spherical component of stress σ_{ii} acting on the polymer substrate. ϕ_2 is the volume fraction of polymer, χ is the polymer-solvent interaction parameter, V_1^m is the molar volume of the solvent, ρ_2 is the polymer density and M_c is the estimated molecular weight between physical crosslinks.

Eq. 2) $$\ln(1-\phi_2)+\phi_2+\chi\phi_2{}^2+\frac{V_1^m\rho_2}{M_c}(\phi_2{}^{\frac{1}{3}}-\frac{\phi_2}{2})=\frac{\sigma_{ii}V_1^m}{RT}$$

Eq. 3) $$\chi=\chi_s+\frac{V_1^m(\delta_1-\delta_2)^2}{RT}$$

Using the Hildebrand-Scatchard relationship to estimate χ (Equation 3) [68], and estimating a physical crosslink density M_c Gent's equation can be plotted as volume fraction of solvent vs. hydrostatic stress for level curves of χ. The form of the proposed model, shown in Figure 2, shows a critical spherical stress at which the swelling is unbounded. Inspection of the plot and equation indicate that Gent's hypothesis at least qualitatively captures many of the observed characteristics of ESC: (i) Hydrostatic compression tends to suppress swelling and prevent the onset of crazing. (ii) The critical crazing stress is temperature dependent and decreases as T_g is approached. (iii) The tensile stress at which crazing occurs when a surface-active liquid is present is much reduced, and the liquids tend to have solubility parameters similar to that of the polymer such that they are neither fully compatible solvents nor fully incompatible non-solvents. (iv) Increasing the molecular weight of a polymer can be expected to increase the density of physical crosslinks and so the observed threshold stress for swelling and subsequent crazing [69].

Gent's hypothetical crazing mechanism is appealing in that it describes many of the observed qualities of ESC failure. In addition it has a thermodynamic basis. If the transition to unbounded swelling could be observed by some thermodynamic indicator it would indicate that crazing is likely to occur after some time interval. In practical applications the most problematic ESC liquids are those in which crazing occurs at low levels of stress on a long timescale. A screening method based on Gent's hypothesis has the potential to be an industrially useful technique for screening polymer-liquid pairs for susceptibility to ESC on a short time scale.

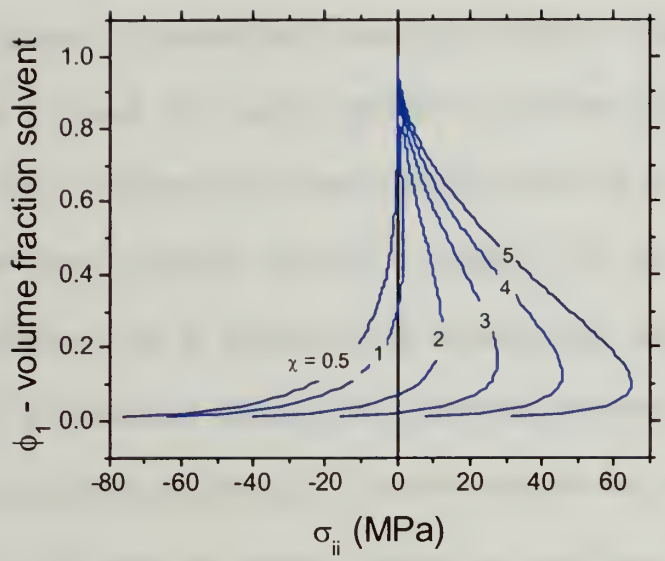

Figure 2: Plot of Gent's generalization of the Flory-Huggins equilibrium swelling relationship.

Wetting behavior as an indicator of unbounded swelling

One possible route toward evaluating the Gent hypothesis criterion for unbounded swelling is observation of the wetting behavior of an ESC liquid on a glassy thermoplastic substrate. This approach has been suggested by some preliminary data from a study using a polycarbonate-oleic acid system collected by Caskey and Lesser [70]. These experiments placed a horizontal polycarbonate substrate under fixed tensile load and observed the three phase contact angle of a sessile drop using a video goniometer. The observations, shown in figure 3, indicate that there is a drop in contact angle with load on the substrate that occurs near the critical hydrostatic stress of approximately 3-15 MPa embodied in Gent's equation for this material combination.

Given this preliminary result it was proposed that further study of the wetting behavior of ESC liquids as a function of the stress state of the polymer has potential to yield insight into the validity of Gent's hypothetical mechanism for crazing. However, there are some experimental hurdles to overcome: First, ESC liquids generally wet polymer substrates well and the resulting three phase contact angles are often less than 20°. Such small angles are very difficult to measure accurately using the various goniometry methods because determination of the tangent at the three-phase line is subjective at best. Typical precision reported for the goniometer technique is in the range of 2-5° [71]. An objective and sensitive method of measuring contact angle is needed. Second, contact angle by itself does not directly indicate the solid liquid interaction. Inspection of Young's equation, shown in Equation 4 and graphically in Figure 4, indicates that inference of the solid-liquid interaction (γ_{SL}) term requires measurement of the effect of substrate stress on both the contact angle (θ) and the solid-vapor term (γ_{SV}).

Both an objective and accurate method of measuring small three phase contact angles and an independent method of measuring the effect of substrate stress on the solid-vapor surface energy were needed to use wetting behavior to evaluate the Gent hypothesis. In this research experimental solutions to these two issues were developed: small contact angles were measured as a function of substrate stress using both conventional goniometry and the refraction of light through the sessile drop lens and the effect of stress on the solid-vapor surface energy was evaluated using a modified Contact Adhesion Test (CAT) based in JKR theory. The strain condition at the onset of crazing and the elapsed time at the onset of crazing were also observed.

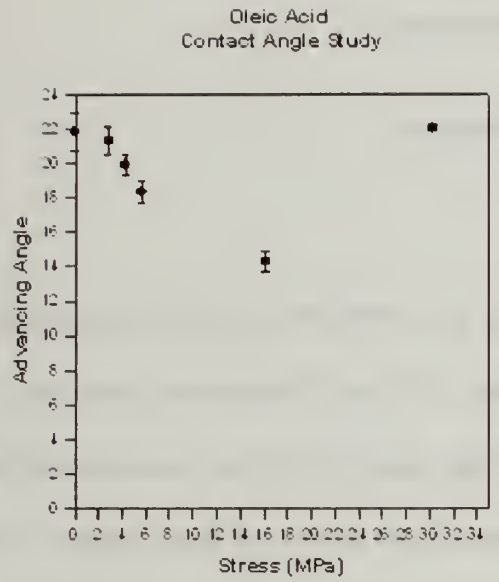

Figure 3: Caskey's preliminary data for contact angle as a function of stress. The oleic acid/polycarbonate system shows a drop in angle with increasing stress [70]

Eq. 4) $$\lim_{\Delta A \to 0} \frac{\Delta G_s}{\Delta A} = 0 = \gamma_{SL} - \gamma_{SV} + \gamma_{LV} \cos\theta$$

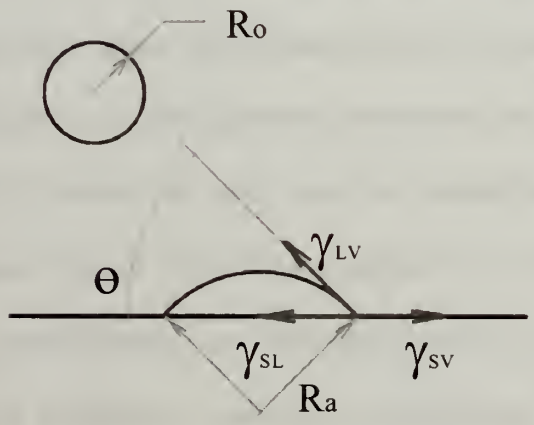

Figure 4: Sessile drop force balance.

Experimental

Materials

Contact Adhesion Testing

The polycarbonate substrate film is a commercially available material purchased from McMaster Carr and used as received. 0.25 mm thickness polycarbonate samples were cut into 12 mm x100 mm strips with the machine direction oriented with the 100m axis. Hemispherical lenses of 4mm diameter were fabricated from Sylgard 185 PDMS resin crosslinked by hydrosilylation using 5 wt% of crosslinker. The PDMS lenses were then spin coated with a 10 wt% solution of polycarbonate in chloroform at 900 RPM resulting in a uniform thin film over the lens surface.

Contact angle with respect to substrate stress observations:

The materials used for observations of three-phase contact angle with respect to stress are described in Table 1. The polycarbonate substrate film is a commercially available material purchased from McMaster Carr and used as received. 0.25 mm thickness polycarbonate samples were cut into standard ASTM 638 Type 1 tensile bars. The surface active liquids, oleic acid and dibutyl phthalate, were chosen based on their solubility parameters relative to the polycarbonate substrate, comparable molecular weights, and low vapor pressures, which renders evaporation of liquid from the sessile drop negligible. Oleic acid is a monounsaturated lipid that is a non-solvent for polycarbonate. In contrast, dibutyl phthalate is a plasticizer and can be expected to swell polycarbonate even in the absence of a dilatational stress. Both liquids are stress cracking agents for polycarbonate.

Figure 5 shows the gent equation predictions for ESC liquid uptake with increasing spherical stress. For dibutyl phthalate-PC swelling and subsequent crazing can be expected at very low stress levels. For oleic acid-PC a range of critical swelling stresses are predicted of between 3-15 MPa spherical stress.

Table 1: Some physical properties of ESC materials

	MW ***[g/mol]***	V_m $[cm^3/mol]$	δ $[MPa]^{1/2}$	γ $[mJ/m^2]$
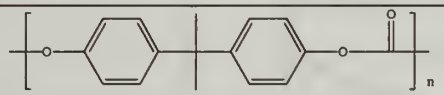 polycarbonate	11,000	9167*	20-21	42.9
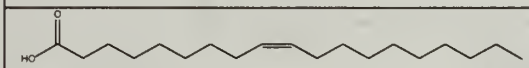 oleic acid	282.5	317	15.6	33
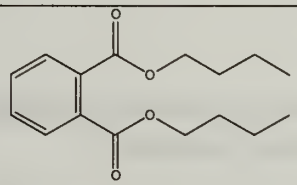 dibutyl phthalate	278.3	267	20.2	34

*estimated molecular weight between physical crosslinks after reference [49].

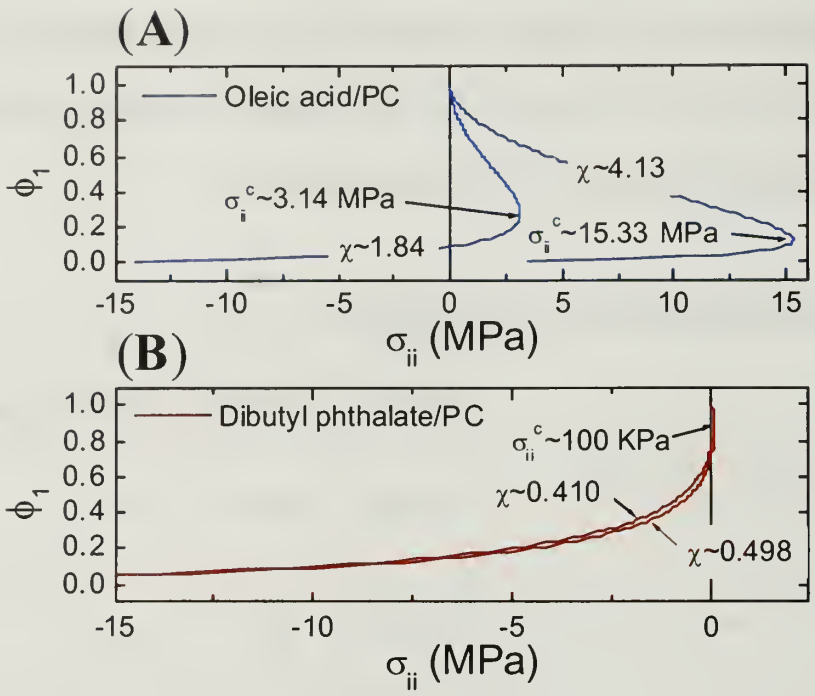

Figure 5: Gent hypothesis prediction of critical stress for unbounded swelling. (A) polycarbonate/oleic acid and (B) polycarbonate/dibutyl phthalate

Crazing Kinetics Under Fixed Displacement Conditions

Sheets of commercially produced 3mm thickness polycarbonate were purchased from McMaster Carr Industrial Supply and were cut to bars of 20mm width and 200 – 218 mm length depending on the level of strain desired. A series of ester family ESC liquids with a range of solubility difference were purchased from Sigma-Aldrich and used as received. The structures and some physical characteristics of the ESC liquids: propyl acetate, diethyl fumarate and dibutyl phthalate are described in Table 2.

Table 2: Some physical properties of materials used ESC kinetics observations.

	MW (g/mol)	ρ (g/mL)	V^m (cm^3/mol)	δ ($MPa^{1/2}$)
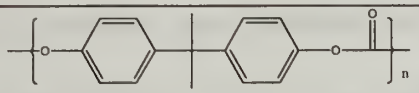 polycarbonate	11000	1.20	-	20.5
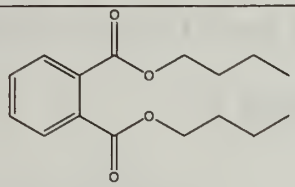 dibutyl phthalate	278.4	1.043	266.9	20
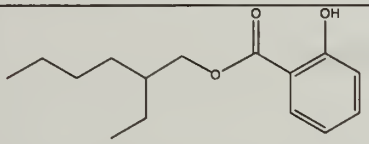 2-ethylhexyl salicylate	250.34	1.014	247	19.8
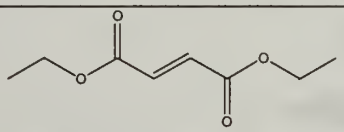 diethyl fumarate	172.2	1.052	163.67	19.5
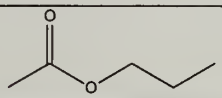 propyl acetate	102.13	0.888	115.01	18

Methods

Contact Adhesion Testing

The technique used to evaluate solid-vapor surface energy is a modification of the JKR theory based Contact Adhesion Test, commonly used to characterize small magnitudes of adhesion in soft materials [72,73]. CAT has been successfully used by M. Tirrell to measure the solid-vapor surface energy of an unstressed solid [74]. In the variation of CAT used in this work a hemispherical lens of PDMS is brought into contact

with a polycarbonate film placed in uniaxial tension as illustrated in Figure 6. The contact area radius a, normal Force P and vertical displacement δ are observed. The energy release rate to create new surface area can then be estimated using equations 5, 6 and 7 [75,76]. For symmetrical contact the energy release rate is twice the solid-vapor surface energy (Eq. 8). For asymmetric contact the energy release rate is the sum of the surface energy of each surface minus the interfacial surface energy (Eq. 9).

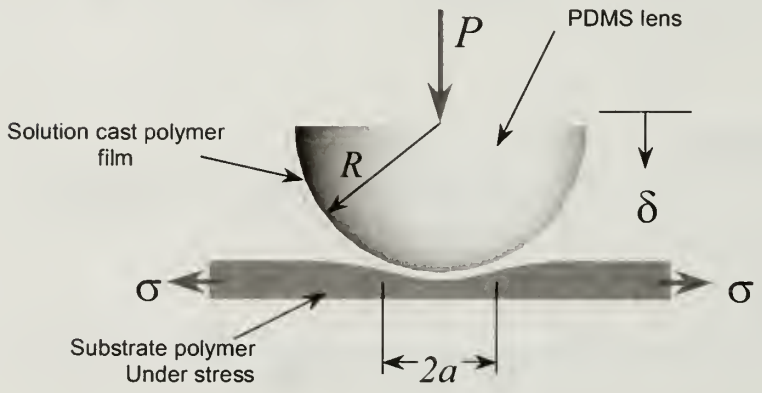

Figure 6: Schematic of JKR theory based Contact Adhesion Test used to measure effect of uniaxial stress on solid-vapor surface energy.

Eq. 5) $$\left(\frac{a^3K}{R}-P\right)^2 = G_{JKR}\left(6\pi K a^3\right)$$

Eq. 6) $$W_{adh} = \frac{1}{\pi a_{\max}^2}\int_{\delta_o}^{\delta_f} P\partial\delta$$

Eq. 7) $$G_{crit} = -\frac{4P_{\max}}{3\pi R}$$

Eq. 8) $$G_{JKR}, W_{adh}, G_{crit} = 2\gamma$$ a=b, Symmetrical contact

Eq. 9) $$G_{JKR}, W_{adh}, G_{crit} = \gamma_a + \gamma_b - \gamma_{ab}$$ a≠b, Asymmetrical contact

Mass uptake of ESC Liquids

Mass uptake experiments were conducted on 50mm x 50mm x 4mm PC samples immersed in a series of ESC liquids at 21°C. The samples were periodically removed from the liquid blotted dry and weighed. The initial gradient (R) of the resulting plots of mass with time (M_t) were analyzed to determine diffusion coefficient (D) using equation 10 [77]. The equilibrium mass uptake (M_∞) is either observed during the experiments or estimated using a numerical fit of the mass uptake data.

Eq. 10) $$\frac{M_t}{M_\infty} = \frac{4}{\pi^{\frac{1}{2}}}\left(\frac{Dt}{l^2}\right)^{\frac{1}{2}}$$

$$R = \frac{d\left(\frac{M_t}{M_\infty}\right)}{d\left(\frac{t}{l^2}\right)^{\frac{1}{2}}} \qquad \overline{D} = \frac{\pi}{16}R^2$$

Contact Angle By Refraction

Contact angles between an ESC liquid-polymer pair are typically smaller than 20° and are difficult to measure using conventional goniometry techniques. Measuring contact angle by goniometer involves imaging the sessile drop profile and manually measuring the angle at the three-phase line. The manual selection of the tangent line for such small angles is highly subjective and typically precisions are reported as ±2-5 degrees. The refraction approach presented here is an objective and accurate technique for measuring such small angles with precision of approximately ±0.5 degrees.

The basis of the refraction method, illustrated in figure 7, is the refraction of light through both the polymer substrate alone and the substrate and sessile drop lens near the

sessile drop edge. The difference in refractive indices of the liquid and vapor phase causes a divergence of the light into two paths at angles with the substrate normal of α and β. Application of Snell's law across the three unique interfaces in the system and measurement of the angles α and β allows calculation of the three phase contact angle θ according to equation 11.

The device used to measure ESC liquid contact angles on polymer substrates is illustrated schematically in Figure 8. The substrate material is held in a horizontal fixture upon which a mechanical stress can be introduced with a mass or other mechanical testing system. Once a drop is applied, the transmitted light incident on the vertical detector is photographed using a CCD camera. The resulting images are used to determine the dimensions Z_α and Z_β. Subsequently, the angles α and β may be calculated from the X, Z_α and Z_β measurements. An enclosure around the sample ensures protection from airborne particles and gives the ability to control the nature of the vapor phase. An LVDT is used to monitor the strain condition of the tensile bar, temperature is monitored using a thermocouple, and an electronic relative humidity sensor is used to record the relative humidity of the vapor phase which can be conditioned to be dry or moist within limits of approximately 10%-70% relative humidity.

Figure 9A shows a typical refraction images for the oleic acid on a polycarbonate substrate. The upper spot is the α refraction due to light refracting through the polymer substrate only and the extreme lower arc is the β spot - light refracting through both the substrate and near the three-phase line of the sessile drop. The irregularity of the β refraction is indicative of spatial variation at the sessile drop edge. A sessile drop edge of oleic acid on a PC substrate is shown viewed from above in the Figure 9B reflection

optical micrograph and variation in the three phase contact angle at the drop edge is apparent.

Using standard error propagation analysis (Equations 12, 13) [78] and estimates of the errors associated with the length X and Z_α and Z_β the limiting precision of the refraction technique for these materials and experimental conditions is presented in Table 3 and is estimated to be ±0.5°.

During the refraction observations of contact angle with respect to substrate stress the strain condition of the substrate was monitored using an LVDT (Linear Voltage Differential Transformer). The time resolved refraction images collected during the experiments to determine contact angle also allow length-scale consistent determination of the time and strain at which craze damage is commensurate with the LASER wavelength λ. This is accomplished by observation of the onset of diffraction fringes caused by the parallel array of closely spaced crazes. Figure 10 illustrates the refraction/diffraction geometry and compares early and later time refraction images for an polycarbonate- oleic acid sample at a hydrostatic stress of ~13 Mpa. The early time image has no diffraction fringes while the later time image shows distinct diffraction fringes. The transition to diffraction fringes is observed before crazes in the tensile sample are easily visible to the naked eye.

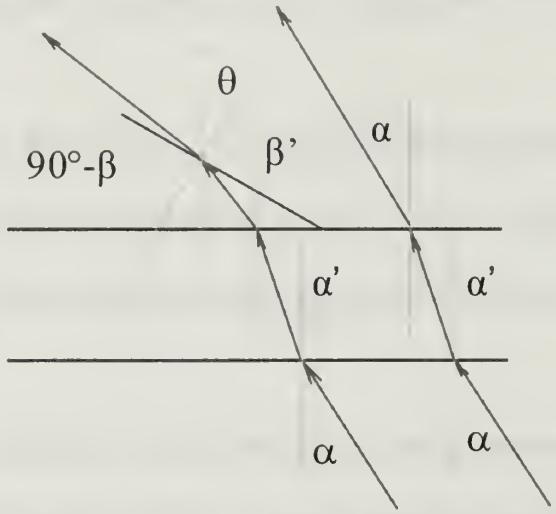

Figure 7: Schematic of refraction geometry showing refraction of incident LASER through sessile drop lens and substrate material.

Eq. 11)

$$\tan\theta = \frac{n_1(\sin\beta - \sin\alpha)}{n_2\left(1-\left(\frac{n_1}{n_2}\right)^2 \sin^2\alpha\right)^{\frac{1}{2}} - n_1\sin\beta}$$

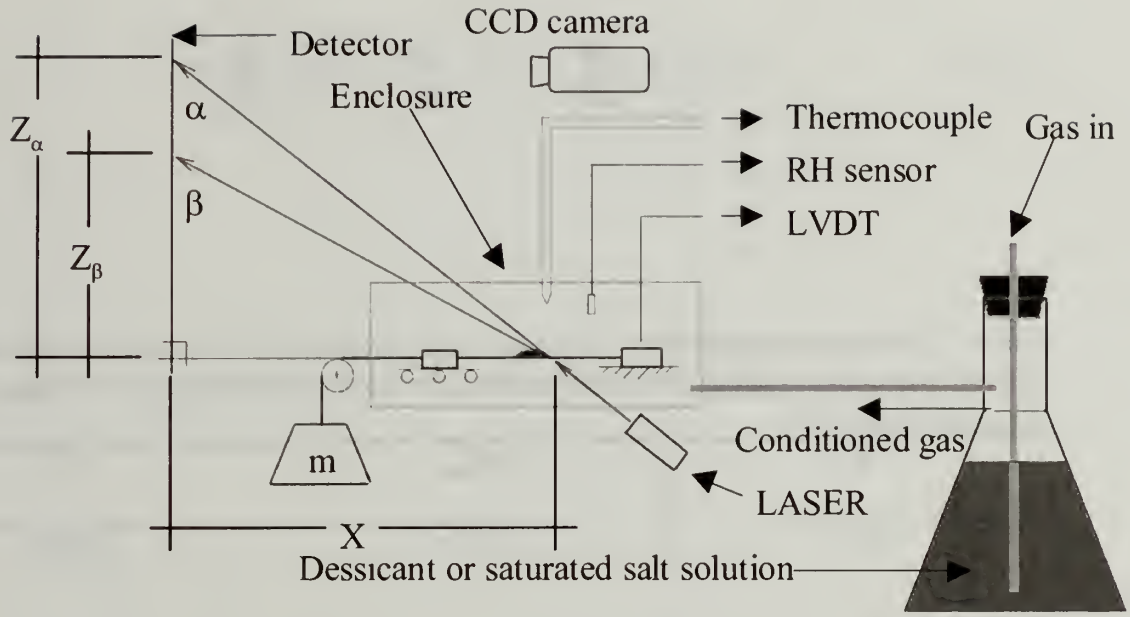

Figure 8: Schematic of refraction device showing tensile sample, sessile drop, means of applying load, environmental enclosure, detector and LASER source.

Figure 9: (A) Oleic acid/polycarbonate refraction pattern showing measurands Z_α, and Z_β. (B) Reflectance mode optical micrograph of oleic acid/polycarbonate sessile drop edge viewed from above.

Eq. 12)
$$E_{\max} = \left|P_X \frac{\partial R}{\partial X}\right| + \left|P_{Z_\alpha} \frac{\partial R}{\partial Z_\alpha}\right| + \left|P_{Z_\beta} \frac{\partial R}{\partial Z_\beta}\right|$$

Eq. 13)
$$U = \left[\left(P_X \frac{\partial R}{\partial X} \right)^2 + \left(P_{Z_\alpha} \frac{\partial R}{\partial Z_\alpha} \right)^2 + \left(P_{Z_\beta} \frac{\partial R}{\partial Z_\beta} \right)^2 \right]^{\frac{1}{2}}$$

Table 3: Estimate of maximum error (E_{max}) and uncertainty (U) in contact angle for oleic acid-polycarbonate system. Probable limiting precision of the refraction technique approximately ±0.5°.

θ	E_{max}	U
0°	±0.64°	±0.50°
1.31°	±0.65°	±0.50°
2.60°	±0.65°	±0.49°
3.88°	±0.65°	±0.49°
5.14°	±0.65°	±0.48°
6.37°	±0.65°	±0.47°
7.57°	±0.65°	±0.46°
8.73°	±0.64°	±0.45°
9.86°	±0.64°	±0.44°
10.94°	±0.63°	±0.43°
11.96°	±0.62°	±0.41°
12.93°	±0.60°	±0.40°
13.84°	±0.59°	±0.38°

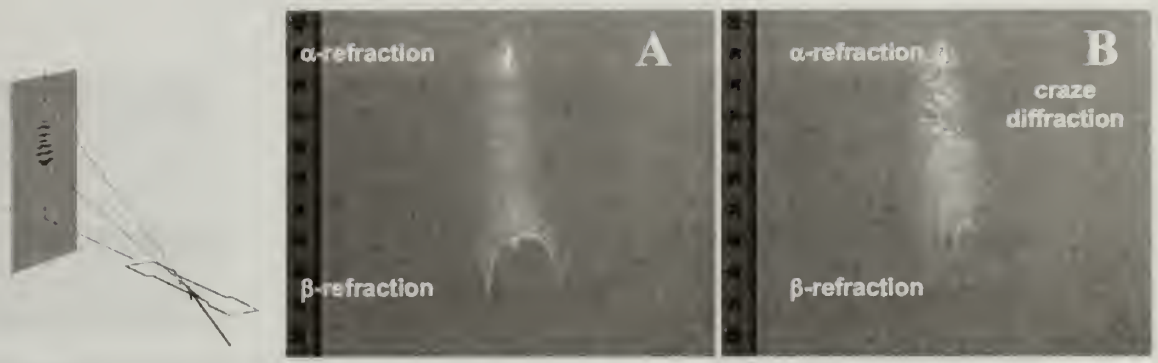

Figure 10: A) Refraction image prior to the onset of crazing. B) Refraction image after onset of crazing. Diffraction fringes in refraction image indicate growth of craze to a length scale commensutrate with the 632 nm wavelength LASER.

Contact Angle by Goniometry

Polycarbonate films of 0.25mm thickness, 12mm width and 100mm length were placed in a microscope stage equipped with a set of horizontal tensile grips through which measured increments of displacement can be applied. A microliter scale syringe operated by a linear drive stepper motor and controller was used to apply and remove the ESC liquid to and from the sessile drop at a constant flow rate of 0.125 μL/s resulting in a three-phase line velocity of approximately 0.1820 mm/s. The capillary or reduced velocity ($U\mu/\gamma_{LV}$) is then in the range of $1.5x10^{-4}$, appropriate for determination of advancing contact angle [79]. A CCD camera is used to image the profile of the sessile drop and contact angles are manually measured from each limb of the sessile drop using UTHSCA ImageTool v3.1. Typical images for advancing and receding three phase line are shown in Figure 11. A plot of angles recorded during advance and recession are

shown in Figure 12. The advancing angle is taken as the average during the equilibrium plateau.

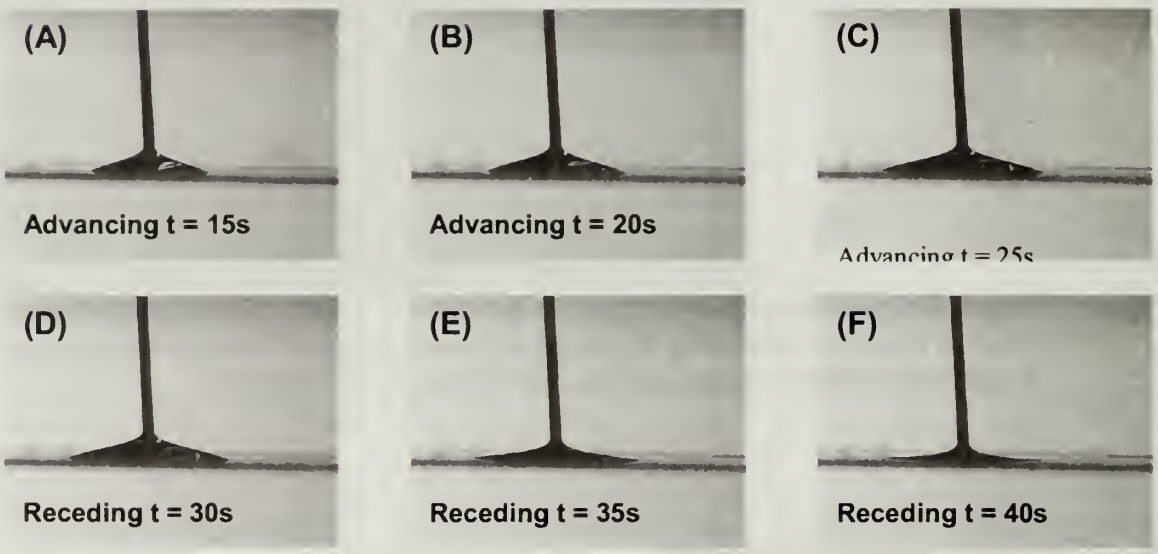

Figure 11: Video goniometer images showing application of oleic acid to polycarbonate substrate and the advance and recession of the three-phase line.

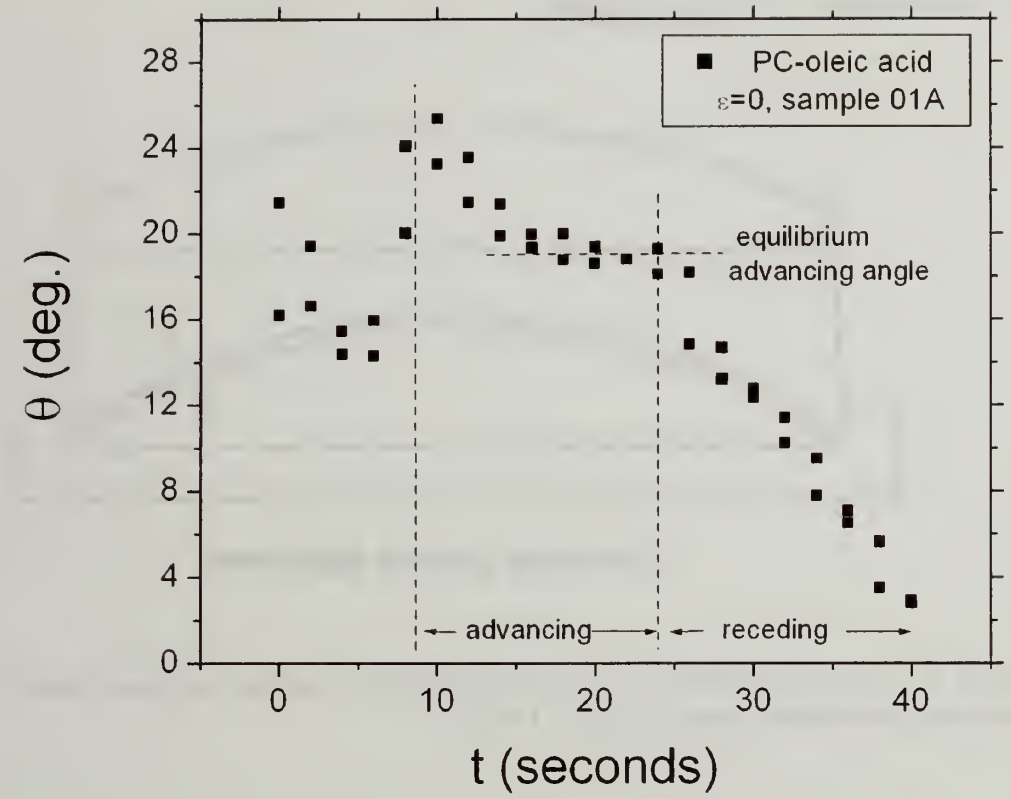

Figure 12: Plot of contact angle wrt to time for a fixed uniaxal strain oleic acid-polycarbonate sample. Note plateau of equilibrium advancing angle during 16s<t<25s interval. Advancing angles are taken as the average of the plateau region for three separate samples.

Crazing Kinetics Under Fixed Displacement Conditions

ASTM 638 Type 1 tensile bars of 0.125" thick polycarbonate were placed in a two point bending jig to result in 0.5%, 1.0% and 1.5% strain at the specimen midpoint and extreme fiber. The device is illustrated in Figure 13. Strain level at the midpoint was estimated using equation 14 [80]. A series of ester family ESC liquids with a range of solubility difference and molar volume were applied to the samples and the time to the

onset of crazing estimated from visual observations of craze formation using a stereomicroscope at 5X magnification.

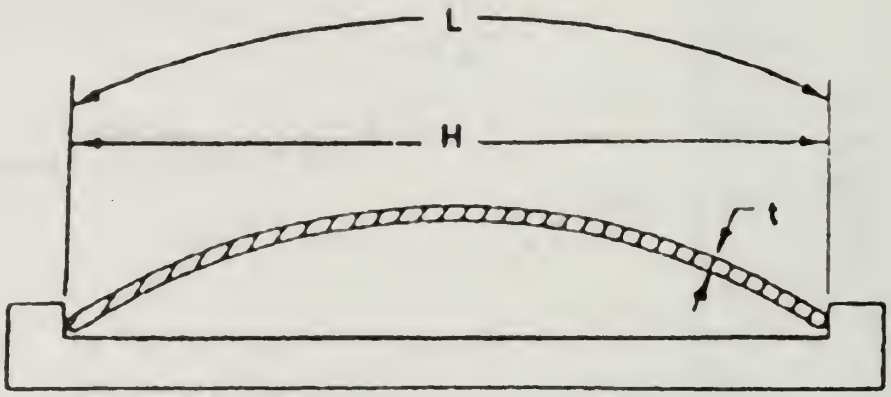

Figure 13: Two-Point bending jig for fixed strain ESC testing. Maximum strain at midpoint is calculated using Equation 14 [80]

Eq. 14) $$L = \left(\frac{kt}{\varepsilon}\right)\sin^{-1}\left(\frac{\varepsilon \cdot H}{kt}\right)$$

IFF: $0.01 \le \frac{L-H}{H} \le 0.50$; $k \approx 1.28$

Results and Discussion

CAT: Effect of Substrate Stress on Solid-Vapor Surface Energy

The JKR based Contact Adhesion Test was used to assess the effect of uniaxial stress on the solid-vapor surface energy of the polymer substrate. Both PDMS-PC and a PC-PC systems were evaluated. Force displacement curves for PDMS-PC contact are shown in Figure 14 and images of the contact area in Figure 15. . The lack of interference fringes in indicates that the surface of the PDMS near the three-phase line of contact is approximately normal to the PC substrate surface. Figure 16 is a plot of the energy release rate and overall work of adhesion as estimated from equations 5 and 6 for PDMS-PC contact as a function of stress. Because the system is asymmetric the solid vapor surface energy cannot be directly determined but the experiment does indicate that G_{Crit} and W_{Adh} are approximately constant with substrate stress. Figure 17 shows the force-displacement curves for PC-PC contact. In comparison with the previous PDMS-PC system the adhesion is of much smaller magnitude. Images of the contact area are shown in Figure 18. The existence of interference fringes indicates that the surfaces of the PC coated hemisphere and substrate are tangent to each other. The asymmetry of the contact area is due to swelling of the PDMS lens during the process of solvent casting a thin layer of PC on the Lens surface. Figure 19 is a plot of solid vapor surface energy with increasing stress as estimated using G_{JKR}, G_{Crit} and W_{adh} (Equations 5, 6 and 7 respectively). Because of the small adhesive forces present in PC-PC contact the G_{JKR} and W_{Adh} quantities show a great deal of variability. G_{Crit} as estimated from the maximum pull-off force (Eq 6.) is taken as the most appropriate metric and it shows a solid-vapor surface energy of ~42 mJ/m^2 that remains constant with substrate spherical stress.

These results indicate that for the levels of stress used in this investigation of Gent's ESC hypothesis the solid vapor surface energy of polycarbonate is independent of the stress acting on it and that the three phase contact angle can be directly used to indicate changes in the solid-liquid interactions.

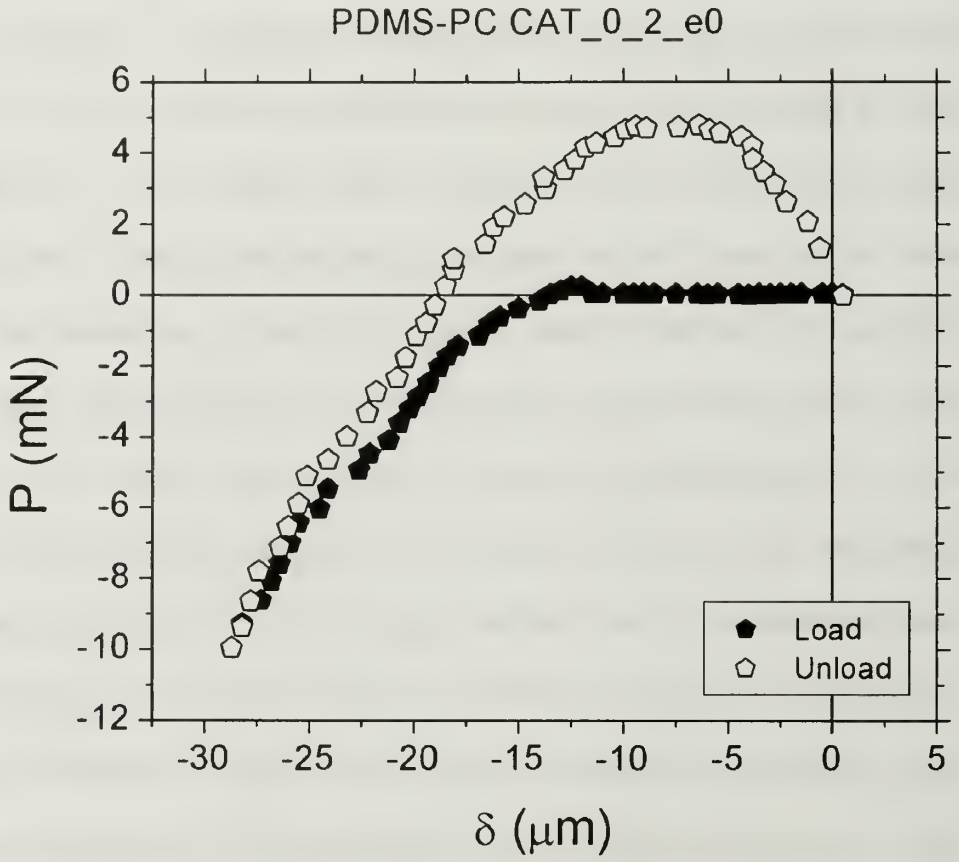

Figure 14: Load-displacement curves for polycarbonate-polydimethylsiloxane contact during Contact Adhesion Testing. Polycarbonate substrate is at zero strain. Large degree of hysteresis and large maximum pull-off force indicates relatively large adhesion forces.

Figure 15: Images of contact area for polycarbonate-polydimethylsiloxane during Contact Adhesion Testing. (A) maximum contact area. The lack of interference fringes at the perimeter indicates that the PDMS suface ia approximately normal to the PC substrate material as in the diagram to the left. (B) composite of contact areas during loading and unloading.

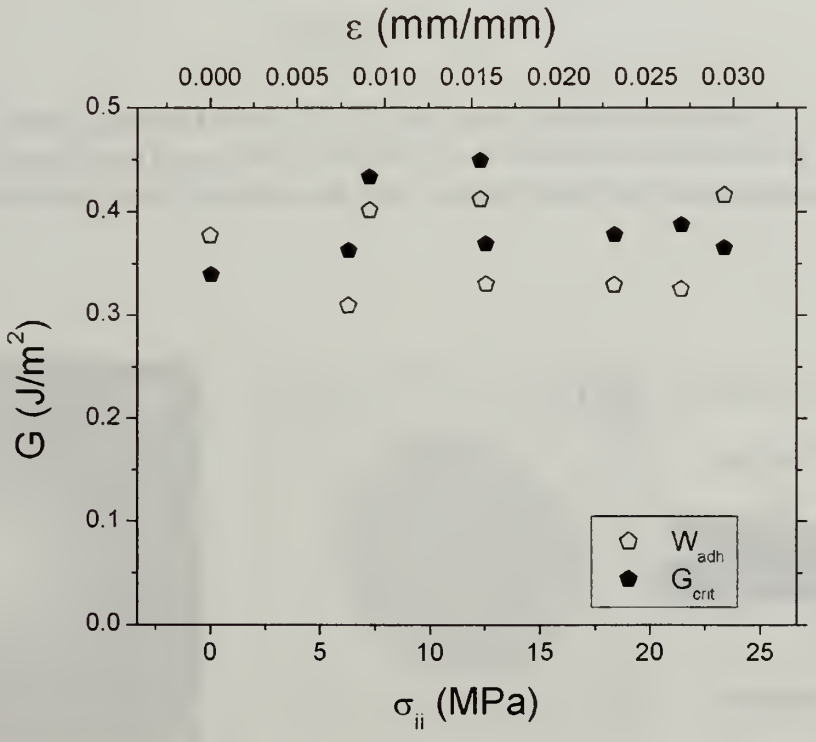

Figure 16: Work of adhesion (W_{adh}) and critical energy to create surface (G_{crit}) vs. spherical component of stress for contact between a uniaxially stressed polycarbonate substrate and a PDMS hemisphere. Both quantities indicate that the energy release rate and hence the interfacial energies acting on the PC substrate are independent of substrate stress.

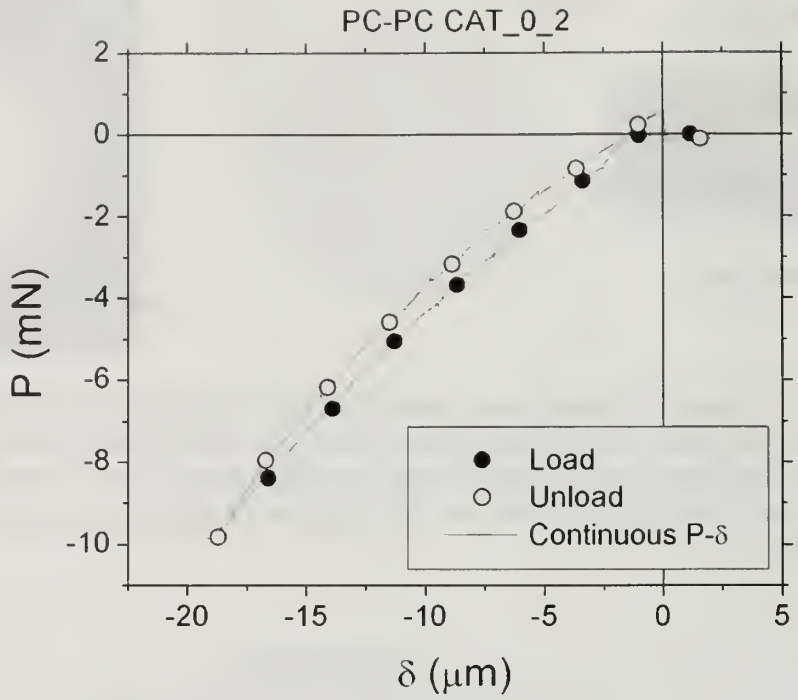

Figure 17: Load-displacement curves for PC-PC contact during Contact Adhesion Testing. Polycarbonate substrate is at zero strain. The small magnitude of hysteresis and small maximum pull-off force indicate very low adhesive forces between the surfaces.

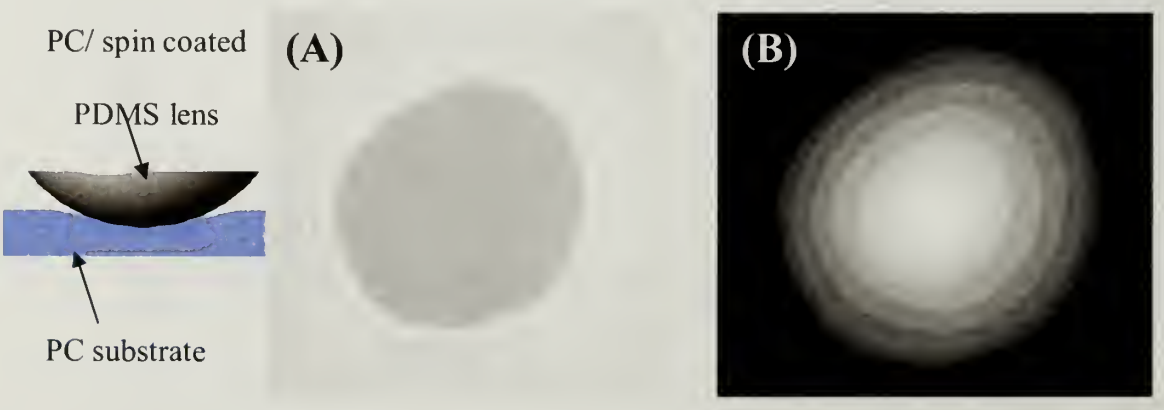

Figure 18: Images of contact area for polycarbonate-polycarbonate contact during Contact Adhesion Testing. (A) maximum contact area. The presence of interference fringes indicates tangent-tangent interface at the contact area perimeter as in the diagram to the left. (B) composite of contact areas during loading and unloading. Distortion of the hemispherical probe is due to swelling during the solution casting of the polycarbonate coating.

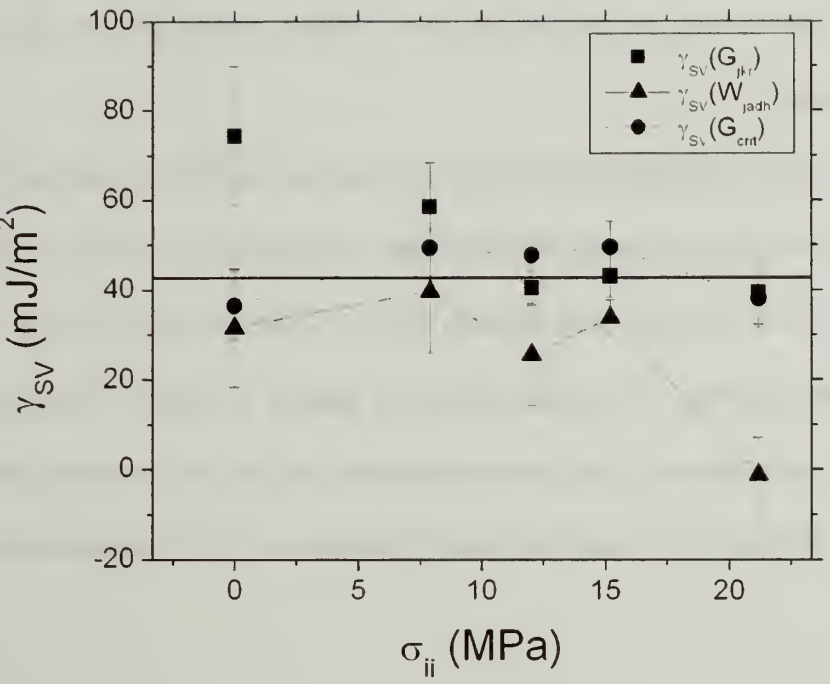

Figure 19: Plot of solid-vapor surface energy with respect to the spherical component of stress of a uniaxially loaded polycarbonate sample as determined from Contact Adhesion Testing. Small degree of adhesion for polycarbonate-polycarbonate contact increases the variability of surface energy determined from GJKR and WADH. Surface energy derived from GCrit is similar to that measured using conventional contact angle studies (42 mJ/m2). GCrit is taken as the most appropriate indicator and shows that γSV is constant with increasing stress.

Evaluation of Gent ESC Criterion Using Observations of Contact Angle

Contact angle as an indicator of swelling

Mass uptake experiments were conducted on 50mm x 50mm x 4mm PC samples immersed in both oleic acid and dibutyl phthalate at 21°C. The results are shown in Figures 20 and 21. Dibutyl phthalate swells PC strongly. At ~8% mass uptake the sample lost physical integrity and could no longer be weighed accurately. The diffusion coefficient estimated fromn the dibutyl phthalate/polycarbonate data using equation 10 is

D= 8.62766E-14 m^2/s. Oleic acid appears not to swell polycarbonate within the limits of ±1% as there was no significant mass uptake during the 70 day duration of the observation.

Having established that Oleic acid does not swell PC significantly and that dibutyl phthalate will spontaneously swell PC the contact angle of a sessile drop of each on a PC substrate was observed with time to indicate whether contact angle is an appropriate metric for swelling. The results shown in figures 22 and 23 confirm this: the contact angle of a sessile drop of the non-solvent oleic acid on a PC substrate does not decay with time while that of the plasticizer dibutyl phthalate on a PC substrate decays strongly with time.

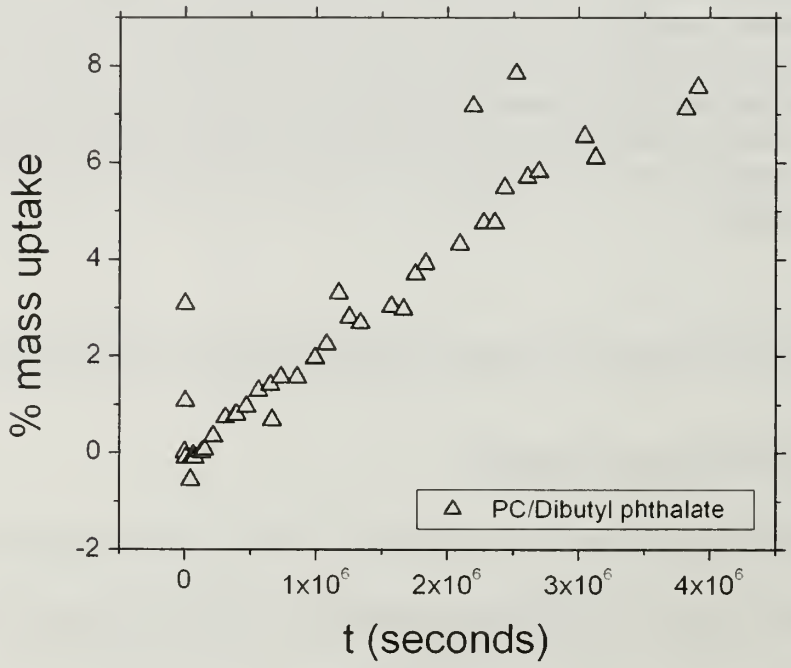

Figure 20: Mass uptake for polycarbonate in dibutyl phthalate. At ~8% solvent uptake the PC sample lost physical integrity and could no longer be weighed accurately.

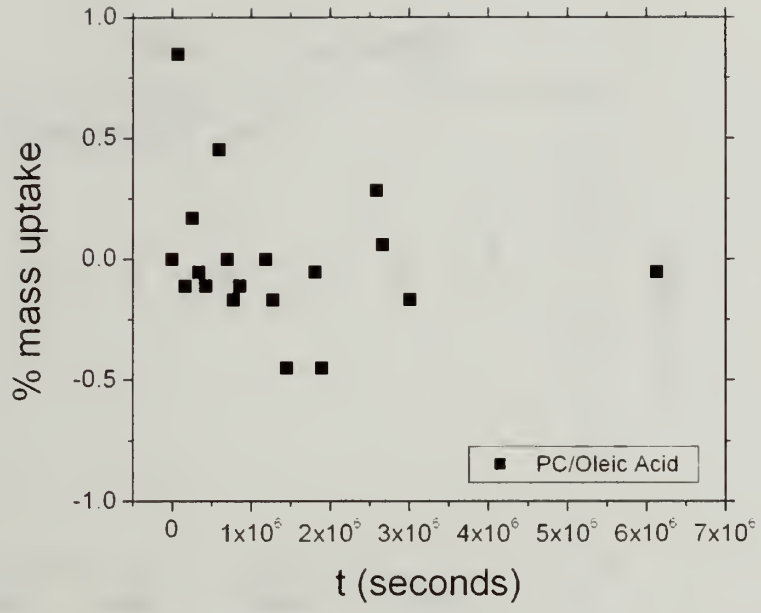

Figure 21: Plot of mass uptake with respect to time for polycarbonate immersed in oleic acid. The data indicates that no significant amount of oleic acid is absorbed during the 70 day duration of the observation. The PC sample remained optically clear throughout the observations.

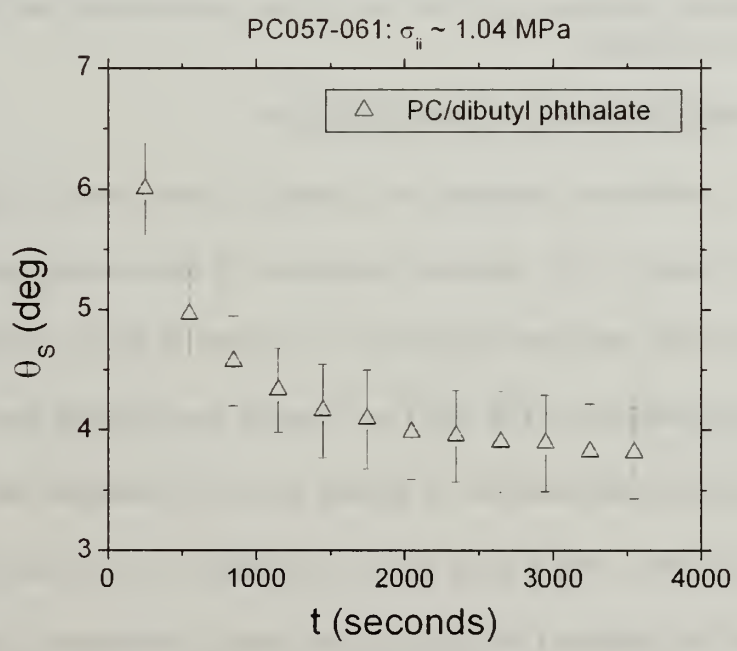

Figure 22: Static contact angle with respect to time for a sessile drop of dibutyl phthalate on a polycarbonate substrate. Strong decay with time is due to spontaneous swelling of substrate. Each data point is the mean of five observations and the error bars indicate one standard deviation on the mean.

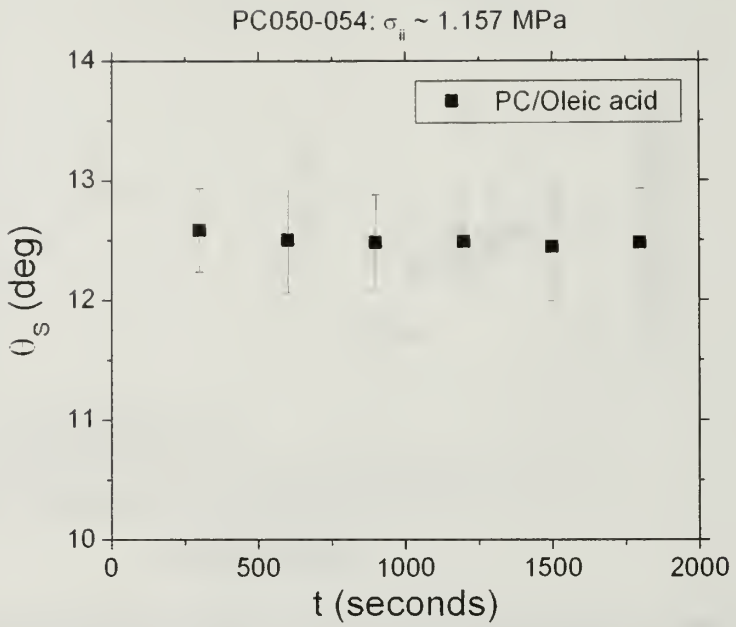

Figure 23: Plot of contact angle with respect to time for a sessile drop of oleic acid on a polycarbonate substrate. No significant decay in contact angle with time is observed. Each data point is the mean of five observations and the error bars indicate one standard deviation on the mean.

Contact angle with respect to stress: Refraction

The refraction technique was applied to observation of the advancing contact angle with respect to the spherical component of stress acting on the substrate material for oleic acid-PC and dibutyl phthalate-PC systems. A 0.25 mm thick polycarbonate film was cut into standard ASTM 638 Type 1 tensile bars insuring that the machine direction was parallel with the direction of applied stress. The substrate film was clamped in the horizontal fixture. After a fixed load was applied a 1 μL sessile drop of oleic acid was applied to the middle of the gauge length using a micrometer syringe. Contact angle, strain condition, temperature and relative humidity were observed as the drop spread onto the PC substrate surface.

The results for PC-dibutyl phthalate are presented on figure 24 and show that contact angle is constant with substrate stress. The results for PC-oleic acid are shown in figure 25.

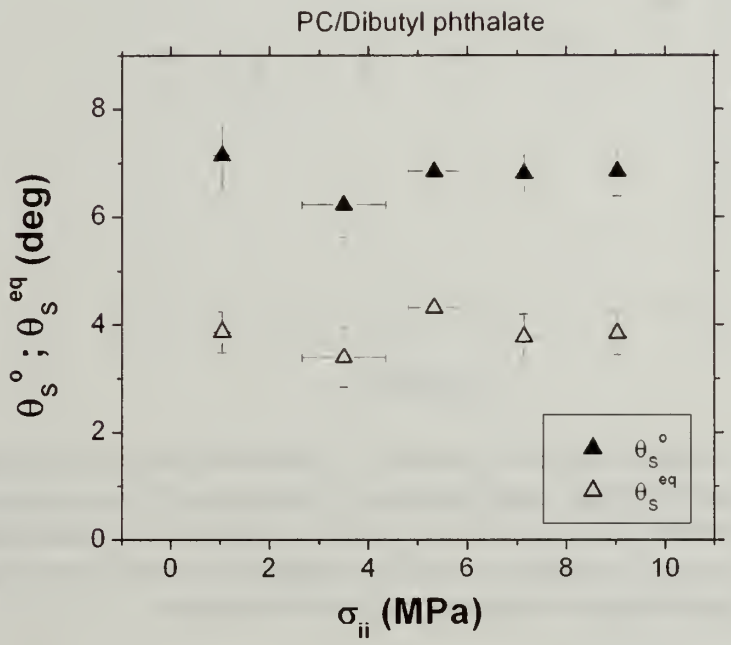

Figure 24: Initial and equilibrium contact angle as a function of spherical stress for dibutyl phthalate on a polycarbonate substrate. Each data point is the mean of five samples and the error bars indicate 1 standard deviation on the mean. The time decaying contact angle data was fit using a first order exponential decay model and the initial t=0 and equilibrium t=∞ angles calculated. The filled triangles are the initial t=0 contact angle and the unfilled triangles are the equilibrium angle at t=∞. Both quantities indicate contact angle is independent of substrate stress for this system.

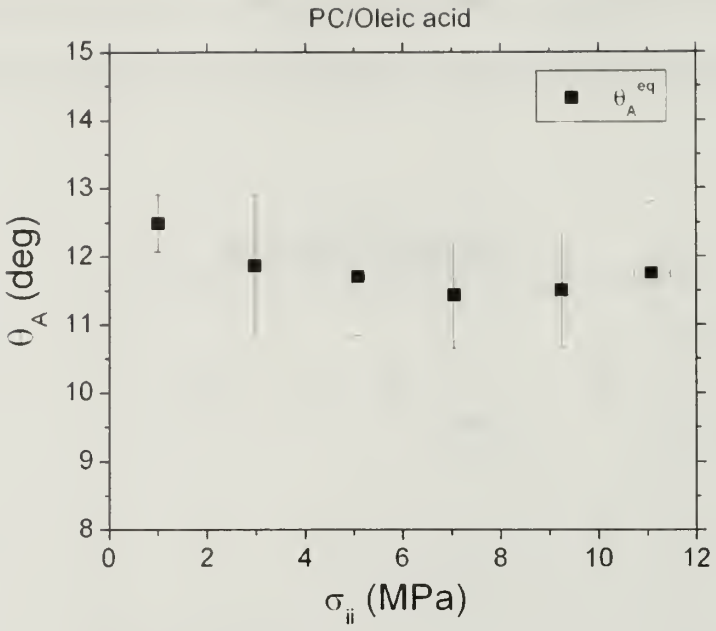

Figure 25: Contact angle as a function of spherical stress for oleic acid on a polycarbonate substrate. Each data point is the mean of five samples and the error bars indicate 1 standard deviation on the mean. The data show a weak trend toward a minima at ~7MPa spherical stress but given the magnitude of error contact angle must be considered approximately constant with substrate stress.

Contact angle for amphiphilic molecules like oleic acid is highly sensitive to the amount of moisture present in the vapor phase. During the previously described work the vapor phase relative humidity was kept constant at approximately 10%.

Figure 26 shows refraction method contact angle observations for an oleic acid-polycarbonate system under changing conditions of relative humidity (ω). The humidity conditions begin at 20%, are cycled up to 70%, then cycled down to 20%. As relative humidity is increased the contact area of the sessile drop spreads and the contact angle drops. The triple line is translating onto dry substrate yielding advancing angles (θ_A). As the relative humidity is decreased back from 70% the contact area is at first pinned then retracts. The triple line is receding from wetted substrate and the contact data are receding angles (θ_R). Each observation of contact angle was taken at a 300 second

interval and so the plot shows that the contact area of the sessile drop spreads onto dry substrate more readily than it recedes.

The large degree of hysteresis between the advancing and receding angles, and the pinning evident in this data, provides a possible explanation for the lack of a σ_{ii}^{c} transition in the refraction method observations of θ_A vs. σ_{ii} reported in figures 24 and 25. For the oleic acid-polycarbonate system the magnitude of hysteresis is on the order of 3°-5°. Contact angles within the limits of θ_A and θ_R are in thermodynamic equilibrium, and the effect of changes in γ_{SL} on θ could reasonably be expected to be smaller than this given the localized nature of the swelling proposed in the Gent hypothesis. In this light, any changes in θ related to Gent's transition to unbounded swelling could easily be obscured by pinning of the sessile drop between the limits of the advancing and receding angles when the three phase line is translating very slowly as in the previous contact angle vs. spherical stress state refraction observations.

Figure 27 shows the refraction images during (A) three-phase line advance and (B) three-phase line recession during the relative humidity driven contact angle advance and recession of figure 26. The lower β-refraction spot of the refraction images contains information on spatial variation of the three-phase line and the images give qualitative indication that the advancing three-phase line is more uniform that the receding three-phase line. This observation is consistent with the pinning of contact angles observed during recession.

The hysteresis between advancing and receding angles driven by changing relative humidity as a function of substrate stress was investigated as a possible indicator of Gent's unbounded swelling transition. A 0.25 mm thick polycarbonate film was cut

into standard ASTM 638 Type 1 tensile bars and placed under fixed stress in the refraction device. A sessile drop of 1 uL volume of oleic acid was placed on the PC substrate at 20% relative humidity. The humidity was then cycled to 70% for one hour then and back to 20% over one hour. Humidity was then held constant for two hours. The contact angle hysteresis was determined as the difference between the initial angle at 20% RH and t=0 seconds and the final angle at 20% RH and t = 1440 seconds. The results shown in figure 27 indicate the contact angle hysteresis is on the order of 2° and does not change with increasing spherical component of substrate stress.

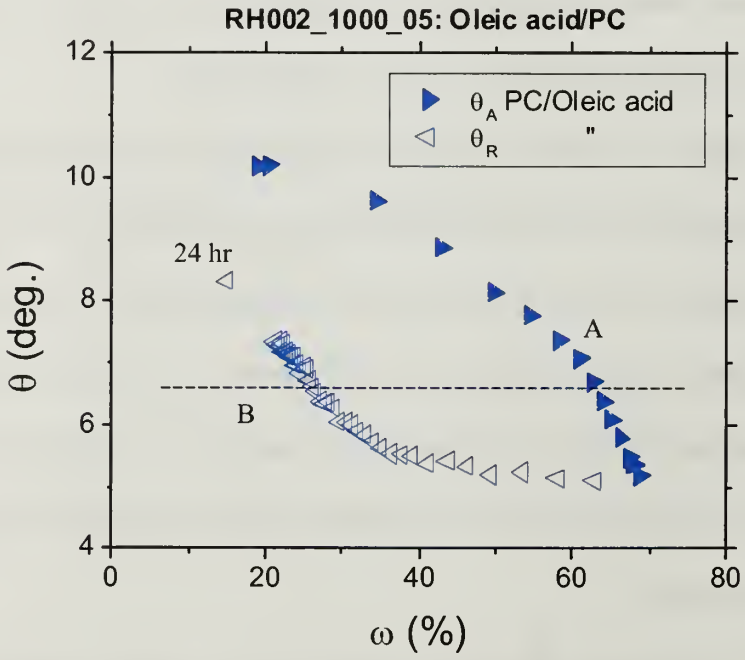

Figure 25: Plot of contact angle with respect to relative humidity for polycarbonate/oleic acid. Three phase line advances as humidity increases and recedes as humidity drops.

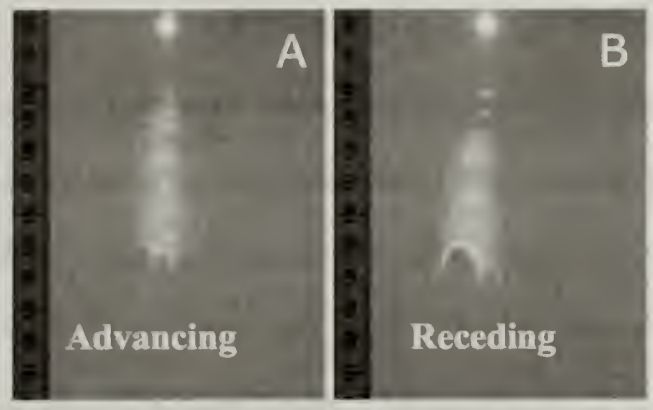

t = 2700 s	t = 18300 s
$\omega = 62.5\%$	$\omega = 21.3\%$
$\theta_A = 7.08°$	$\theta_R = 7.34°$

Figure 26: Advancing and receding refraction images from Figure 2.23 observations of advance and recession of three-phase line driven by vapor phase relative humidity. Advancing β-refraction spot shows that the advancing three-phase line is more uniform than the receding three-phase line.

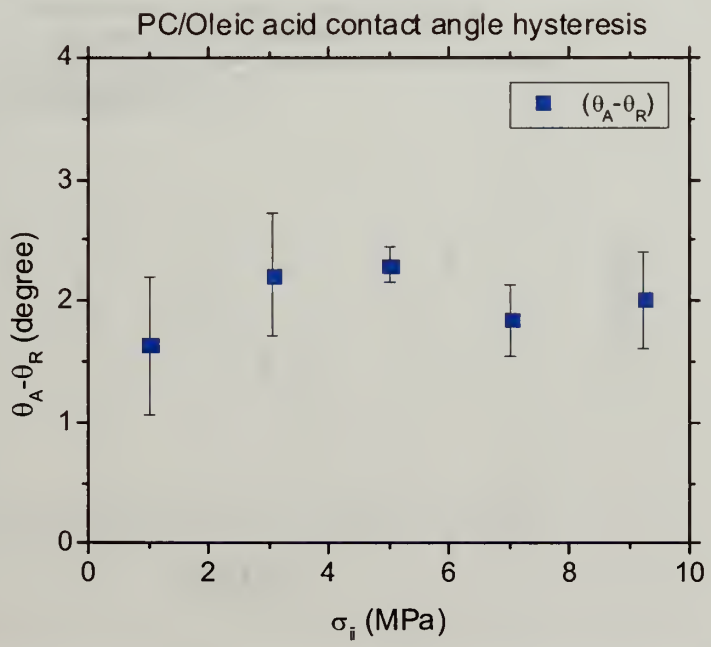

Figure 27: Contact angle hysteresis of polycarbonate/oleic acid driven by cycled relative humidity. Magnitude of contact angle hysteresis is on the order of 2° and is constant with substrate stress.

Contact Angle with Respect to Stress: Goniometry

Figures 28, 29 and Tables 4 and 5 show the equilibrium advancing contact angle measured by goniometry for increasing spherical stress for PC-oleic acid and PC-dubutyl phthalate systems respectively. In both cases there is a weak trend toward a minima in contact angle with stress. This is not expected in the PC-dibutyl phthalate combination as the critical stress for unbounded swelling predicted by the Gent equations is well below the levels of stress applied in these observations. For the PC-oleic acid observations the apparent minima is at stresses similar to the range of critical stress predicted by the Gent equations. Given the given the low precision of the goniometry technique, usually considered to be in the range of ±2-5°, the PC-oleic acid contact angle wrt stress observations cannot be considered to indicate the transition to unbounded swelling.

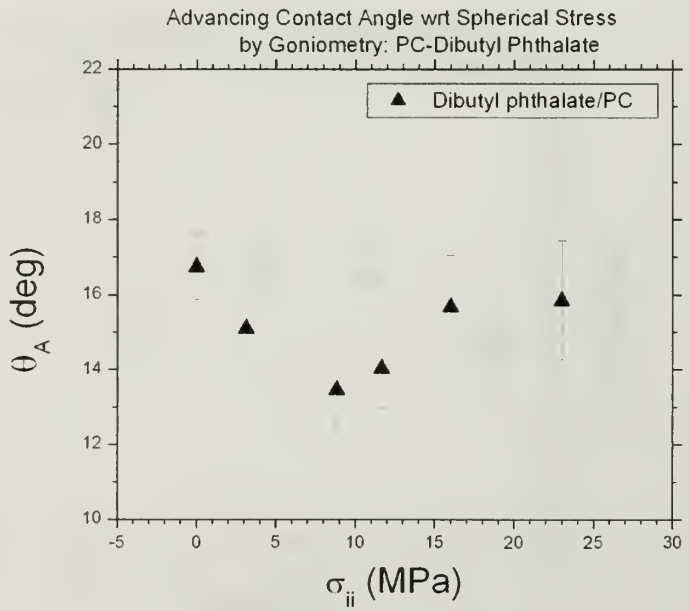

Figure 28: Advancing contact angle as a function of spherical stress for a polycarbonate-dibutyl phthalate sample under fixed displacement uniaxial tension. Angles are the mean of three observations on separate samples observed by video goniometer.

Table 4. Polycarbonate-dibutyl phthalate data for contact angle with respect to spherical component of stress. Angles are the mean of three observations on separate samples observed by video goniometer.

ε (mm/mm)	σ_{ii} (MPa)	θ_A (deg.)	***Std. Dev.*** (deg.)
0.00	0.00	16.74	0.780
0.398	3.16	15.10	0.699
1.113	8.83	13.46	0.805
1.467	11.64	14.03	0.931
2.02	16.02	15.67	1.208
2.90	23.0	15.85	1.401

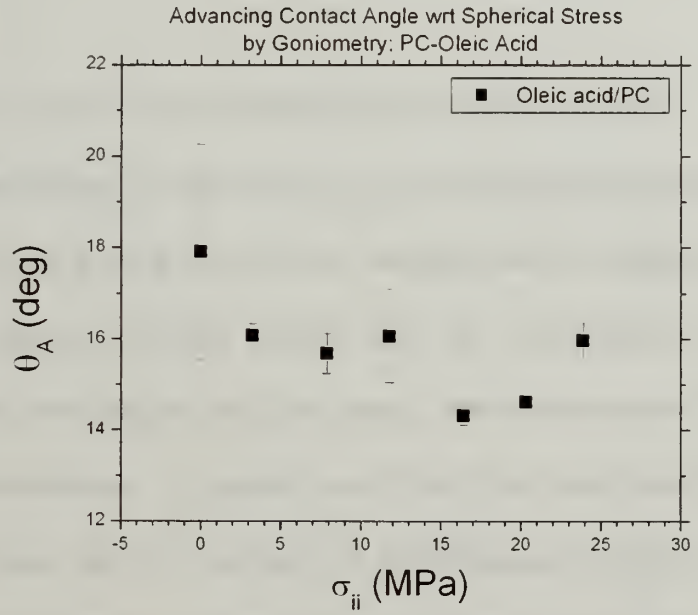

Figure 29: Advancing contact angle as a function of spherical stress for a polycarbonate-oleic acid sample under fixed displacement uniaxial tension. Angles measured by video goniometer. The filled squares denote the mean of three observations and the error bars indicate 1 standard deviation on the mean. There is a trend to a minima at ~15 MPa but given the precision of this method, usually considered to be ±2-5°, the data do not indicate the Gent hypothesis transition to unbounded swelling.

Table 5. Polycarbonate-oleic acid data for contact angle with respect to the spherical component of stress acting on the sample. Angles are the mean of three observations observed using a video goniometer.

ε (mm/mm)	σ_{ii} (MPa)	θ_A (deg.)	***Std. Dev.*** (deg.)
0.00	0.00	17.91	2.08
0.410	3.28	16.08	0.220
1.000	7.89	15.68	0.386
1.490	11.80	16.07	0.910
2.07	16.45	14.32	0.184
2.56	20.3	14.63	0.1170
3.01	23.9	15.97	0.337

Strain Condition at Crazing Under Constant Stress conditions

During the refraction observations of contact angle with respect to substrate stress the strain condition of the substrate was monitored using an LVDT (Linear Voltage Differential Transformer). The time resolved refraction images collected during the experiments to determine contact angle also allow length-scale consistent determination of the time and strain at which craze damage is commensurate with the LASER wavelength λ. This is accomplished by observation of the onset of diffraction fringes caused by the parallel array of closely spaced crazes. Figure 30 illustrates the refraction/diffraction geometry and compares early and later time refraction images for an polycarbonate- oleic acid sample at a hydrostatic stress of ~13 Mpa. The early time image has no diffraction fringes while the later time image shows distinct diffraction fringes. The transition to diffraction fringes is observed before crazes in the tensile sample are easily visible to the naked eye.

Figure 31 shows the strain response of dry polycarbonate samples under fixed load conditions identical to those used for the observations of contact angle strain and time to crazing with respect to substrate stress. For the time scale of these experiments substrate creep or inelastic strain is only significant at spherical stresses larger than 9-10 MPa.

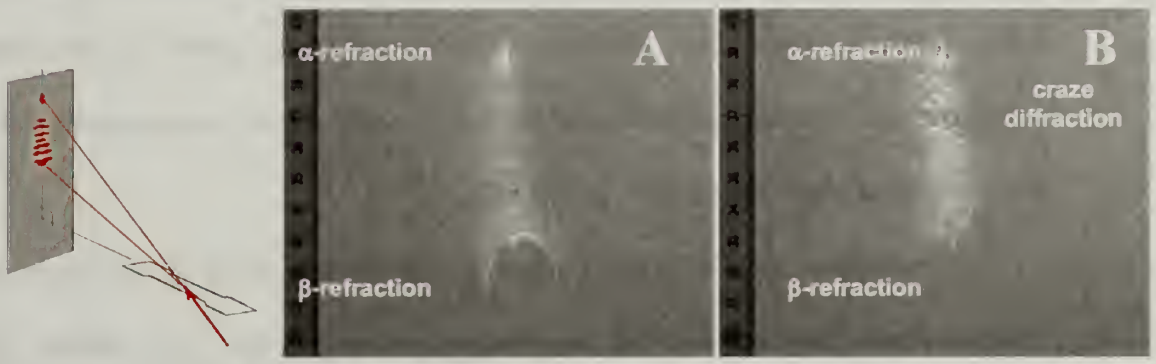

Figure 30: A) Refraction image prior to the onset of crazing. B) Diffraction fringes in refraction image indicate growth of craze to a length scale commensutrate with the 632 nm wavelength LASER.

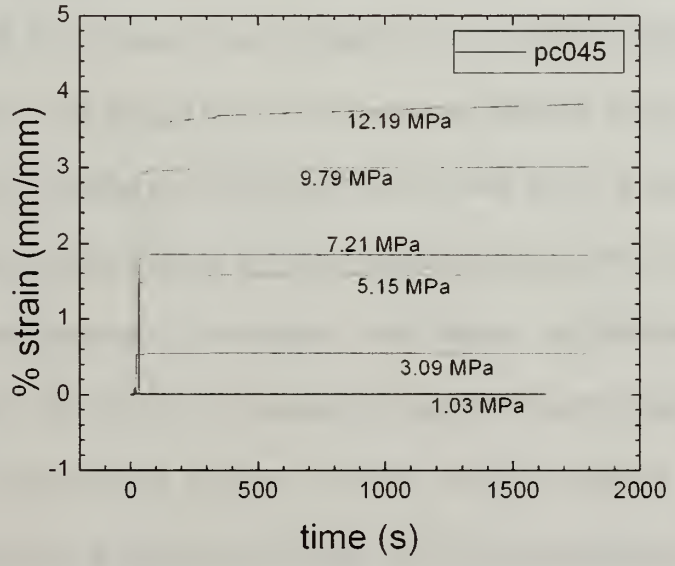

Figure 31: Fixed uniaxial load strain response of polycarbonate samples used in contact angle-stress observations, time to craze initiation and strain at crazing experiments. Labels indicate the spherical component of stress acting on the tensil specimen. For the 1800 second duration of the experimental observations substrate creep is significant only for spherical stresses above 9MPa.

Total strain at crazing

Figure 32 shows plots of hydrostatic stress vs. the total strain at crazing for both polycarbonate-dibutyl phthalate and polycarbonate-oleic acids systems. The strain at crazing increases with stress for both. The dibutyl phthalate-polycarbonate crazes at lower levels of stress than the oleic acid-polycarbonate system In the oleic acid-polycarbonate observations the lowest level of stress at which crazing occurred during the duration of the experiments was ~11-12 MPa.

Comparison of the inelastic strain at crazing data of figure 33 shows markedly different behavior between the two surface-active liquids. The dibutyl phthalate-polycarbonate system crazes at essentially zero inelastic strain at all stress levels tested larger than zero. The oleic acid-polycarbonate system shows two distinct regions of inelastic strain response. At hydrostatic stress below 11-12 MPa the inelastic strain at crazing is highly variable between 0.1-0.6 %. At stress levels above 12 MPa the inelastic strain at crazing is less than 0.1%. This transition in behavior occurs near the midpoint of the range of critical spherical stress predicted by the Gent hypothesis for PC-oleic acid.

Kambour and Arnold have respectively proposed critical strain criterion, and critical inelastic strain criterion for crazing [55, 56, 57, 61]. It should be noted that any attempt to correlate a critical strain or inelastic strain using the data from the present research is complicated by the fact that the ESC liquid is in contact with only a small area of the gauge length of the tensile specimen. In this experimental geometry the strain response to stress is a composite of the dry polymer response and that of the region affected by the surface-active liquid.

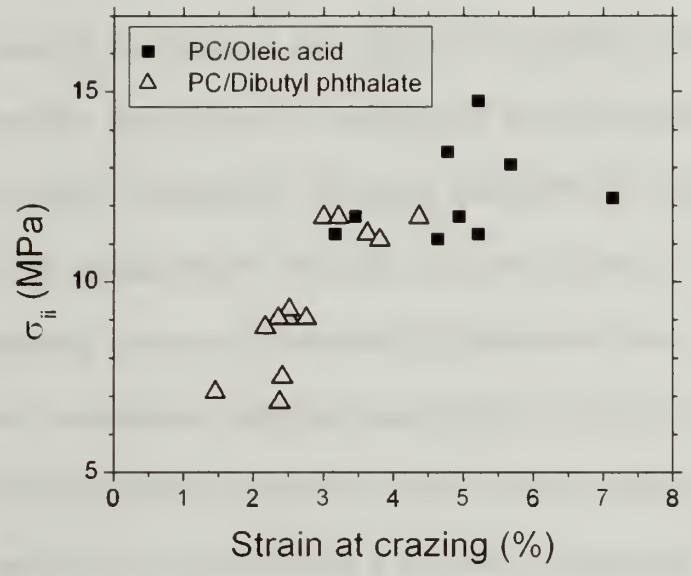

Figure 32: overall strain at crazing for oleic acid-polycarbonate and dibutyl phthalate-polycarbonate samples.

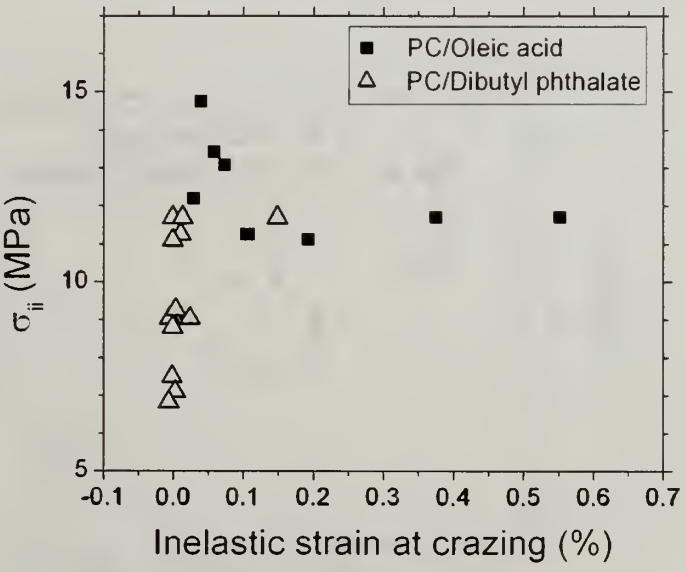

Figure 33: Inelastic component of strain for oleic acid-polycarbonate and dibutyl phthalate-polycarbonate samples.

Kinetics of Crazing Under Fixed Load Conditions

Time to initiation of crazing was observed for PC-oleic acid and PC-dibutyl phthalate during refraction observations of contact angle with respect to spherical stress using the onset of diffraction fringes in the refraction images previously described in Figure 30. The results, shown in Figure 34, results indicate that time to craze initiation increases as stress levels drop for both sets of materials. Comparison of the two groups shows that oleic acid at higher stress and dibutyl phthalate at lower stress actually cause crazing in a similar amount of time. The smaller solubility difference of dibutyl phthalate relative to polycarbonate makes it a more potent stress-cracking agent than oleic acid. The slope of both data sets is similar which suggests that the rate of change of crazing stress with time to crazing is similar for both pairs of materials.

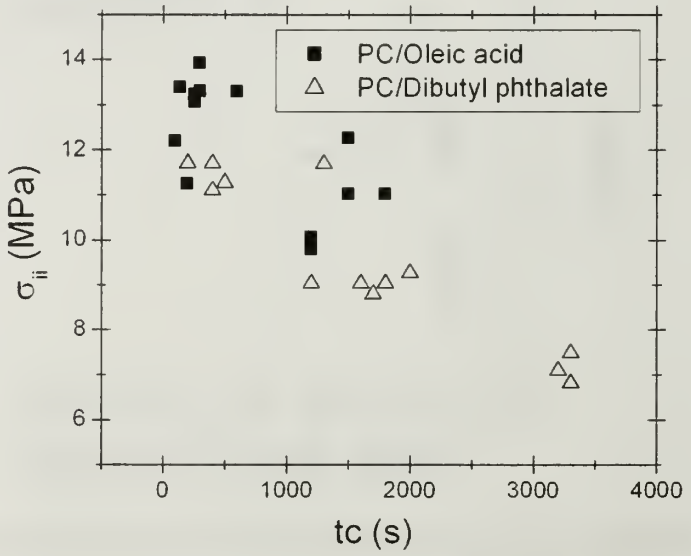

Figure 34: Time to onset of crazing for polycarbonate-oleic acid and polycarbonate-dibutyl phthalate systems. Crazing indicated by appearance of diffraction fringes.

Crazing Kinetics Under Fixed Displacement Conditions

The previous results suggested that it might be possible to normalize the substrate spherical stress vs. time to crazing data by the relative solubility difference between the ESC liquid and substrate material and collapse it onto a single curve.

An experiment was undertaken in which ASTM 638 Type 1 tensile bars of 3 mm thick polycarbonate were placed in a bending jig to result in 0.5%, 1.0% and 1.5% strain at the specimen midpoint and extreme fiber. A series of ester family ESC liquids with a range of solubility difference were applied to the samples and the time to crazing observed visually using a stereomicroscope at 5X magnification.

Figure 35 is a plot of substrate spherical stress divided by the square of the solubility difference between the ESC liquid and polycarbonate substrate vs. time to the initiation of crazing. The normalized stress term is an indicator of the thermodynamic potential for crazing to occur as large substrate stress and small solubility difference will both increase the propensity for crazing because of increasing dilatation of the physically entangled polymer network and increasing strength of enthalpic interactions between the polymer and liquid. These results indicate that in addition to thermodynamic potential for crazing the molecular size of the ESC liquid is an important factor affecting crazing kinetics. Crazing occurs in similar time scales for smaller molar volume ESC liquids at lower crazing potential and larger molar volume ESC liquids at higher crazing potential. The similarity between the four sets of data suggests that further normalization may be possible using diffusion constant as a parameter to account for the longer crazing times observed with larger molar volume ESC liquids.

Diffusion coefficients for polycarbonate in each of the ESC liquids were measured using the sorption method of Equation 10. The results are plotted in Figure 36 as diffusion constant with respect to the ratio of the molar volume of the assumed physical crosslink present in the polycarbonate and the molar volume of the ESC liquid. For this homolgous series of liquids Diffusion constant is roughly estimated to vary in proportion to $(V_m^{xl}/V_m^{S})^{5.8}$. Normalization of $\sigma_{ii}/(\Delta\delta)^2$ by this quantity shifts slower diffusing liquids to lower crazing potential and faster diffusing liquid to higher crazing potential collapsing the data reasonably well onto a single curve across approximately 3 orders of magnitude time scale as shown in Figure 37.

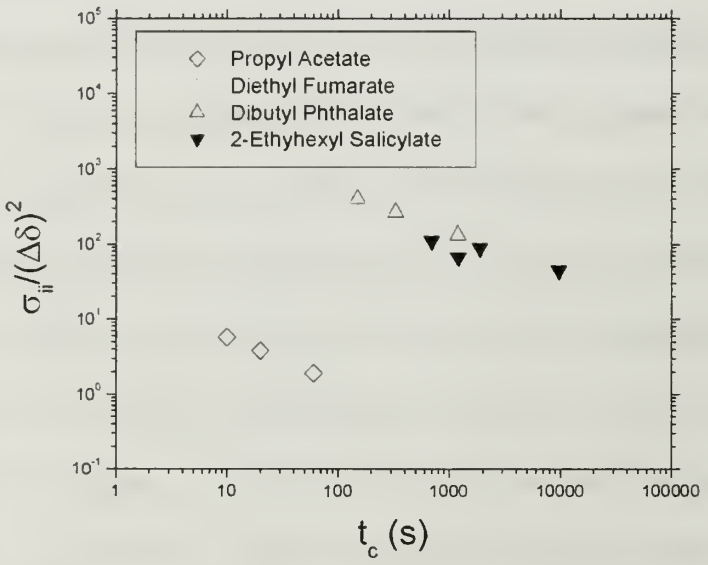

Figure 35: Plot of spherical stress on a PC substrate normalized by the square of the solubility difference between ESC liquid and polymer plotted vs the time to initiation of crazing under fixed displacement loading in a two point bend test. The σii/(Δδ)2 term is representative of the thermodynamic potential for swelling. The plot shows that in addition to thermodynamic potential, the size of the ESC liquid molecule is an important factor in crazing kinetics. A large molecule at high swelling potential crazes in a similar time as a smaller molecule at lower swelling potential.

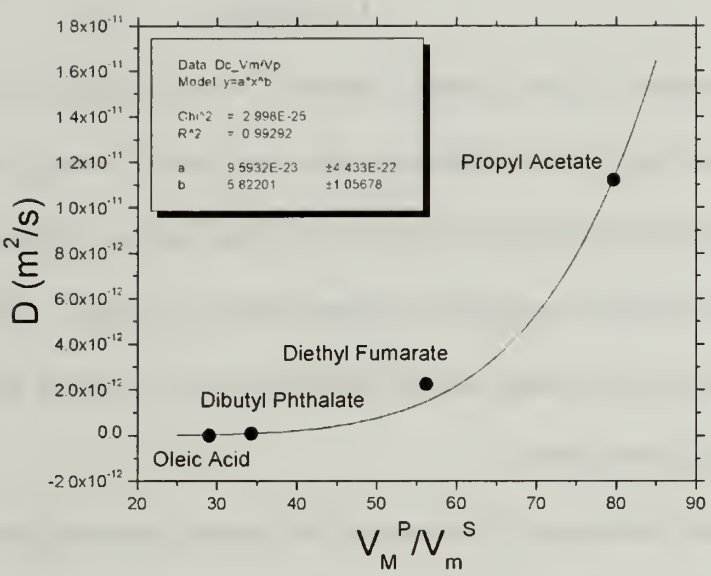

Figure 36: Estimate of the relationship of diffusion coefficient to the ratio of physical crosslink molar volume (V_m^P) and ESC liquid molar volume (V_m^S). A power law fit indicates that diffusion coefficient varies roughly in proportion to $(VmP/ VmS)^{5.8}$.

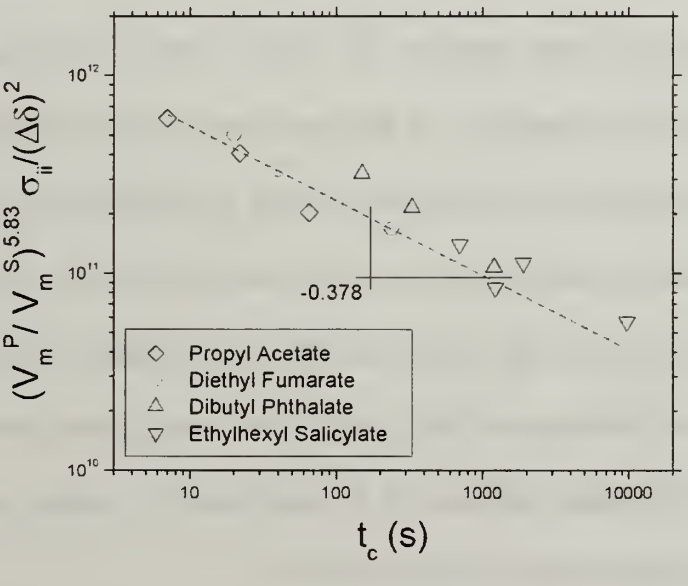

Figure 37: Plot of $(V_m^P/V_m^S)^{5.8} \bullet \sigma_{ii}/(\Delta\delta)^2$ with respect to time to crazing for a homolgous series of ESC liquids on a polycarbonate substrate.

Conclusions

A variation of the Contact Adhesion Test was used to evaluate the effect of substrate stress state on the substrate solid-vapor surface energy. For the relatively low levels of stress used in this work solid-vapor surface energy is found to be independent of substrate stress with a magnitude of approximately 42 mJ/m^2 . The result indicates that the three phase contact angle may be directly used as a possible indicator for changes in the solid-liquid interactions.

A novel technique for measuring three phase contact angle using the refraction of light through the lens of a sessile drop was developed. The method is objective and precise. It is appropriate for measurement of angles from ~20° to 0° with precision of approximately ±0.5°. This represents nearly an order of magnitude improvement over conventional goniometer methods. The β-spot portion of the refraction images also give an indication of the irregularity at the three phase line that may be due either to physical of chemical roughness of the substrate surface and the differences in the configuration of the three phase line during advance and recession are clearly evident in the β-refraction. The use of a LASER light source also allows determination of the time at the onset of crazing due to diffraction of the light by the closely spaced array of crazes. This is a length scale consistent indicator of the early tages of crazing as diffraction is evident before the crazes are visible to the naked eye.

Comparison of mass uptake observations and time resolved three phase contact angle observations were used to evaluate whether contact angle is an appropriate metric for swelling of the polymer substrate. The mass uptake experiments indicate that dibutyl phthalate does spontaneously swell polycarbonate while oleic acid does not. Time

resolved observations of contact angle for the two systems showed that the dibutyl phthalate-polycarbonate system exhibited strong decay in contact angle with time while the oleic acid-polycarbonate system exhibited little or no decay in contact angle with time. In this way three-phase contact angle has been found to be a sensitive metric for swelling. The refraction method has also been used to show the sensitivity of contact angle to relative humidity.

In an effort to observe the transition to stress induced swelling embodied in the Gent hypothesis observations of advancing contact angle with respect to substrate stress for dibutyl phthalate and oleic acid have been made using both the refraction method and conventional goniometer methods. Both sets of data indicate that three phase contact angle is independent of substrate stress for these materials. Contact angle hysteresis of the oleic acid-polycarbonate system was also evaluated. The advance and recession were driven using changes in relative humidity yielding contact angle hysteresis as a function of stress. The results of these experiments indicate that wetting behavior is not a good indicator for the unbounded swelling transition embodied in the Gent hypothesis.

The strain condition at crazing was monitored during contact angle observations for the oleic acid-polycarbonate and dibutyl phthalate-polycarbonate systems. As has been previously observed [3], the critical total strain at crazing decreases with decreasing difference in solubility between the polymer and ESC liquid. Separation of the total strain at crazing into elastic and inelastic components reveals markedly different behavior for the two surface active liquids. The dibutyl phthalate-polycarbonate system crazes at ~zero inelastic strain for all stress levels larger than zero. The oleic acid-polycarbonate system show two distinct regions of response. At spherical stress of less than 11-12 MPa

the inelastic component of strain at crazing is highly variable while at higher stress levels the inelastic strain component again falls to essentially zero. This transition in response occurs at a stress state commensurate with the Gent hypothesis prediction for these materials.

The time to the initiation of crazing was monitored during contact angle observations using the length scale consistent onset of diffraction fringes as an indicator of crazing. As has been previously observed the time to crazing decreases as stress level increases or solubility difference decreases. This result suggested that normalization using the solubility difference might yield a consistent stress-time response for different systems.

To probe this idea a series of fixed displacement crazing experiments was undertaken using polycarbonate substrates in a two-point bend configuration exposed to a series of ester family ESC liquids chosen to cover a range of solubilities. The substrate stress state was normalized by the square of the solubility difference between the polymer and ESC liquid. This term is considered to represent thermodynamic potential for crazing. The crazing response of the four ESC liquids tested showed an interesting result: Large ESC liquid molecules at high thermodynamic potential for crazing and smaller ESC liquid molecules at low thermodynamic potential craze in similar time scales. The inference is that larger molecules take longer to migrate into the polymer and so plasticization and subsequent crazing are delayed in spite of high crazing potential. In addition smaller ESC liquid molecules will have a larger plasticizing effect.

Measurement of the diffusion coefficients of the liquids allowed correlation diffusion coefficient to the molar volume of the ESC liquids relative to that of the

physically crosslinked polycarbonate network. Diffusion coefficient was found to vary roughly as $(V_m^P/V_m^S)^{5.8}$. Normalization of the crazing potential term by this quantity resulted in a reasonable collapse of the data into a single curve over three orders of magnitude of crazing time. This result is limited to relatively short time scales and a series of similar ESC liquids on a single substrate, but if it can be shown to be more general the approach has the potential to be used as a crazing failure criterion.

CHAPTER 3

ENVIRONMENTAL DEGRADATION OF POLY-P-PHENYLENE BENZOBISOXAZOLE FIBERS

Introduction

Poly-p-phenylenebenzobisoxazole (PBO) is one of a family of lyotropic liquid crystalline polymers that orient easily into extended chain configurations producing fibers with excellent strength and modulus. PBO polymer was originally developed by the U.S. Air Force to replace metals in space and aviation applications for its excellent thermal stability and chemical resistance [81, 82]. PBO fibers typically have exceptionally high tensile strength (5.8GPa), stiffness (180-270 GPa), and relatively low density (1.54 g/cm^3) [83, 84, 85]. To date, they are the strongest commercially available organic polymeric fibers. Consequently, they are ideal candidates for many military applications. Research and development of this material is being actively pursued for applications in high-performance fiber composites, protective garments, and personnel ballistic armors.

Recently (late 2001), Toyobo published some disconcerting results regarding the susceptibility of PBO fibers to degradation when exposed to relatively mild conditions [85]. In particular, the strength of PBO fibers decreases even at a temperature less than 100°C in high humidity. After 100 days at 80% relative humidity, and 80°C more than 40% of the strength is lost and the trend in the data suggest that additional losses can be expected with continued exposure. Subsequent data from Toyobo show that PBO fibers are also susceptible to degradation when exposed to sunlight. Both AS and HM fibers lost more than 50% of their strength after only 3 months exposure at Ohtsu, Japan. Toyobo

has shown similar results with 100 days' exposure in a Xenon arc weather-ometer. Subsequent to these reports, numerous news reports reiterating these concerns in PBO products have been reported [86]. It should however be noted that even with 50% degradation of fiber tenacity PBO fiber still has specific strength comparable to that of aramid fibers.

Potential Mechanisms of Degradation

The reported propensity of PBO fibers to degrade when exposed to sunlight and/or high humidity is somewhat surprising given the apparent high thermal and chemical stability of this class of polymers. To date, no mechanism has been confirmed to explain the degradation in mechanical properties of PBO fibers when exposed to these relatively mild conditions. However, potential mechanisms can be proposed after considering how commercial fibers are made.

The polymer is made in a polycondensation reaction from 1,3-diamino-4,6-dihydroxybenzene dihydrochloride (DADHB) and terephthalic acid (PTA) in a polyphosphoric acid solution as in Scheme 1 [87]. Commercial PBO fibers are spun using a dry-jet wet spinning process [88]. In this process, PBO polymer solution containing 10-20% of PBO in polyphosphoric acid (PPA) is extruded through a spinneret into a coagulation bath (water). This is followed by washing, drying and, in the case of HM fiber, heat treatment. The structure formed during the coagulation stage of the above dry-jet-wet-spinning process of PBO fiber is an interconnected network of highly crystalline oriented microfibrils, the width of which is 8-10 nm [89,90,91,92]. These microfibrils are the fundamental structural elements of the fibers. PBO fibers after the coagulation stage contain a great amount of the non-solvent in 25% by weight or more, and they will

exhibit a volume change on drying as the fibrillar network collapses yielding the "as-spun" fiber [93, 94]. Consequently, there are inevitably defects present in the fibers, which have been verified with small angle x-ray scattering and transmission electron microscopy [95, 96, 97]. The voids are elongated in the direction of the fiber axis.

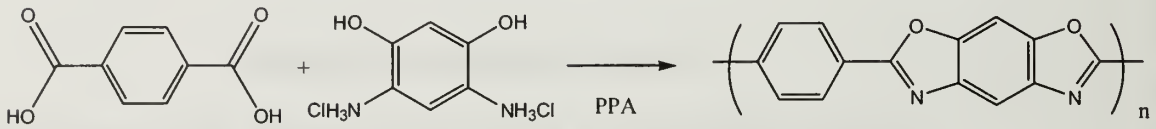

Scheme 1: Polycondensation of a 1,3-diamino-4,6-dihydroxybenzene dihydrochloride (DADHB) and terephthalic acid (PTA) in a polyphosphoric acid solution to form PBO polymer.

Physical Mechanisms of Fiber Degradation

There are two primary reasons for us to focus on the physical aspects of fiber degradation. First, the fiber tenacity is related to the concentration of defects, which act as fracture initiation sites. The process used to manufacture PBO fiber results in the introduction of microvoids and these defects act as fracture initiation sites. Secondly, because there are only relatively weak van der Waals and electrostatic forces acting between chains, slippage of adjacent crystalline domains and fibrils is possible. Within this context the size and concentration of the microvoids, or even the interconnectivity between fibrils and microvoids may be changed under certain conditions and the resulting morphology will influence the mechanical properties of PBO fibers.

Based on the unique molecular, crystalline and supermolecular structures of PBO fibers, we hypothesize that any environmental factor, which can loosen the structure of PBO fibers such as introducing defect on fiber surface or inside the fiber, weakening the interfacial adhesion between fibrils and crystals, will decrease the mechanical properties

of PBO fiber [98]. On the other hand, any treatment that can densify the structure of PBO fiber such as increasing the orientation and size of crystals and fibrils, increasing the interfacial interactions between fibrils, may increase the mechanical properties of PBO fibers [99].

Chemical Mechanisms of Fiber Degradation

It has been observed that the coagulation of PBO and PBT in methanesulfionic acid (MSA) solution with water was accompanied by a decrease of polymer intrinsic viscosity (IV). Berry and coworkers proposed that the IV decrease was not due to chain scission but was a result of inter-chain association, with the chains in parallel array in the aggregates [100, 101]. In contrast more recent studies indicate that PBO in polyphosphoric acid (PPA) or methanesulfonic acid with residual water followed by coagulation in water underwent bond cleavage to generate carboxylic acid and o-aminophenol functional groups [102]. A study of PBT fibers exposed to Lewis acids showed bond cleavage and a decrease in molecular weight [103]. Bourbigot proposed the chain cleavage during pyrolysis of PBO and showed that oxygen plays a great role in the thermo-oxidative degradation, which is an initiator of degradation [104]. In addition the conjugated structure of the PBO mer and π - π stacking in PBO crystals may make the fiber intrinsically photosensitive [105].

Although these severe conditions are unlikely to be encountered in normal applications of PBO fibers, we must consider that PBO fiber is spun from a solution of poly-phosphoric acid, and it is reasonable to expect that trace amounts of phosphoric acid remaining in the fibers after spinning combined with wet or humid environments, sunlight and oxygen may promote hydrolytic and oxidative degradation similar to that

noted by Morgan and coworkers in poly-p-phenylene terephthalamide fibers containing trace quantities of H_2SO_4 [106, 107, 108].

In this work we have explored the physical and chemical degradation pathways for fibers exposed to aqueous environments, acidic environments and radiation in the ultraviolet-visible light range. Subsequent to exposure fibers were characterized using a broad range of mechanical and physical tests including tensile testing, scanning electron microscopy (SEM), small angle X-ray diffraction (SAXD), wide angle X-ray diffraction (WAXD) and attenuated total reflectance infrared spectroscopy (ATR-FTIR).

Experimental

Materials

PBO fiber used in our experiment is Zylon AS, which was supplied by US Army Soldier System Command at Natick, MA. The physical properties of the fiber can be found in reference [85].

Methods

Liquid and vapor water exposure

Tows of PBO AS fibers were placed in liquid de-ionized water in a dessicator and held at 50°C in a darkened oven. PBO tows were exposed to water vapor by placing them above de-ionized water held within a second dessicator and held at 50°C in the same oven. The relative humidity within the dessicator was measured at 90% under these conditions. Fibers were periodically removed from both environments and dried at room temperature prior to any characterization experiments.

Phosphoric acid exposure

Phosphoric acid solutions of 0.5M, 1M and 1.8M concentration were prepared from de-ionized water and 85% o-phosphoric acid obtained from Fisher Chemical and used as received. Tows of PBO AS fibers were placed in the acid solution within a closed darkened container at 20°C. Tows of fiber were periodically removed and dried for 24 hours under vacuum prior to tensile testing or other characterization.

UV-Visible light exposure

Controlled exposure to UV-Visible light was accomplished using a Suntest CPS + weatherometer. The radiation source is a xenon lamp with a broad spectrum filter that closely simulates the distribution of wavelengths and intensity found in natural sunlight (figure 38). The fibers were exposed to at 750 W/m^2 and held at a constant temperature of 50°C. Fibers used for tensile testing were single fibers fasted to cardboard backing with an epoxy adhesive and placed in the CPS+ Suntester sample tray, fibers used for SEM, SAXD, WAXD and ATR-FTIR were tows each comprised of approximately 160 single fibers and placed in the sample tray in parallel arrays.

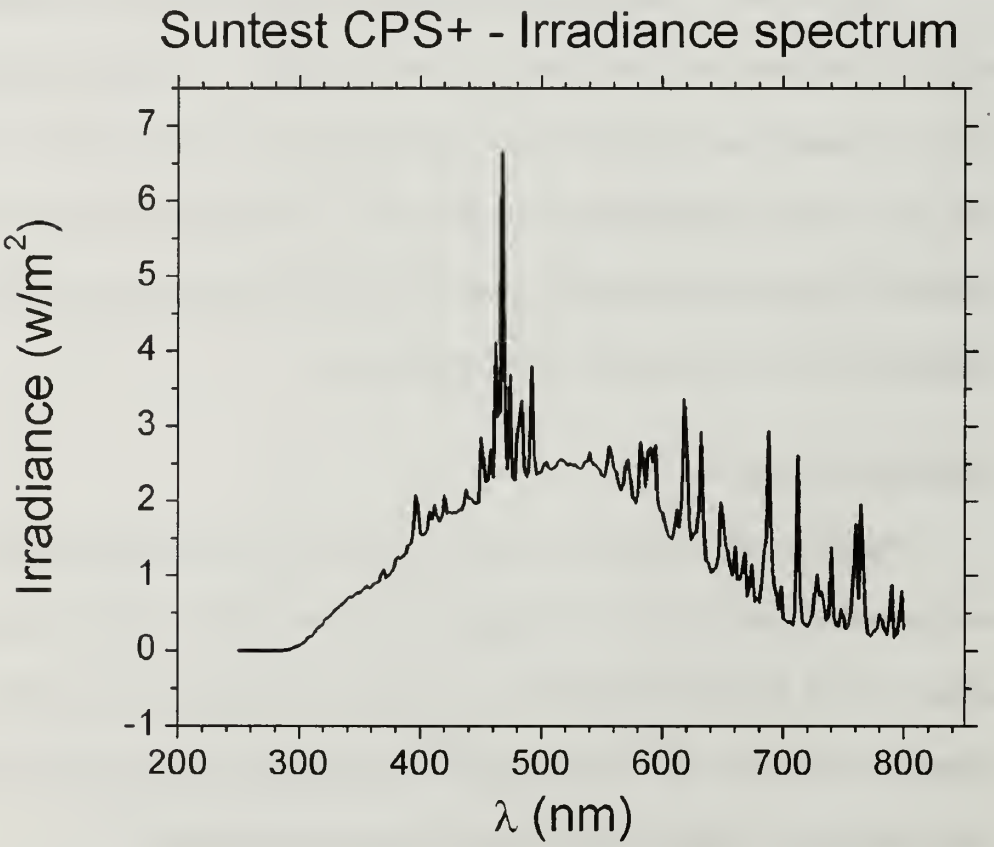

Figure 38: Irradiation spectrum of the Suntest CPS + weatherometer used in PBO fiber degradation studies.

Tensile testing

Mechanical properties were measured using an Instron 5800 series tensile tester equipped with a 50N load cell. Tests were conducted on single fiber specimens using a crosshead velocity of 10 mm/minute and a gauge length of 20mm. The fiber tensile specimens were prepared according the methods suggested in ASTM standards C 1557-03 and D 3379-75 [109, 110]: Single fibers were glued at each end to a cardboard backing using Huntsman Araldite 2012 five-minute epoxy. Two holes in the cardboard backing were used to ensure a consistent gauge length. The center section of the backing was removed after the sample was fixed in the Instron grips. The grips were arranged with pin ends between the Instron foundation and the gripping surface so the direction of applied force and fiber axis were coincident. Compliance of the Instron 5800 load train was measured using the method outlined in ASTM standards D 3379-75 and C 1557-03 [210,110] using identical fiber and sample mounting techniques. The results are shown in Figure 39 and the system compliance (C_s) was found to be approximately 1.152×10^{-4} m/N. Elastic modulus and elongation data were adjusted accordingly. Each reported value of fiber tenacity, modulus and elongation at break is the mean from a population of at least 15 single fiber tests.

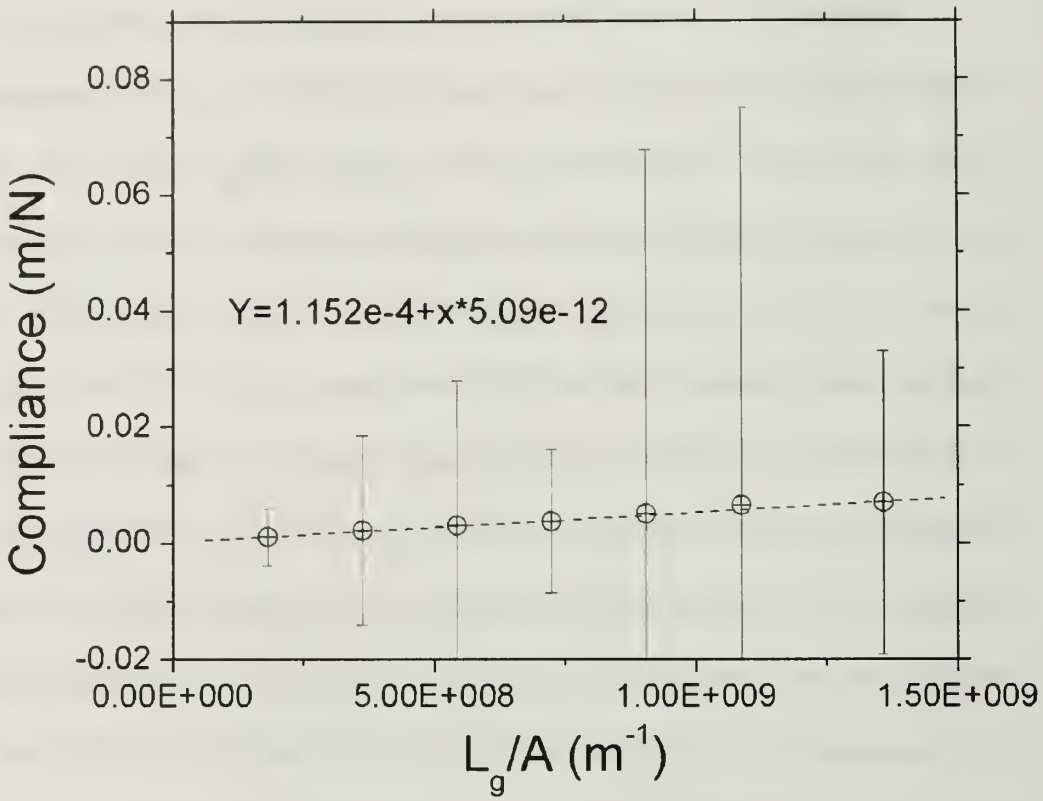

Figure 39: Instron 5800 system compliance (C_s). Determined from a plot of the initial slope of the fiber force displacement curve with respect to fiber gauge length normalized by cross sectional area. Ten PBO AS fiber samples were tested at each gauge length (20mm, 40mm, 60mm, 80mm. 100mm, 120 mm and 150mm) The intercept of the line is Cs (1.152x10-4 m/N) and the slope is 1/E for the as received PBO AS fibers tested (E≈196 GPa).

Scanning Electron Microscopy

SEM images were collected using an JEOL 6320FXV high resolution field emission cold cathode scanning electron microscope with semi-in-lens detector configuration achieving resolution down to 2 nm. Mounted fiber samples were sputter coated with gold in an argon atmosphere.

ATR-FTIR

ATR-FTIR spectra were collected using a Horiba HR800 Lab-Ram microscope with resolution of 4 cm^{-1}. Fiber samples were prepared by laying a tow of fibers over a clean glass microscope slide. Three spectra were collected at different locations on the sample for each type of fiber to assure that the spectra are truly representative of the fiber surface condition.

SAXD, WAXD

Small angle X-ray diffraction measurements were performed on tows of fiber using a Molecular Metrology® SAXD device. SAXD images were calibrated using a turkey tendon standard. Wide angle X ray diffraction measurements were performed using a Rigaku RU-H3R rotating anode X-ray diffractometer (operating at 1.2 KW, equipped with a multilayer focusing optic: point focus $(100\ \mu m)^2$; Osmic Inc., type CMF23-46Cu8) and a home built evacuated Statton-type scattering camera. Scattering patterns were acquired with a 10 cm × 15 cm Fuji ST-VA image plates in conjunction with a Fuji BAS-2500 image plate scanner.

Elemental analysis

Carbon, Hydrogen and Nitrogen analysis is performed by precisely weighing 2500-3500 μg of sample and combusting it at 1000°C in oxygen over a platinum catalyst, using a standardized Exeter Analytical 240XA Elemental Analyzer based on the modified Pregl-Dumas method. Phosphorus analysis is performed by a standard inductively coupled plasma emission spectroscopy (ICP) technique, after 20-30 mgs of sample is

precisely weighed and digested with a combination of sulfuric and nitric acids. A Leeman Labs, Direct Reading Echelle (DRE) ICP was utilized.

Results & Discussion

Liquid and vapor phase water exposure results

Figure 40 shows the results of tensile testing for PBO AS fibers immersed in liquid water at room temperature and conditioned in 90% relative humidity at 50°C respectively. Both treatments decrease tenacity and the strain at break while modulus remains essentially constant. Two key facts are evident; First, moisture alone does degrade the mechanical strength of the fibers, and, fibers immersed in liquid water degrade more quickly than those in humid environments.

The Figure 41 SEM micrographs compare the surfaces of (A) un-degraded PBO fiber with (B) PBO AS fiber exposed to liquid water for 270 days at 50°C and (C) PBO AS fiber exposed to 90% relative humidity @ 50°C for 270 days. In both types of moisture-exposed fiber, the development of long defects parallel to the fiber axis is observed. One possibility is that these surface defects are a result of voids increasing in size with water exposure and breaking through the fiber surface. Comparison of SEM micrographs for control fibers and water exposed fibers indicates no very large changes in fiber diameter.

To examine changes in the size and shape of voids within the fiber bundle small angle x-ray diffraction patterns of a tow of parallel fibers were collected as a function of liquid water exposure. Figure 42 shows the diffraction pattern and Guinier plot for liquid water exposed PBO AS fiber. Previous work by Kitigawa et al. in which TEM images of axially sectioned fiber were compared with the correlation length from SAXD has confirmed that the equatorial streak is due to scattering by needle-like voids oriented parallel to the fiber axis rather than the fibrillar elements [95].

Table 6 shows the correlation length (D) of the void cross-section according to the wide angle region of a Guinier plot, and from the small angle regions, the radius of gyration of the void cross section (R_3), the mean-length across the void cross section parallel to the incident beam (l_2), and the void cross sectional area (S_3). The final three quantities calculated using the analysis of Shioya and Takaku et al. previously applied to carbon fibers [111].

D, R_3, l_2 all remain approximately constant while S_3 increases with exposure implying that the fiber has become swollen. If we approximate these voids as needlelike ellipsoids oriented parallel to the fiber axis and with major and minor cross-sectional axes randomly arranged through the fiber it is reasonable that R_3 does not change significantly as the fiber swells. This quantity is an indication of the radius of gyration of the void cross-section. If the cross section is elliptical the radius of gyration will change as the root mean square of the major and minor axes. With the high aspect ratio of major and minor axes indicated by the comparison of S_3 and D, the change in the length of these axes is small and so will be the effect on R_3. The random orientation of the major and minor axes of the void cross section means that D and l_2 will remain approximately constant because the decrease in mean length of a void cross-section oriented with major axis parallel to the incident beam will be offset by the increase in mean length of one with major axis perpendicular to the incident beam. The increase in S_3 implies that the void cross sections are becoming more circular with exposure. These observations taken in context with the SEM evidence of figure 41 for increased void size are consistent with a permanent swelling of the fibrillar bundle by moisture.

This change in fiber structure is a very likely cause for the large drop in fiber strength and elongation at break. As the fiber swells voids may be growing along the fiber axis. Adjacent voids may be coalescing to form larger defects and new voids may be nucleating. The net effect is to increase the number of defects present in a given fiber. The increased size of the defects leads to a greater number becoming preferential sites for fracture initiation leading to a decrease in fiber strength and elongation at break

As mentioned previously, it has been suggested that residual phosphoric acid within the fiber may play a role in the degradation process when water is present. ATR-FTIR was used to evaluate possible chemical changes in the PBO fiber with exposure to water. Figure 43 is a comparison of spectra for a PBO AS control fiber and various durations of liquid water exposure. The IR spectra show no indication of any chemical changes near the fiber surface. The Figure 44 WAXD data also indicate no changes on the length scale of the crystalline domains within the PBO fibrils.

Taken together these SEM, SAXD, ATR-FTIR and WAXD observations suggest that there is no large degree of chemical degradation occurring with exposure to water and that the mechanism of degradation appears to be primarily a physical one in which the fibrillar elements within the fiber are loosened. The resulting increase in size of the micro-void defects present in the fiber is the primary cause of the loss in strength. The effect of residual phosphoric acid may not be chemical in nature but instead an increase in the equilibrium quantity of water absorbed by the fiber. However, work assessing the effects of phosphoric acid on fiber morphology and strength shows that even small concentrations accelerate the loss of fiber breaking strength and elongation as well as the size of defects. It is not clear whether this is only due to an increase in the degree of

swelling or chemical degradation of a small amount of material at the surface of individual fibrils.

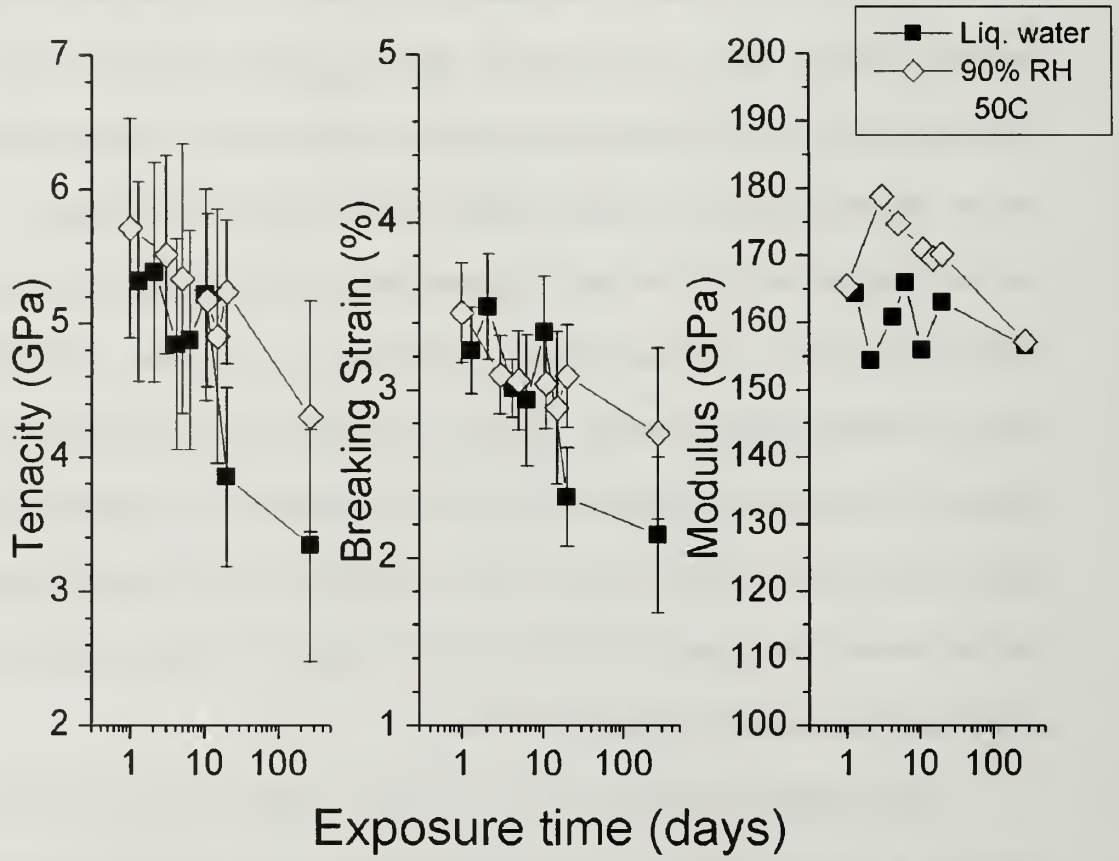

Figure 40:Tensile data for PBO fiber exposed to liquid water and 90% relative humidity at 50°C

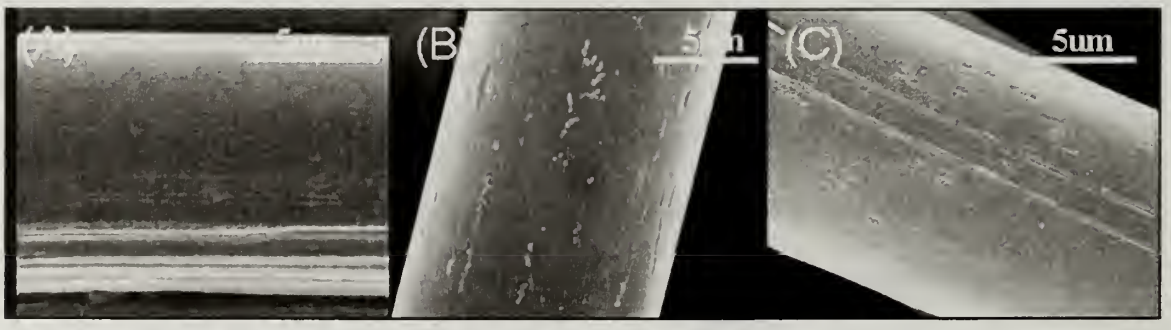

Figure 41:SEM micrographs: (A)PBO AS control, (B)PBO AS fiber exposed to liquid water (C) PBO AS fiber exposed to 90% relative humidity.

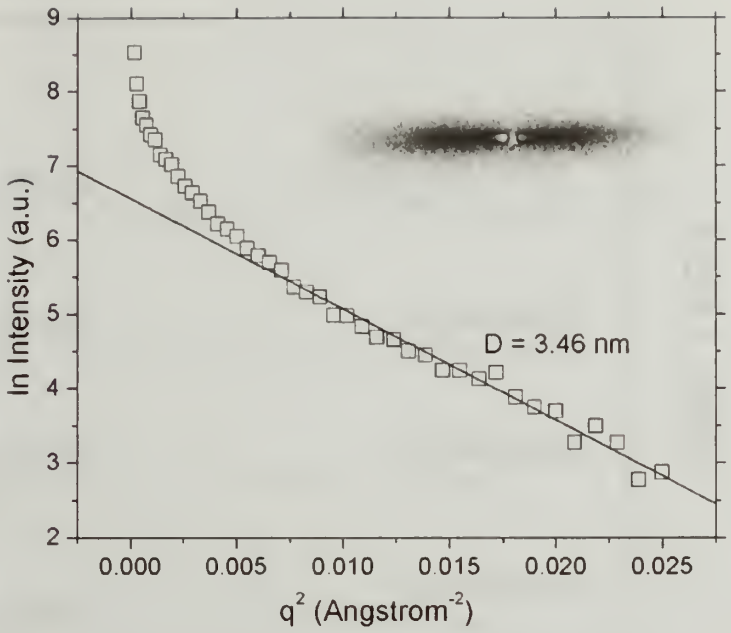

Figure 42: SAXD diffraction pattern and Guinier plot for PBO fiber exposed to liquid water.

Table 6: Results of Guinier plot and SAXD analysis for liquid water exposed PBO fiber. The increase in the average cross sectional area (S3) of the voids suggests a loosening of the fibrillar bundle on exposure to water.

Sample	*D(Å)*	*R_3(Å)*	*l_2 (Å)*	*S_3 (Å^2)*
Control	34.6	31.1	42.4	12.03
20 d	34.6	30.3	38.0	13.89
150 d	33.4	30.3	37.7	16.06
270 d	32.9	31.6	31.6	17.86

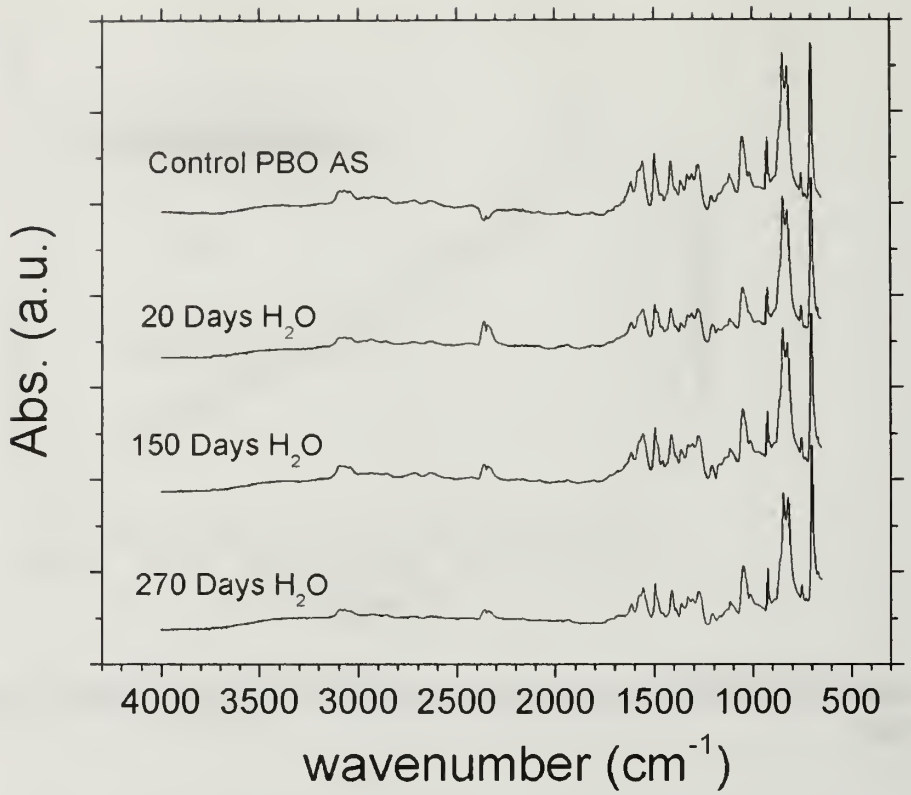

Figure 43:ATR-FTIR spectra for PBO fiber exposed to liquid water. There is no significant alteration of the chemical structure at or near the surface of the fibers. Spectra of fiber exposed to water vapor showed similar results.

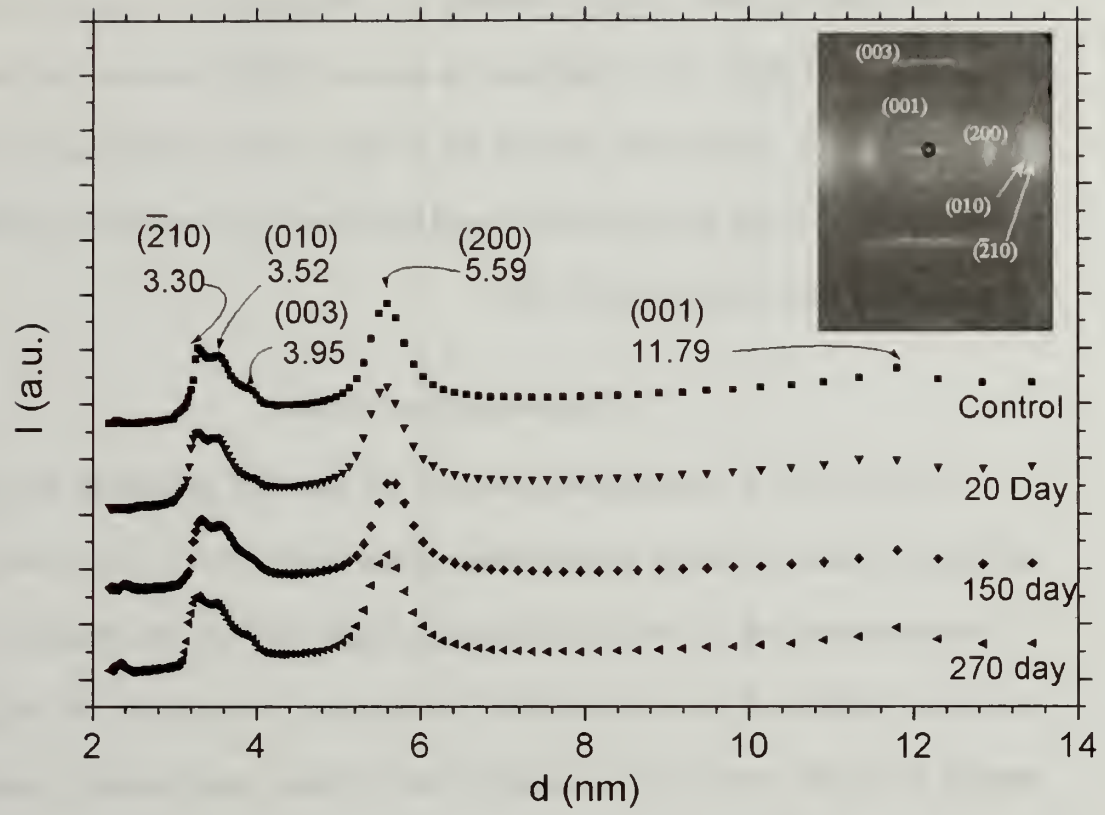

Figure 44: WAXD results for PBO AS fiber exposed to liquid water showing no effect on the crystalline structure of the fiber. Peaks in the diffraction have been assigned according to the work of Fratini et al. [92]

Effects of Residual Phosphoric acid

Elemental analysis was initially done on the Zylon AS fiber to determine if residual phosphoric acid resides in the fiber, and if so, establish a baseline quantity. Our results from these analyses indicate that an amount of residual phosphorus ranging between 0.3 – 0.4 wt% resides in the fiber. This result supports the hypothesis of hydrolytic or oxidative degradation involving phosophoric acid [103,106,107,108] in that residual phosphorous, which may be in the form of phosphoric acid is certainly present in the fibers.

In order to assess whether residual PA contributes the reported mechanical degradation, PBO fibers were conditioned in various PA/H_2O solutions for 24 hours at room temperature, dried under vacuum for 24 hours and characterized for residual phosphoric acid. Using this approach allowed for adjusting the residual phosphorus in a controlled way between 0.3 and 4.8 wt %.

Chemical exposure results

PBO AS fibers were exposed to 0.5M, 1M and 1.8M phosphoric acid solution. Subsequent elemental analysis of these fibers indicated 0.3 wt %, 0.7 wt % and 4.8 wt % of residual phosphorus for each concentration. Figure 45 shows the tenacity, breaking strain and modulus of the exposed fibers. At stronger concentration the reduction in strength is on the order of 75%. Based on our previous observations in which fiber strength was not significantly changed by 24 hour exposure to liquid water, it is reasonable to assume this drop in properties to be due to chemical degradation and not the physical mechanism proposed for water exposure. However, examination of the Figure 46 SEM results shows that there is certainly significant physical separation of fibrillar elements occurring.

The ATR-FTIR spectra shown in Figure 47 compare neat fiber with liquid water exposed and phosphoric acid exposed fiber. The broad band of absorbance centered ~3400 cm^{-1} increases slightly for the phosphoric acid/PBO samples and a new peak at ~3200 cm^{-1} occurs. The first are assigned to an amide N-H and the second to a cyclic N-H. There is also a small increase in absorbance at 1600-1700 cm^{-1} indicating the presence of amide carbonyls or other C=O.

While these spectra do not illuminate the exact chemical mechanism of degradation it is clear that a chemical reaction is occurring and they suggest that hydrolysis of the oxazole ring is the most likely route. The physical separation of the fibrillar elements observed in the SEM indicates that the chemical reactions with strong acid will accelerate the increase in defect size and number. This is relevant to the earlier observations for liquid water exposed fiber because it is possible that even very low concentrations of phosphoric acid will have a similar effect while not causing chemical change in enough of the fiber surface to show changes in the ATR-FTIR spectra.

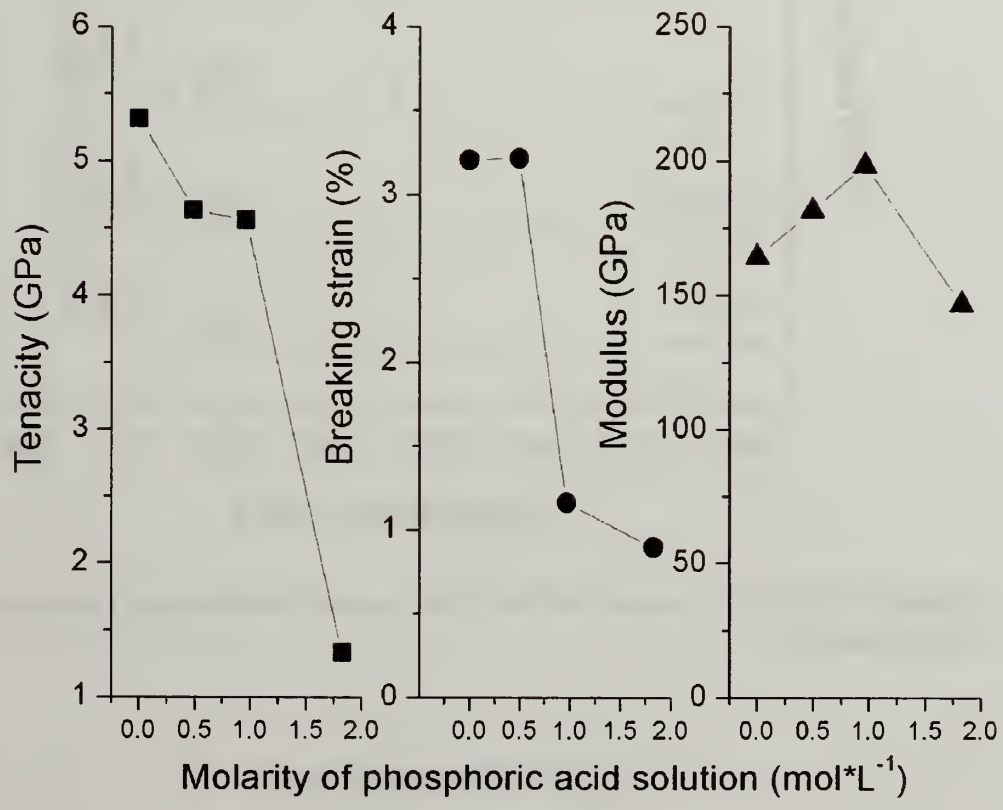

Figure 45: Tensile testing results for PBO fiber at 24 hour exposure to increasing concentrations of aqueous phosphoric acid solution.

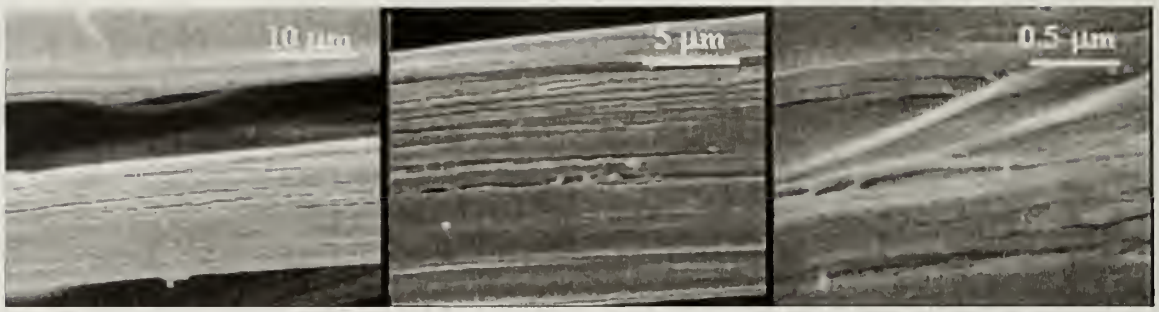

Figure 46: SEM results for PBO fiber exposed to 1.8M phosphoric acid.

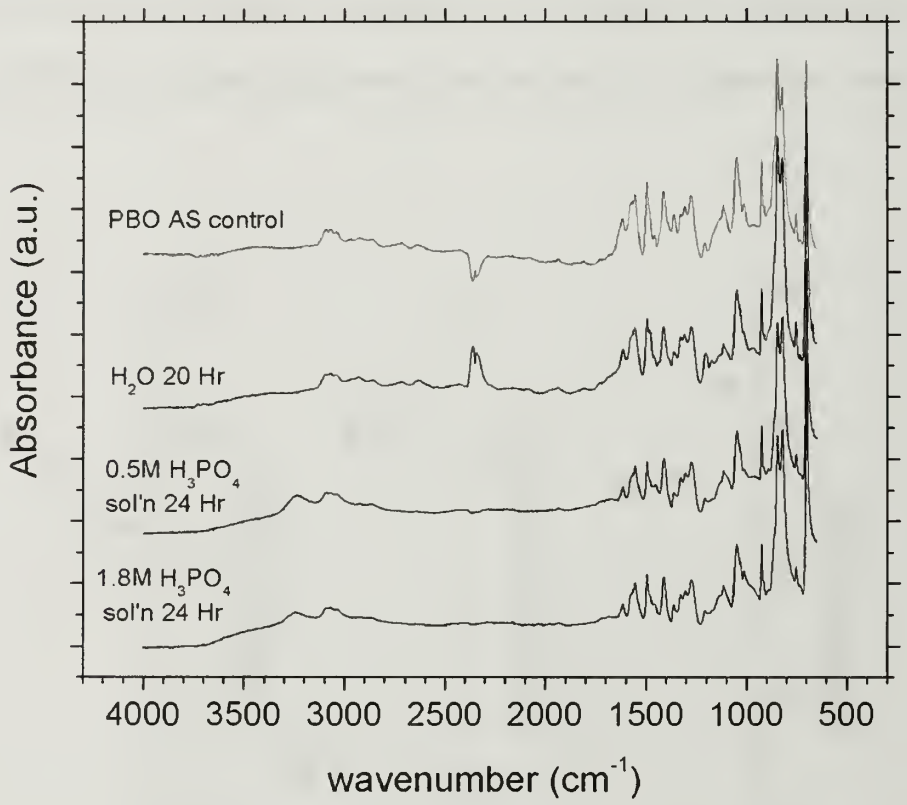

Figure 47: ATR-FTIR results for PBO Fiber exposed to increasing concentrations of phosphoric acid.

UV-Visible light exposure

Figure 48 shows the effects of exposure to UV-Visible light for three series of tests on PBO AS fiber. Tenacity and breaking strain are both reduced by approximately

40% after 300 hours of exposure with significant losses occurring after only the first 100 hour interval. The data for modulus shows that it is highly variable for a given exposure time but within these limits can be considered to remain approximately constant with UV-Vis exposure.

The SEM results of figure 49 compare pristine PBO AS fiber with fibers exposed to UV-vis light at 750 W/m^2 for durations of 150 and 270 days. As compared to the control fiber it can clearly be seen that the material on the UV-Vis exposed fiber surface has lost orientation. It seems very likely that the chemical nature of the polymer backbone is altered. While the depth of degradation cannot be determined from these images small degrees of degradation at the fiber surface will result in large changes in the cross-sectional area available to bear load. In addition work by Kitigawa [95] shows that PBO AS fiber has a core-shell structure in which the shell of approximately1-2μm depth has fewer voids and a higher degree of order than core region. Loss of a fairly small proportion of the fiber shell region may have a disproportionately large effect on fiber strength.

Possible degradation reactions include disruption and rearrangement of the oxazole ring, chain scission and/or cross-linking reactions. ATR-FTIR was used to determine the nature of the chemical changes near the fiber surface. The spectra are shown in figure 50. There are two clear changes observed with increased UV-Vis exposure: the increase in intensity of the broad band centered at ~3400 cm^{-1} that is attributed to the stretching vibrations of an secondary N-H bond, and the increase of a peak at ~1685 cm^{-1} that is assigned to the C=O of an amide linkage. Similar changes have been observed by Villar-Rodil et al. in their work monitoring chemical changes during

the early stages of thermal degradation [112]. These spectra suggest that the primary degradation pathway is disruption of the oxazole ring to form an amide likage. Chain scission is not indicated as one likely outcome of that reaction would be nitrile end groups and no such absorbance was observed in the IR spectra.

Table 7 shows the results of SAXD on UV-Vis exposed fiber. The Guinier correlation length D, Radius of gyration R_3, mean length of void cross section l_2 and void cross-section area S_3 appear to not be significantly altered by UV-Visible light exposure.

In total this data suggests that UV-Vis degradation is a chemical process occurring on the fiber surface in which the cyclic structure of the PBO backbone is disrupted and an amide linkage formed. This may occur without chain scission. Even a relatively small degree of degradation on the surface of the fiber will result in a significant loss in cross-sectional area, and in addition the material lost is from the highly ordered shell region of the fiber.

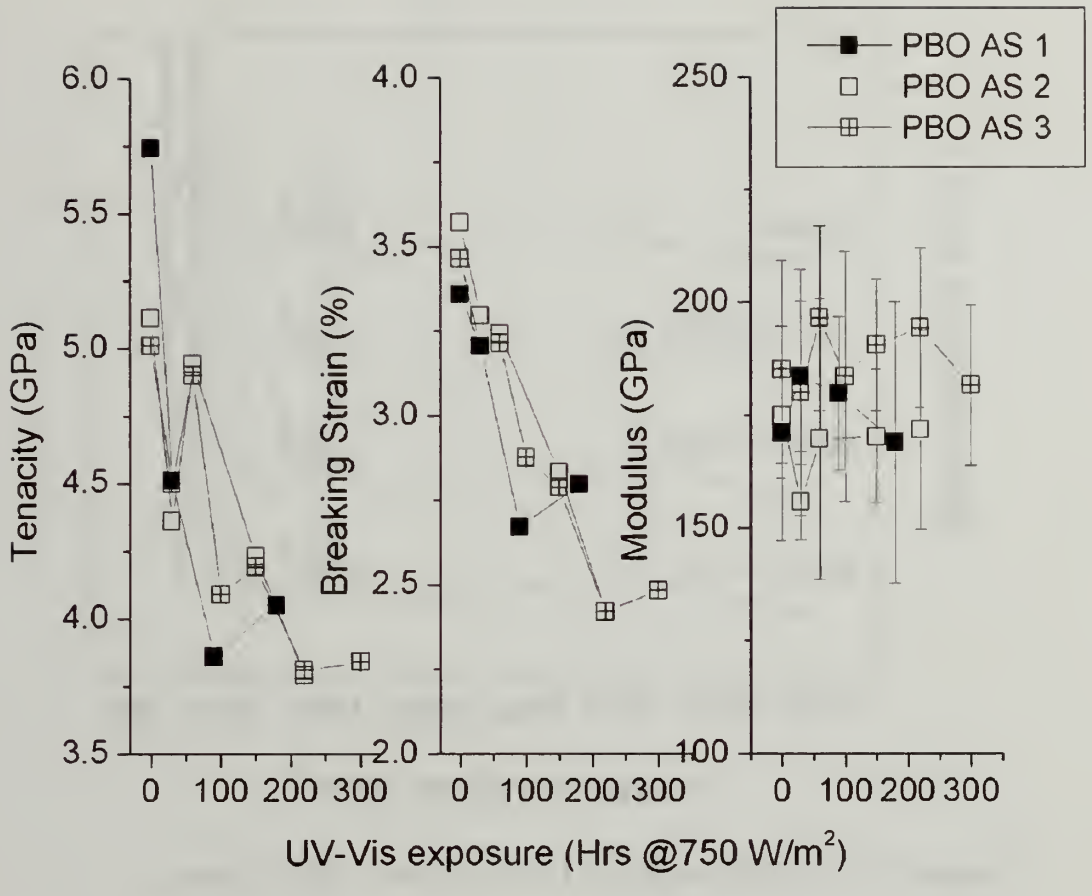

Figure 48: Tensile testing results for three series of PBO AS fiber exposed to UV-Vis light at an intensity of 750 W/m2. Error bars on modulus indicate one standard deviation about the mean value.

Figure 49: SEM results for UV-Visible light exposed PBO AS fiber

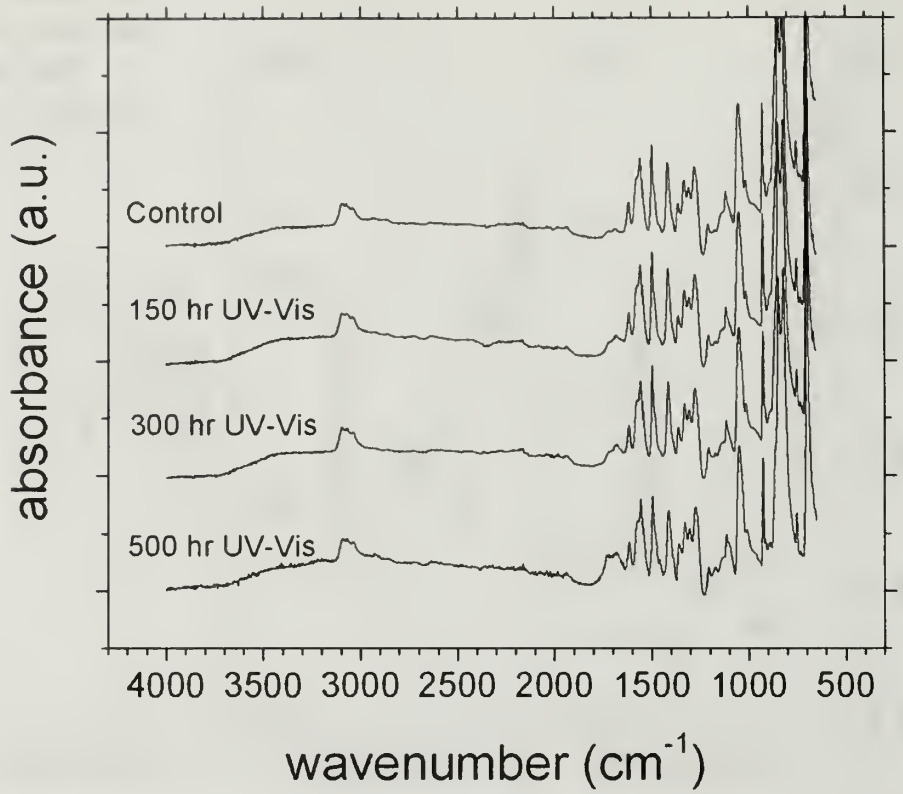

Figure 50: ATR-FTIR results for UV-Vis exposed PBO AS fiber.

Table 7: Results of Guinier plot and SAXD analysis for PBO AS fiber exposed to UV-Visible light.

Sample	*D (Å)*	*R_3(Å)*	*l_2 (Å)*	*S_3 (Å^2)*
Control	34.6	31.1	42.4	12.03
150 hr	32.7	32.4	42.5	18.83
200 hr	32.7	32.9	43.0	17.86
270 hr	33.7	32.1	42.3	14.80
300 hr	31.9	32.9	43.0	17.79

UV-Visible light exposure/Phosphoric acid exposure

Mechanical tests were conducted on filaments after UV-visible light exposure on both phosphoric acid conditioned and control samples. Figure 51 shows how the fiber tenacity and elongation change with increased exposure time. Note in both graphs, the squares are results on fibers without any conditioning in PA/H_2O solution, the circles are results from a 1M solution, and the triangles represent findings from a 1.8M solution. These, in turn, translate into residual phosphorus of 0.3, 0.7 and 4.8 wt % respectively. It can be seen in all cases that exposure to UV-visible light causes a reduction in both the stress elongation to break. Figure 51 also shows that small amounts of additional residual PA dramatically enhance the degradation in mechanical properties. This finding supports the first hypothesis in arguing that residual PA plays a role in the degradation process and underscores the importance of thorough extraction of residual PA in any attempt to alleviate fiber degradation. It should be noted that at 4.8% residual PA, the fibers were so degraded that measurements were not possible after more than 50 hours exposure. Modulus was measured and is in the range of 170 ± 5GPa and is independent of exposure time for fibers soaked in 5% and 10% PA/ H_2O solution. Only when the exposure time approaches 300 hours there is an indication of a slight decrease. However, for fibers soaked in 20% PA/H_2O solution, where the residual phosphorus concentration is 4.8wt%, the modulus decreases after soaking as well as after exposure, which is similar to the change in strength and elongation-at-break. Compared to the modulus, the phosphoric acid soaking and UV-visible light exposure samples show a more dominant influence on the fiber strength and elongation-at-break.

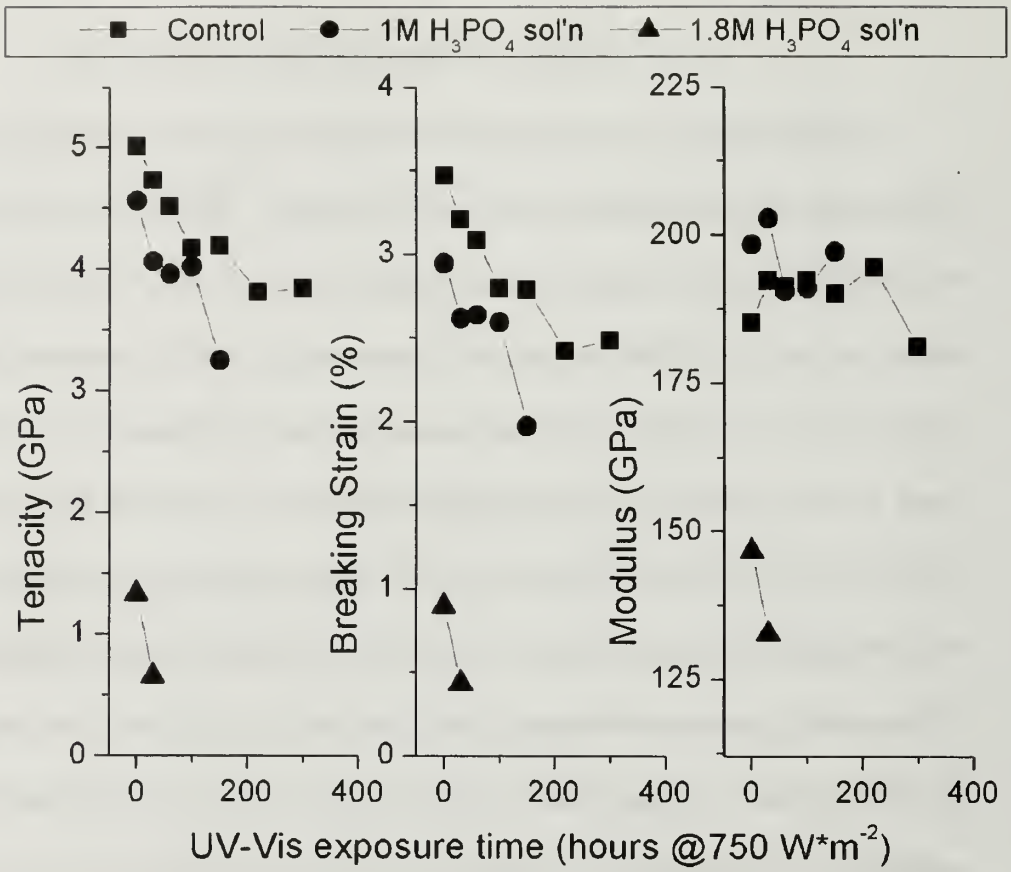

Figure 51: Mechanical properties of phosphoric acid exposed PBO AS fibers with UV-Visible light.

Conclusions

Degradation of mechanical properties from exposure to moisture appears to be primarily due to swelling of the fiber resulting in separation of the fibrillar elements and introduction of larger numbers and larger average size of defect. The defects act as fracture initiation sites and the strength of the fiber decreases exponentially with the increase. IR spectroscopy and wide angle X-ray experiments indicate that there is little or no chemical change occurring with exposure to water alone thereby casting some doubt on the role of residual phosphoric acid plays in fiber degradation.

However, the results of tensile testing, SEM and ATR-FTIR, in which PBO fibers are exposed to high concentrations of phosphoric acid show that in addition to a chemical degradation involving hydrolysis of the oxazole ring and leading to formation of cyclic amines and amide linkages, the presence of phosphoric acid seems to accelerate the separation of fibrillar elements within the fiber structure. This is relevant to the case of moisture exposure because even small amounts of acid due to residual phosphoric acid from the spinning process may be involved in the swelling observed for moisture exposure alone.

Degradation from exposure to radiation from thee UV-Vis spectrum shows significant loss of mechanical properties in a short period of time. The material near the fiber surface is chemically degraded and shows loss of orientation. Infrared spectroscopy indicates that the surface has undergone hydrolysis at the oxazole ring causing disruption of the ring structure and introduction of amide linkages. SAXD experiments probing defect size indicates that the axially oriented voids are changed but little by UV-Vis radiation and we conclude that the degradation is confined to the fiber surface and that

the drop in mechanical properties is due to the loss in cross-sectional area available to support load, particularly important is that the UV-Vis degradation is concentrated in the more highly ordered shell region of the fiber and that the core material that remains is less ordered and has a higher concentration of voids than the shell.

The effect of exposure to phosphoric acid followed by UV-Vis exposure shows that the loss of both breaking strength and elongation at break increased with exposure to increasingly acidic environments. These results support the idea that even the relatively low concentrations of residual phosphoric acid may play a large role in separating the fibrillar elements of the PBO fiber. Since the ATR-FTIR results indicate no significant chemical degradation of fibers exposed to liquid or vapor water the role of residual phosphoric acid may be primarily in increasing the equilibrium quantity of water absorbed by the fiber.

In sum we can say that the most significant degradation mechanism for PBO AS fiber is the loosening of the fiber structure due to moisture and/or phosphoric acid. UV-Vis degradation is significant also, but it should prove to be much easier to prevent this type of environmental damage than to exclude moisture in a typical service environment. Possible approaches to alleviate damage due to moisture include removing the residual phosphoric acid by washing the fibers with an inert solvent such as super-critical carbon dioxide, neutralizing the residual acid using small basic molecules and excluding moisture from the fiber surface with a barrier film that may also absorb radiation in from the UV-Vis spectrum.

It is useful to also consider that because the loss of strength is primarily due to loosening of the fiber morphology there is actually an opportunity to improve the

properties of PBO. Any post spinning process we can introduce that compacts the structure of the fiber, increases the size of the fibrillar elements and reduces the volume fraction of voids should be a route to improving the mechanical properties. Work exploring these approaches to alleviating environmental degradation and improving the base fiber properties are presented in the following chapter.

CHAPTER 4

STABILIZATION OF POLY-P-PHENYLENE BENZOBISOXAZOLE FIBERS

Introduction

In Chapter 3 the mechanisms of degradation of PBO AS fiber due to exposure to moisture, acidic environments and UV-Visible light (UV-Vis) were investigated in detail [113]. The mechanism of degradation for moisture was found to be primarily physical in nature. The loss in properties was accompanied by an increase in the size of voids within the fiber while ATR-FTIR spectroscopy revealed no chemical changes near the fiber surface. Exposure to strong acids in aqueous environments appeared to accelerate the separation of the fibrils within a fiber together with subsequent diminishments in tenacity. This suggests that any residual phosphoric acid present may contribute to degradation by moisture through its affinity with water by enhancing moisture adsorption or by a chemical reaction affecting small amounts of material at the surface of individual fibrils.

In contrast to the degradation due to moisture, the effect of UV-Vis radiation was found to be chemical in nature. This form of degradation is most likely due to the intrinsic photo-reactivity of the PBO polymer due to its highly conjugated chemical structure and π-π stacking within PBO crystals [114]. It should be noted that fibers exposed to concentrated phosphoric acid and subsequently exposed to UV-Vis radiation showed an increased loss of strength with higher concentrations indicating that there is a synergistic effect when both a challenging acid species and UV-Vis radiation are present.

The observation that strength is decreased by swelling of the fibrillar structure of the fiber and the increase in size and/or number of defects actually presents us with an opportunity to increase initial fiber strength through the application of forces that tend to compact the fiber structure and decrease the number and size of defects present. Because of the chemical structure of the PBO backbone there are no secondary chemical forces acting between the basic fibrillar structural elements of the fiber. Once a compacting force has been applied introduction of a secondary inter-fibril force that could maintain the compacted morphology and provide load transfer between fibrils might be beneficial both in terms of increasing initial fiber tenacity, compressive strength and resistance to degradation of strength by moisture.

Having a general concept of the degradation pathways for moisture, acidic environments and UV-Vis radiation, we propose some approaches to alleviate fiber degradation [115].

Super-Critical Fluid Extraction of Phosphoric Acid

Given that the presence of acid accelerates both degradation by moisture and UV-Vis radiation, extraction of residual phosphoric acid should improve fiber environmental stability. Super critical carbon dioxide has frequently been employed as an extraction medium due to its combination of low viscosity and negligible surface tension [116]. Herein, we investigate the use of super critical carbon dioxide ($scCO_2$) to directly wash the residual phosphoric acid out of the fiber.

A related approach investigated involves using $scCO_2$ as a transport medium to introduce the low molecular weight compounds pyridine, morpholine and trimethyl

phosphate in an effort to neutralize the residual acid, and potentially solubilize it in $scCO_2$ for subsequent extraction.

UV-Vis Blockers

For polymeric materials, a common method for improving weathering resistance or photo-stability is through the use of additives. During photo-oxidation, absorption of a photon by the polymer produces an activated species followed by a photophysical and chemical conversion of the activated species [117]. Therefore, various additives such as a UV reflector, a UV absorber, an excited-state quencher, or a free-radical scavenger and/or hydroperoxide decomposer have been long used in industry [118,119,120] to mediate UV-Vis degradation. The approach investigated herein involves coating of PBO fibers with different UV reflectors or absorbers, which are named UV blockers here. The UV blockers used are carbon black, exfoliated graphite, and a glassy TiO_2 created using sol-gel chemistry [121, 122,123].

Compaction

Several approaches to densify the fiber microstructure were undertaken. The first involves applying a twist to single fibers. Twist has long been known to improve the strength of staple fiber materials. It is also used in continuous yarn systems to force the assembly of single fibers to behave as a contiguous unit. It is well known that PBO fibers have a nano-fibrillar structure, which is very similar to that of spun yarns made from staple fiber except that it occurs over a different length scale [124, 125]. Generally, for yarns made from staple fibers, the strength shows a maximum while the extension to break continually increases with degree of twist [126, 127]. A second approach is to

apply hydrostatic pressure to the fiber in an $scCO_2$ environment with the intent to compact the fiber microstructure and allow the plasticizing ability of scCO to aid in the reduction of defects. Finally fibers were exposed to high temperature, tension and hydrostatic pressure in a $scCO_2$ environment simultaneously. The idea was to use the tension to orient the fiber elements more perfectly and allow the heat and $scCO_2$ to reduce the number and size of defects present.

PBO Polysiloxane composites

Prevention of swelling of the PBO AS fiber by moisture and maintenance of externally imposed compaction of the fiber morphology should have the effect of increasing the fiber's initial tenacity and resistance to degradation by moisture. The introduction of inter-fibrillar stabilizing forces has previously been studied with the aim of improving the low transverse mechanical properties of LC rigid rod polymers; Approaches include infiltration of the fiber with a high modulus glassy filler [128, 129], infiltration with an organic polymer phase during the coagulation step of the spinning process [130], creation of an interpenetrating rigid rod fibril-amorphous polymer network by spinning a fiber from a solution containing both a LC rigid rod polymer and an amorphous organic polymer [131, 132] and cross-linking the material in adjacent fibrillar regions [133, 134].

The work undertaken in this research differs from the previous studies in that it is not primarily aimed improvement of fiber transverse mechanical properties but instead at improving the environmental stability of PBO AS fiber by introduction of inter-fibrillar adhesive forces. In addition, rather than altering the nature of the spinning process this work is toward post-spinning processes applicable to stabilization of commercially

produced PBO fiber. Toward this end composites of PBO AS fiber and polysiloxanes crosslinked in a hydrosilation reaction have been prepared in super-critical carbon dioxide environment [135] according to Scheme 1. This approach takes advantage of the high solubility of siloxanes in $scCO_2$ by introducing relatively small molecular weight vinyl substituted polysiloxane prepolymer and hydride containing crosslinker to the fiber, swelling the fiber with the siloxane prepolymer and subsequently initiating crosslinking by introduction of a Karstedt's catalyst known to be highly soluble and robust in a $scCO_2$ reaction environment. The intent is that the resulting elastomeric PDMS will infiltrate the fiber, adhere to the fibrillar elements and provide a secondary force to prevent expansion of the fiber microstructure. Fiber impregnation with two resin systems were investigated: a low molecular weight vinyl substituted polydimethylsiloxane prepared by polycondensation (PVMS), and Sylgard 184 a commercially available PDMS system produced by Dow Corning Corp.

Experimental

Materials

PBO AS Fiber

The as-spun PBO AS fiber used was Zylon AS, which was supplied by US Army Soldier System Command at Natick, MA. The related properties of the fiber can be found in reference [136].

Extraction and Neutralization of Phosphoric Acid

Morpholine, pyridine and trimethylphosphate were purchased from Aldrich and used as received.

UV-Vis Blockers

Expanded graphite was supplied by Prof. Lawrence T. Drzal in Michigan State University. Carbon black is Black Pearl 800 provided by Cabot Corp. Glassy titanium dioxide was prepared from a sol-gel using titanium isopropoxide precursor in solution with absolute alcohol both purchased from Sigma-Aldrich and used as received.

Polymethylvinylsiloxane-polydimethylsiloxane Prepolymer (PVMS)

Polymethylvinylsiloxane-polydimethylsiloxane resin was prepared in a condensation reaction from dichlorodimethylsilane and dichloromethylvinylsilane in an aqueous solution at room temperature according to scheme 1. After completion of the initial condensation reaction the majority of the aqueous phase was removed, zinc acetate was added and the solution heated to 45 °C to reduce cyclic content and increase molecular weight. The product was then washed in absolute ethanol to end cap active chain ends and remove the remaining hydrochloric acid byproduct of the condensation reaction. The resulting vinyl substituted PDMS resin was combined with an appropriate quantity of 1,2,5,7-tetramethylcyclotetrasiloxane crosslinker ($D4^H$) such that there was a 1:1 equivalence of resin vinyl functionality and crosslinker hydrides. The reactants reactants used in preparation of the resin were purchased from Sigma-Aldrich and used as received. The $D4^H$ crosslinker was purchased from Gelest Corp. and used as received.

Scheme 1: Preparation of low MW vinyl substituted siloxane prepolymer

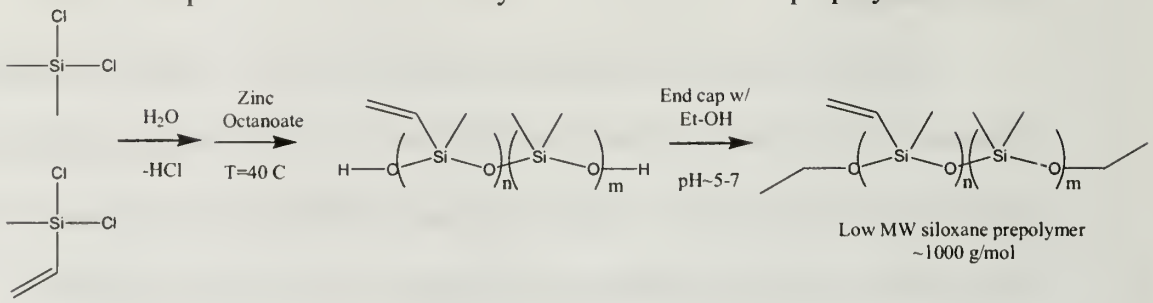

Sylgard 184 Polydimethysiloxane Resin

Sylgard 184 Elastomer Base is a product of Dow Corning Corp. It is composed of 60 or more wt. % dimethylvinyl terminated polydimethyl siloxane, 30-40 wt. % dimethylvinylated and trimethylvinylated silica and 1-5 wt % tetra(trimethylsiloxy)silane and 0.7 wt % xylene.

Sylgard 184 Polydimethylsiloxane Crosslinker

Sylgard 184 Curing Agent is a product of Dow Corning Corp. It is composed of 40-70 wt % Methylhydrosiloxane-dimethylsiloxane copolymer.

Methods

Super-Critical Carbon dioxide Extraction

Fiber washing was carried out in a custom-made high-pressure vessel designed to allow the circulation of CO_2. The details of this experimental apparatus are shown in Figure 52. In order to not damage or disturb the alignment of the fiber tows during washing, bundles of fiber approximately 12 inches in length were supported to an aluminium frame first, followed by insertion into the high-pressure vessel. A pressure regulator was used to control the CO_2 flow rate. Samples were washed in the vessel at

fixed temperatures and pressures with different times. After washing, the temperature was allowed to drop and the vessel was depressurized slowly. Washed PBO fibers were used for mechanical testing, elemental analysis and weathering experiments.

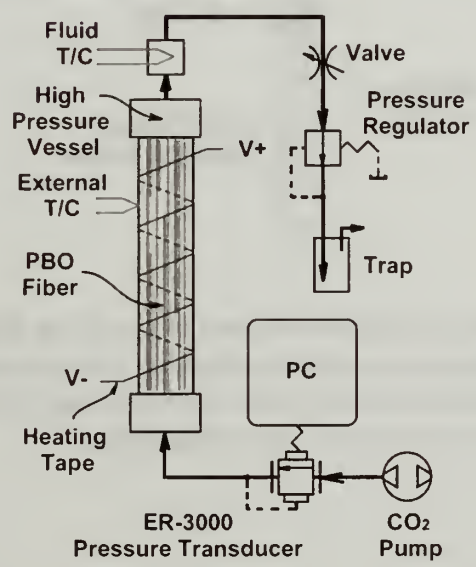

Figure 52: Schematic of device used for super-critical CO_2 extraction of residual phosphoric acid.

Preparation of PBO AS/Crosslinked PDMS Composites in $scCO_2$

Soaking and crosslinking of PBO AS/Crosslinked PDMS composites was carried out in the custom built device illustrated in Figure 53. A CO_2 pump supplied high pressure CO_2. The ER-3000 pressure transducer/controller was used to pressurize the removable high pressure reaction vessel and to ramp pressure down after the completed reaction. Once pressurized the reaction vessel was placed in an oven to attain the desired temperature and final pressure.

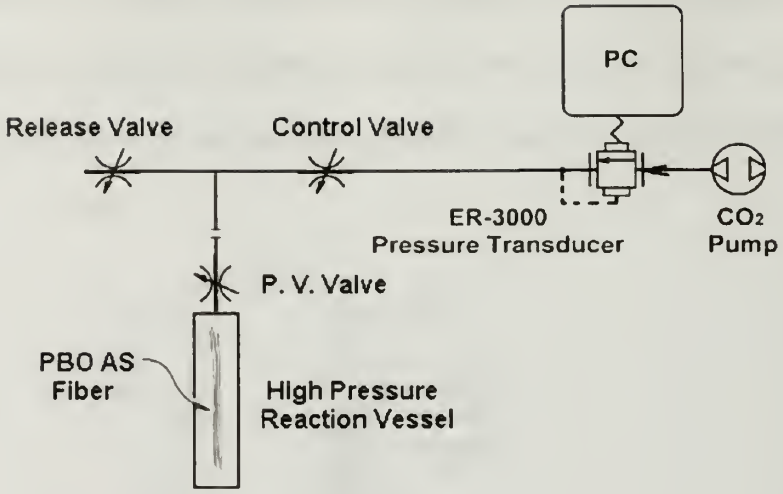

Figure 53: Schematic of the device used in preparing PBO AS/Crosslinked PDMS composites in a super-critical carbon dioxide environment. The high-pressure reaction vessel is removed after pressurization with CO2 and placed in an oven to maintain temperature and pressure above the critical point.

UV-Vis Exposure

Uv-Vis exposure procedures and equipment are identical to those described in Chapter 3.

UV-Vis Spectroscopy

UV-Vis spectra were collected using an Hitachi U-3010 spectrophotometer in transmission mode

Tensile Testing

Tensile testing procedures and equipment are identical to those described in Chapter 3.

SEM

Scanning Electron Microscopy equipment and procedure are identical to those described in Chapter 3.

ATR-FTIR

Attenuated Total Reflectance Fourier Transform Infrared Spectroscopy equipment and procedures are identical to those described in Chapter 2.

SAXD

Small Angle X-Ray Diffraction Equipment and procedures are identical to those described in Chapter 3.

Elemental Analysis

Elemental Analysis equipment and procedures are identical to those described in Chapter 3.

MALDI-TOF

MALDI spectra were acquired using a Reflex III MALDI-TOF (Bruker Daltonics) spectrometer. For MALDI analysis polysiloxane prepolymer resin was dissolved in a 10mg/mL solution with THF and applied to a stainless steel target in a matrix of 2-5-Dihydroxybenzoic acid.

NMR

^{1}H NMR spectra were collected using a Bruker DPX 300 instrument using $CDCl_3$ solvent.

Results and Discussion

Extraction of Residual Phosphoric Acid in Super-Critical Carbon Dioxide

In the work previously described in Chapter 3, elemental analysis indicated that an amount of residual phosphorus ranging between 0.3 – 0.4 wt% resides in the PBO AS fiber inferring the presence of residual phosphoric acid (PA). With exposure to an aqueous environment hydrolytic reactions with the weakly basic oxazole ring may cause disruption of the ring structure or chain scission . The pKa values for each phosphoric acid proton loss and the backbone structure of PBO are shown in Scheme 2.

Scheme 2: pKa values for dissociation of phosphoric acid protons

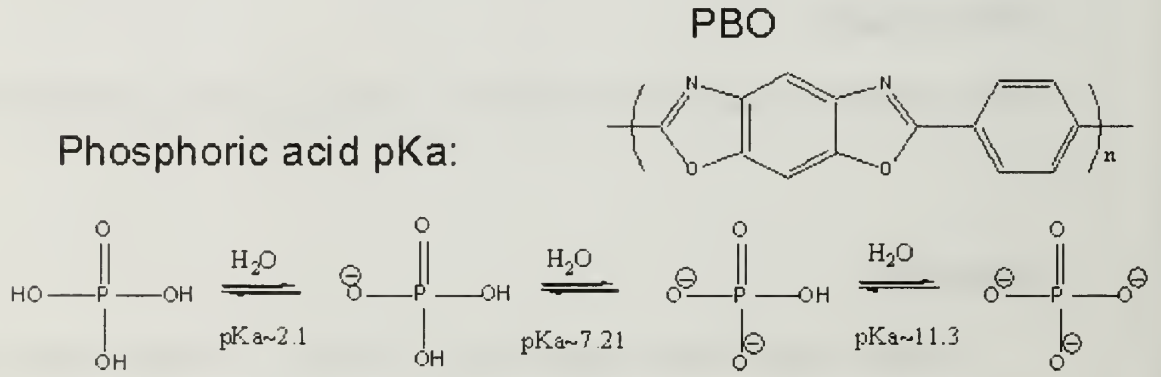

In an effort to extract the residual PA, PBO AS fiber was washed in supercritical carbon dioxide ($scCO_2$) at various conditions of temperature, pressure and $scCO_2$ flow rate using the device illustrated in Figure 52. Elemental analysis was subsequently used to measure changes in the quantity of residual phosphorus. The results presented in Table 8 show that as flow rate and temperature are increased, $scCO_2$ can remove part of the residual phosphoric acid in the fiber but cannot remove it completely. The concentration

of residual phosphorus can not be decreased below approximately 0.25 wt%-0.3 wt% suggesting that the highly crystalline PBO AS fiber may be only partially permeable to CO_2.

Table 8: Weight percentage of residual phosphorus remaining in PBO AS fiber washed in $scCO_2$ under varying conditions of temperature, pressure.

T (°C)	*P (psi)*	*Q (Lpm)*	*wt% residual PA*
Control	Control	Control	0.4
50	2500	5	0.4
100	2500	5	0.3
100	2500	10	0.25
100	5000	10	0.25

Single fiber tensile testing was used to assess the effect of washing in $scCO_2$ on mechanical properties. Figure 54 compares the tenacity of neat PBO AS fiber to fibers washed at a flow rate of 5 LPM, temperature of ~100 °C and pressure ranging from 2500 psi to 5000 psi. Exposure to $scCO_2$ does not appear to have a detrimental effect on the strength of the fibers. In fact, at pressures of 2500 and 3250 psi there appears to be a trend toward increase in fiber properties. This will be discussed further in this chapter's section on improving fiber mechanical properties via compaction of the fiber morphology. In addition, the SEM images of Figure 55 show that the surfaces of $scCO_2$ washed fibers are relatively unchanged as compared to pristine control fiber. The UV-Vis light stability of $scCO_2$ washed fibers was also evaluated. Figure 56 shows the single fiber tensile testing results for fibers exposed at 750 W/m^2 over a 300 hour duration. The

response of the neat fiber and the washed fiber is identical. This result supports the idea presented in Chapter 3 in which it is supposed that UV-Vis degradation is not primarily related to the presence of residual phosphoric acid but is instead due to the intrinsic photo-reactivity of the highly conjugated structure of PBO.

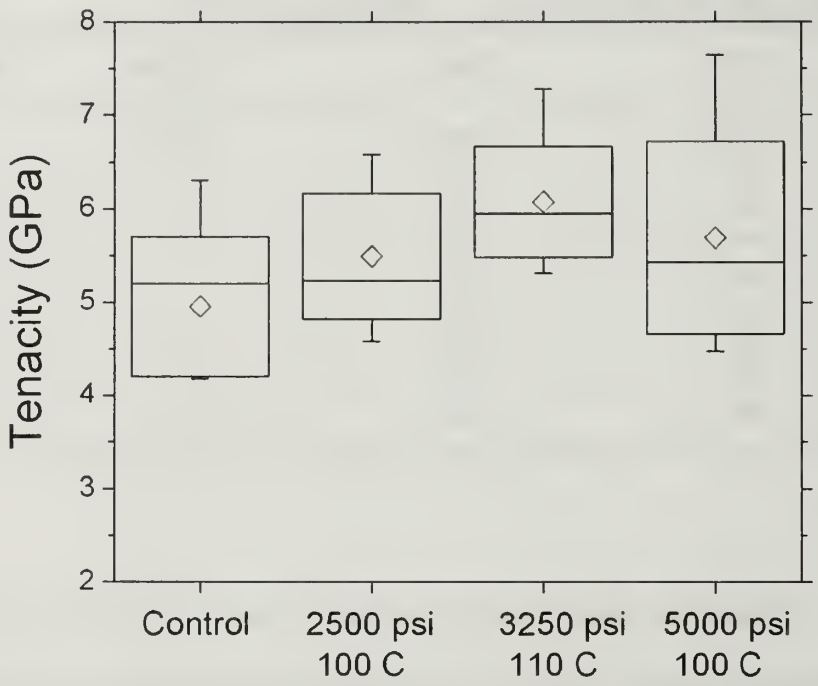

Figure 54: Tenacity of PBO AS fibers washed with scCO2 at 5 LPM flow rate and varying conditions of temperature and pressure compared to pristine control fiber. Whiskers denote minimum and maximum, box denotes median and standard deviation and the open diamond denotes the mean.

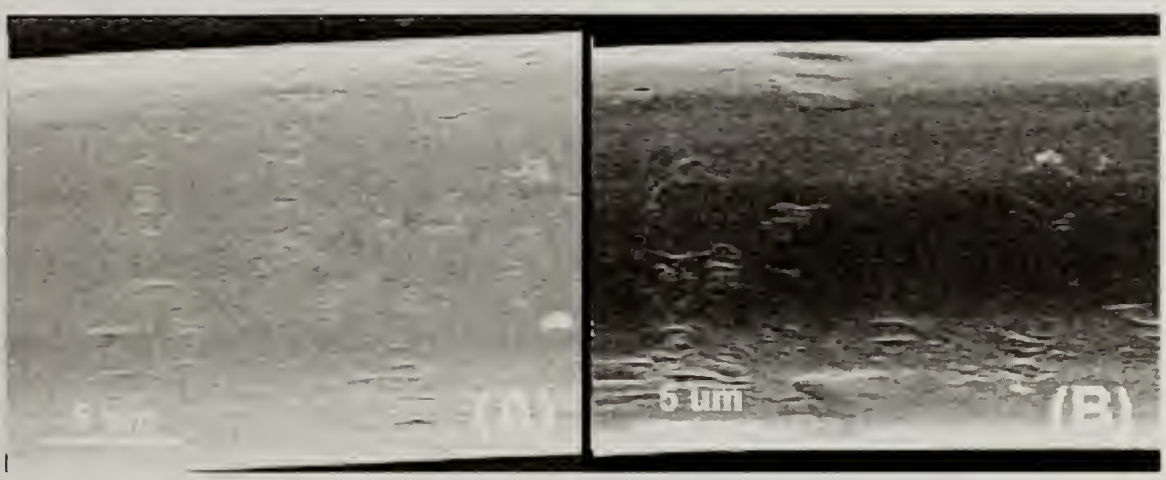

Figure 55: SEM of scCO2 washed PBO AS fiber (A) compared to control fiber (B).

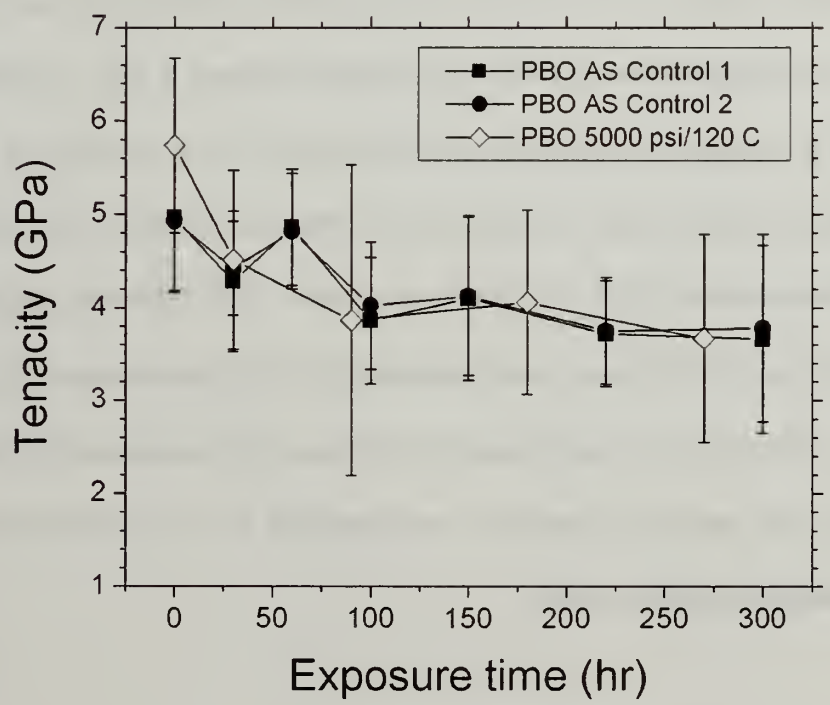

Figure 56: Tenacity of scCO2 washed PBO AS fibers exposed to UV-Vis light at 750 W/m^2 compared to pristine control fiber.

Neutralization and Extraction of Residual Phosphoric Acid

A second approach to improving the stability of PBO in aqueous conditions was to neutralize any residual phosphoric acid with a small molecule having a more favorable reaction with phosphoric acid than the polymer backbone. An $scCO_2$ environment could be used to both enhance introduction of the small molecule and extract the neutralized phosphoric acid.

Three low molecular weigh compounds shown in scheme 3 were selected to explore this hypothesis. Morpholine (MOR) and pyridine (PYR) were chosen based on their pKa values relative to the pKa values for loss of phosphoric acid hydrogens (scheme 1). Trimethylphosphate (TMP) was selected because it has a chemical structure very close to phosphoric acid and has been shown in other polymers to actually work as a molecular fortifier due to noncovalent interactions between the polar phosphate and polymer network [137]. For these experiments PBO fiber was soaked in $scCO_2$ at 100 °C/5000 psi for 30 hours then immersed in 100% concentrations of each compound at room temperature for approximately 160 hours. The mechanical properties were initially tested and additional samples were exposed to UV-visible light and subsequent mechanical properties tested.

Scheme 3: small molecules used to treat PBO AS fibers: pyridine, morpholine and trimethylphosphate.

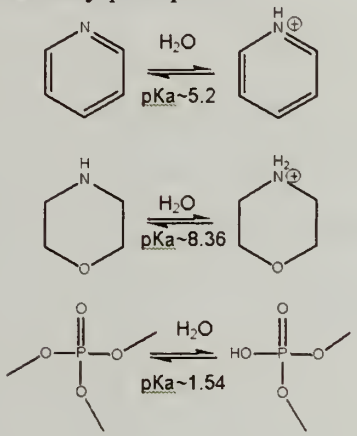

Figure 57 compares the effect these compounds have on the initial fiber tenacity and the indication is that there are no changes in tenacity relative to the control fiber. However, as shown in Figure 58, exposure to all three of these compounds negatively affects the UV-Vis stability. Both trimethylphosphate and pyridine exposed fiber showed slightly less stability than the control fiber – in fact the response of these two compounds is similar in magnitude to that for fiber exposed to concentrated phosphoric acid (Chapter 3, Figure 45). After only 30 hours the morpholine treated samples had degraded to the extent that it was not possible to test single fibers.

Information published by Toyobo [136] and work by Allen et al. on the chemically and morphologically similar poly(p-phenylenebenzobisthiazole) fibers [138] has already indicated decrease in the tenacity of PBO with exposure to strong acids and bases, however, the results of the present work are alarming in that here comparatively weak acids and bases in combination with exposure to UV-Vis light have been observed to significantly degrade fiber strength.

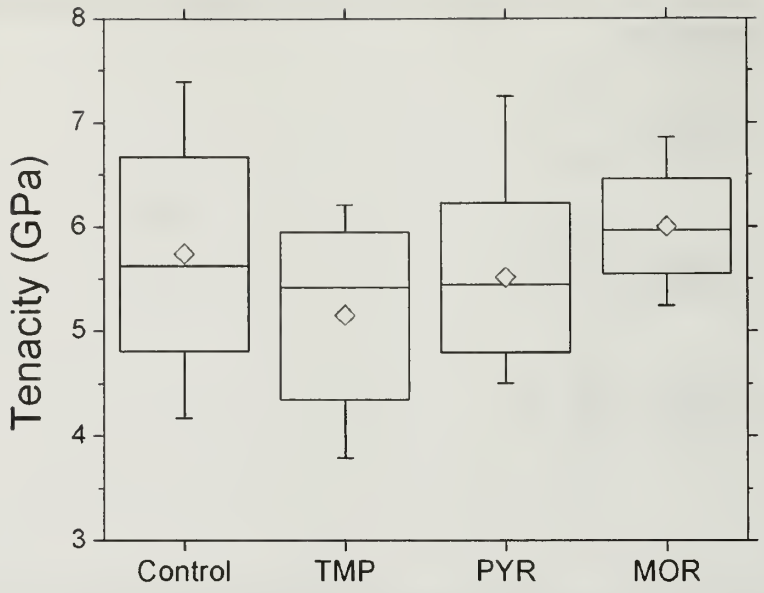

Figure 57: Comparison of initial tenacity for control PBO AS fiber and fiber treated with trimethyl phosphate (TMP), pyridine (PYR) and morpholine (MOR). Whiskers denote minimum and maximum, box denotes median and standard deviation and the open diamond denotes the mean.

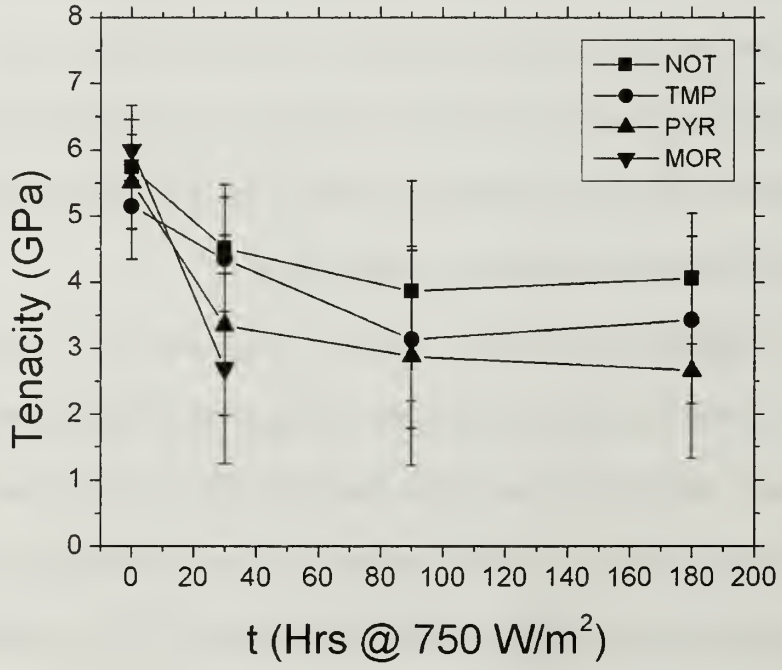

Figure 58: Tensile testing results for PBO AS fibers treated with pyridine, morpholine and trimethyl phosphate.

In further work PBO AS fibers were exposed to pyridine in an $scCO_2$ environment. The idea here was to more effectively introduce pyridine into the fibrillar bundle and where it could neutralize the residual acid and subsequently be extracted along with the $scCO_2$ upon depressurization. Figure 4.8 shows the UV-Vis stability of these fibers plotted along with that of two control samples and the pyridine exposed sample of Figure 58. The primary point of interest is that the $scCO_2$/Pyridine sample shows approximately similar response to UV-Vis light as the control groups. This is in contrast to the decrease in UV-Vis stability of the PBO fibers exposed to pyridine without $scCO_2$ of Figure 58. One explanation for the UV-Vis stability of the pyridine/ $scCO_2$ exposed fiber is that the $scCO_2$ environment is an effective extraction solvent for removing pyridine without damaging the fiber.

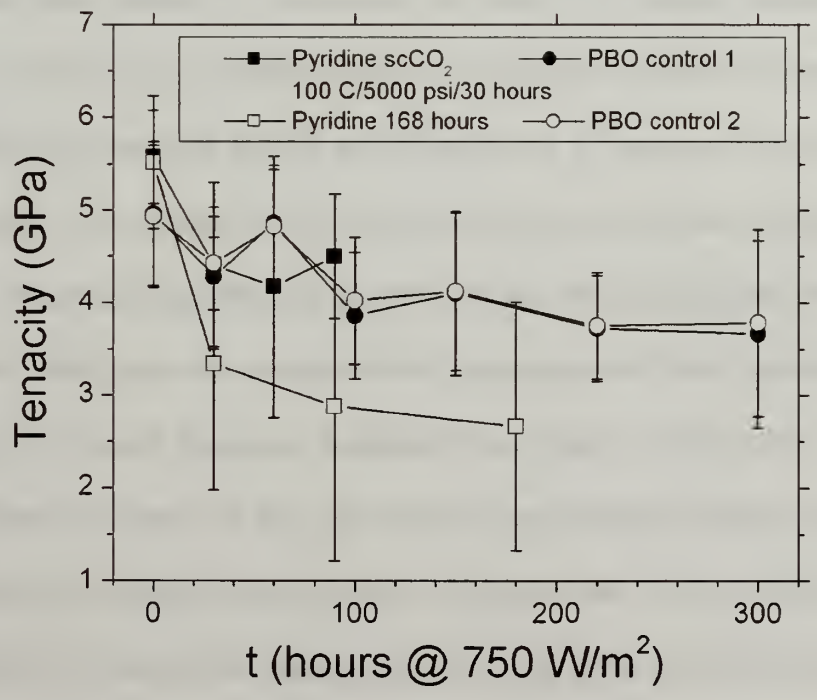

Figure 59: Tensile testing results for PBO AS fibers treated with pyridine in an scCO2 environment.

Figure 60 shows the ATR-FTIR spectra for fibers exposed to liquid water, and treated with 1 M phosphoric acid, 100% trimethyl phosphate, 100% pyridine and 100% morpholine. While the spectra for the pristine fiber and water exposed fiber are similar and indicate little or no chemical change near the fiber surface, changes are observed for fibers exposed to the phosphoric acid, trimethyl phosphate, pyridine and morpholine. In the case of phosphoric acid exposed fiber a broad peak develops between ~3200 and 3300 cm^{-1}. This peak is assigned to a secondary amine on the oxazole ring nitrogen implying some hydrolytic reaction, but because there is no accompanying carbonyl peak the oxazole ring is probably not disrupted. Exposure to trimethyl phosphate shows evolution of a narrow peak at ~1700-1800 cm^{-1} that is ascribed to a carbonyl. The pyridine exposed fiber shows development of both an oxazole ring secondary amine peak between ~3200-3300 cm^{-1} and a narrow carbonyl peak at ~1700-1800 cm^{-1}. The morpholine exposed fiber shows the appearance of a narrow peak at ~1690 cm^{-1} that is thought to be due the formation of an amide carbonyl, however there is no accompanying secondary amine peak. It is not possible to deduce the exact chemical pathway of these degradation reactions from these spectra. Taken together they suggest that hydrolytic reactions originating at the oxazole nitrogen and subsequent alteration or disruption of the oxazole ring around its quaternary carbon center are the most likely route [115].

All the above results were somewhat surprising. Since it was initially anticipated that the residual phosphoric acid played a key role in at least accelerating the degradation of the PBO, and the introduction of a base should neutralize the acid. Nonetheless, the reduction of fiber tenacity with UV-Vis exposure shows that the stability of PBO fiber in the presence of UV-visible light spectrum radiation is highly sensitive to the environment

and any condition either basic or acidic (Chapter 3 concentrated phosphoric acid exposure) can accelerate the degradation. This observation seems to support the hypothesis proposed in Chapter 3 that the PBO fiber may be intrinsically susceptible to photodegradation. A recent study by Wang et al. shows that these polymers do absorb significant amount of energy in the UV-visible spectrum [114]. It should be emphasized that absorption of energy doesn't necessarily indicate instability. However, energy is absorbed nonetheless and, if these fibers are intrinsically unstable in this spectral range, the presence of either an acid or base may synergistically increase the degree of degradation.

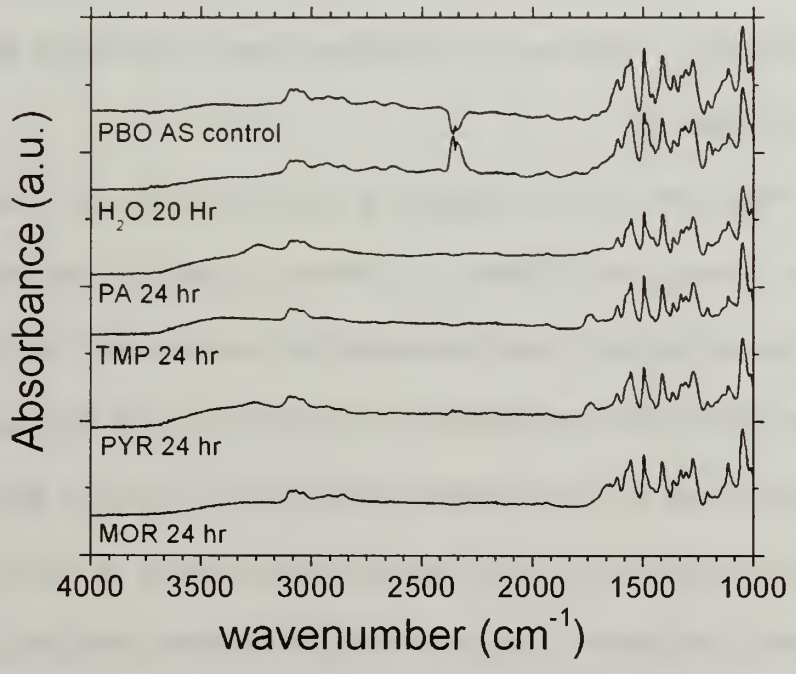

Figure 60: ATR-FTIR spectra of PBO AS fibers treated with phosphoric acid, pyridine, morpholine and trimethyl phosphate compared to spectra of pristine fibers and water exposed fibers.

UV-Vis Blockers

Both the conjugated structures in PBO chains and the π - π stacking in crystals may make PBO fibers intrinsically photo-sensitive. For polymeric products, a frequent method of improving weathering resistance or photo-stability is through the use of additives to absorb incident UV-Vis radiation. In this work UV blockers applied to the PBO AS fibers were carbon black, exfoliated graphite (EG) and glassy titanium dioxide prepared via a sol-gel method.

Both carbon black and the exfoliated graphite flakes were pulverized using an ultrasonic processor in ethanol for 24 hours. PBO fiber bundles were immersed in the sonicated solution, taken out and dried for UV-visible light exposure, and subjected to tensile testing. SEM images of PBO fibers coated with carbon black and graphite are shown in Figure 61.

Note that exfoliated graphite does not cover the fiber surface in a consistent manner. Although the thickness of exfoliated graphite is in the range of nanoscale, the aspect ratio of graphite is much larger and this prevents defect free coating of the fiber. In contrast, carbon black powder does cover the surface of the fiber fairly well. There are at least two reasons for better coating of carbon black. One is that the size of a carbon black particle is about 20 to 50 nm and their agglomeration is still in the range of a few hundreds of nanometers. The other reason is that carbon black has polar groups such as -C=O, -COOH and –OH near the particle surface. Compared to exfoliated graphite, these polar groups have stronger interactions with PBO fiber, which will result in better coating and coating strength.

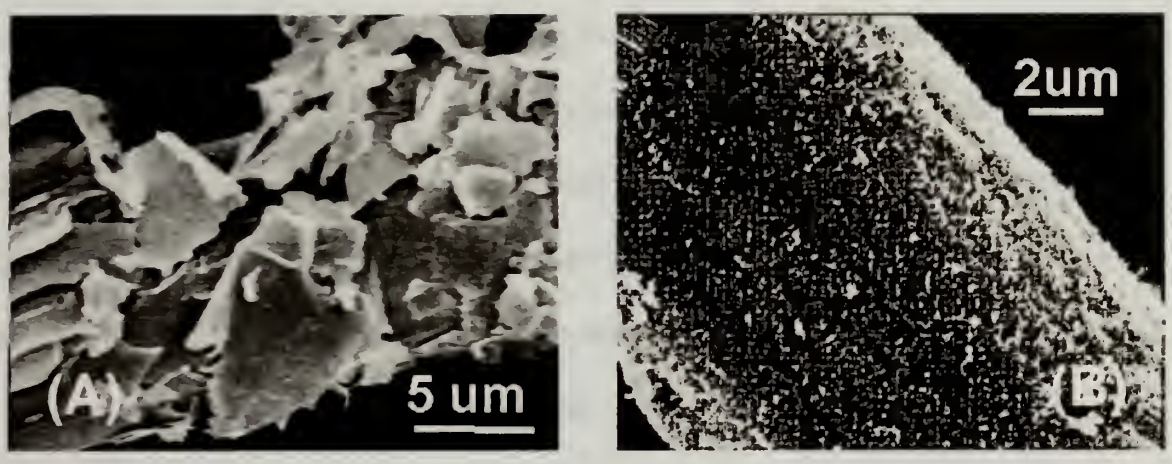

Figure 61: SEM of (A) graphite and (B) carbon black coated PBO AS fibers.

As shown in Figure 62, the load-at-break of carbon black coated fibers is very close to those of control samples at the same UV-Vis exposure time. Coating PBO fiber with carbon black does not appear to increase the light stability of PBO fibers. In contrast to carbon black, it seems that exfoliated graphite increases the rate of UV-Vis degradation of PBO fibers. In Figure 62, the load-at-break of EG coated fibers decreases more quickly compared to uncoated ones. Carbon black coating does not increase the light stability of PBO fibers. One possible reason is that the coating may be too thin to block the UV-visible light. The exact thickness of coating is not clear from SEM images.

A third UV-Vis blocking material used is a glassy coating of TiO_2 created using sol-gel chemistry. A sol-gel was made by adding titanium isopropoxide to ethanol with pH brought to ~2 using dilute hydrochloric acid [121,122,123]. Previously prepared PBO AS single fiber tensile specimens were dipped in the sol-gel and allowed to dry in vacuum at 50 °C for one hour. Figure 63 shows the UV-Vis absorbance of the sol-gel and the dry TiO_2 film. While the wet sol-gel blocks most of both the UVB and UVA spectrum, the glassy TiO_2 film is only effective in blocking the UVB wavelengths. Figure

64 shows an SEM image of the resulting glassy TiO_2 coating. The coverage appears very consistent, with thickness on the order of 100s of nanometers. However, there are some cracks and defects evident. The cracks aligned with the fiber axis are due to contraction of the glassy TiO_2 as the ethanol solvent evaporates away, while those perpendicular to the fiber axis result from the fracture of the glassy and brittle coating due to handling the fibers after evaporation. The figure 62 tensile testing results for samples exposed to UV-Vis show that the tenacity of the TiO_2 coated fibers is nearly identical to that of two uncoated control groups. Again, it is a surprise that this coating does not enhance the UV-Vis stability. This could be due to either inadequate film thickness or defects in coverage due to cracking during drying and handling. Also, given that the TiO_2 film only absorbs strongly in the UVB spectrum, UVA spectrum radiation may still be reaching the fiber surface.

These results, although unsuccessful in improving the resistance of PBO fiber to UV-Vis spectrum radiation, clarify some of the attributes needed for successful application of a UV-Vis blocking material. The blocker must efficiently either absorb or reflect incident UV-Vis radiation over the full UV spectrum. The coating must completely cover the fiber surface and be flexible enough that bending of the fibers does not result in fracture or other defect. Given the results for degradation due to physical expansion of the fibrillar bundle with exposure to water presented in chapter 3 it would be advantageous if the coating also excluded water from the fiber interior.

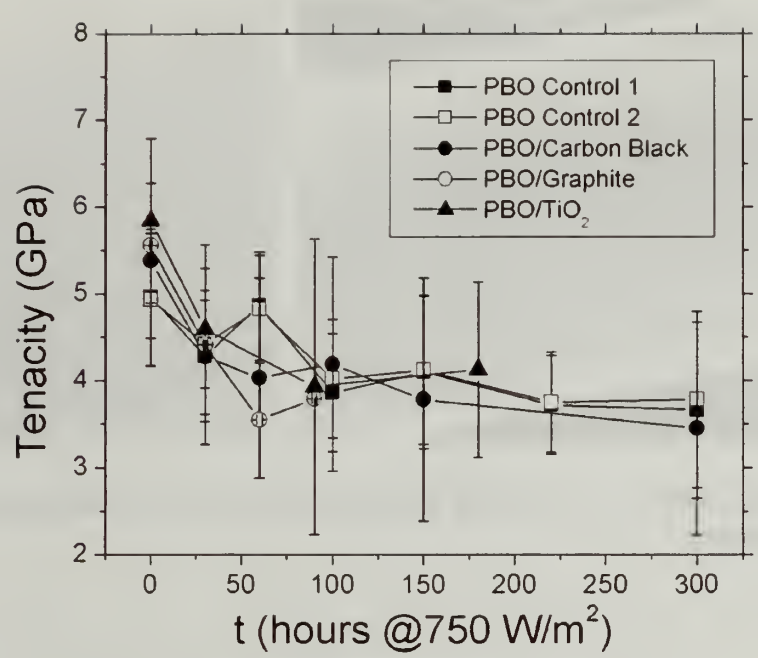

Figure 62: Tensile testing results for carbon black, graphite and TiO2 coated fibers exposed to UV-Vis light.

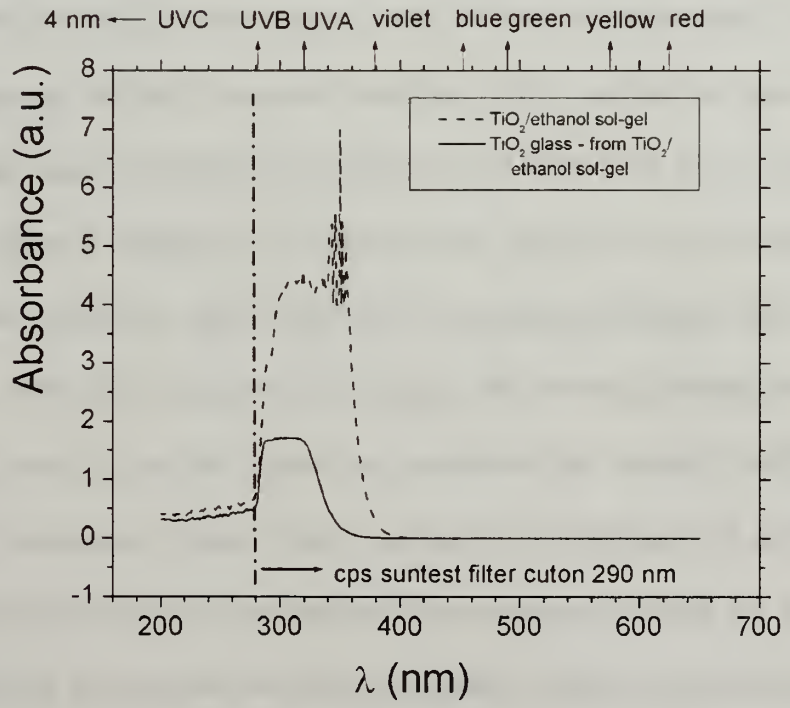

Figure 63: UV-Vis absorption of TiO_2 sol-gel and dried glassy TiO_2 film.

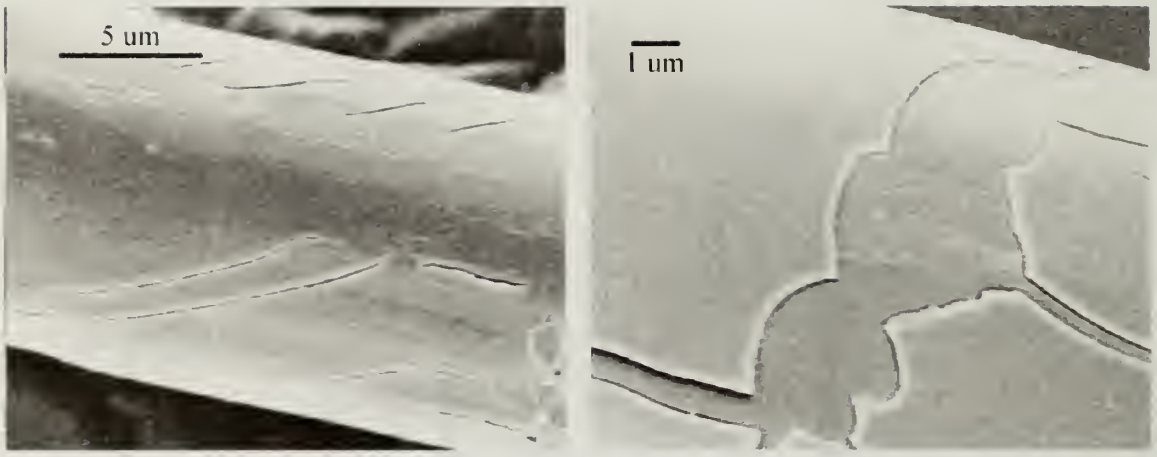

Figure 64: SEM of TiO_2 coating showing a thin film with thickness on the order of ~100's of nanometers.

Compaction of Fiber Microstructure

In Chapter 3 exposure to water was shown to result in physical separation of the fibrillar elements within the PBO fiber. In particular the size of voids between the fibrils was found to increase. SEM evidence indicated that the presence of concentrated phosphoric acid accelerates this swelling and separation perhaps due to the effects of a synergistic chemical reaction. Because the loss of strength is primarily due to loosening of the fiber morphology there may be an opportunity to improve the properties of PBO. Any post spinning process that compacts the structure of the fiber, increases the size of the fibrillar elements and/or reduces the volume fraction of voids should be a route to improving the mechanical properties. Three possible approaches are: using twist to compact the fibrillar morphology of the fiber and enhance load transfer between fibrils, using hydrostatic pressure to compact the fibrillar morphology, and using tension and the plasticizing influence of CO_2 to align crystalline domains and decrease the number of defects in the crystalline material.

The initial idea here is to increase the strength of single filament by an interlocking mechanism where the fibrils are held together by radial force and friction due to twist. Fibrils in the twisted fiber can break more than once and still support load via load transfer from fibril to adjacent fibril. There should be an optimum twist since very high degree of twist will result in a transverse compression stress on fibrils and a decrease in strength.

In the tensile results for twisted single fibers presented in figure 64, the load-at-break of PBO fibers increases very slightly for degree of twist of less than ~5 turns. After 5 turns the tenacity no longer increases and begins to show significantly increased variability.

In the previously described experiments using $scCO_2$ to extract residual phosphoric acid, fibers were placed under hydrostatic pressure using $scCO_2$ fluid. Figure 54 shows a weak trend of an increase in fiber strength for pressures of 2500 and 3250 psi at a temperature of 100°C. This result encouraged a further look at using $scCO_2$ in combination with hydrostatic stress to compact and increase the perfection of the fiber morphology. Experiments were conducted in which $scCO_2$ and nitrogen was used to apply hydrostatic pressure to the fiber with silicon oil as an intermediate fluid. Fibers were placed in a pressure vessel filled with silicon oil and hydrostatic pressure was applied using both nitrogen gas and $scCO_2$. Conditions of temperature and pressure were in both cases 5000 psi and 100°C. Figure 66 shows the results of tensile testing for these fibers. The indication is that there is no increase in fiber tenacity with such treatment, and in fact there is a drop for the fibers with $scCO_2$. Figure 67 shows SEM micrographs of the PBO AS fiber surface after pressure treatment in silicon oil. It appears that the silicon oil,

which is highly soluble in $scCO_2$, has completely wet the surface and being of low molecular weight may have swollen the fiber.

Tension, usually combined with heat, is widely used in fiber industry to increase the orientation of both amorphous and crystalline region of fibers. There are two competitive processes during this: fibers tend to become oriented upon tension and lose orientation on heating. If the magnitude of tension is adequate to overcome the influence toward disorder then the crystalline material is forced to align and the heat can have the effect of increasing the perfection of the crystalline material. This is precisely the approach used to manufacture high modulus PBO (PBO HM) fibers from PBO AS fiber. In this work $scCO_2$ is used with the idea that it may partially plasticize the fiber material and enable a decrease in the defects present.

The effect of tension on fiber properties was explored by placing fibers under tension of ~40 cN or approximately ~80% of the fiber breaking strength. Experiments were conducted in both air at standard pressure and temperature and in sub critical CO_2 at 20 °C and 5000 psi for a 24 hour duration. The results of tensile testing on fibers treated in this way are shown in figure 68. The fiber placed under tension in air shows the same tenacity as control fibers not held under tension. The fiber held under tension in the $scCO_2$ environment shows a slight increase in tenacity but given the large degree of variability this is not a significant effect.

All three of these approaches to compact the fiber morphology and decrease defects using mechanical means of twist, hydrostatic pressure and tension combined with $scCO_2$ conditions resulted in no significant increase in fiber tenacity. One possible explanation for this may be that even if a compacting force is applied to the fiber, once

that force is removed the comparatively weak van der Waals inter-fibril and dipole inter-chain forces are insufficient to maintain the compacted morphology. The observation of little or no increase in properties with application of a compacting force in the presence of $scCO_2$ suggests that $scCO_2$ has little effect on the number of defects present in PBO fibers.

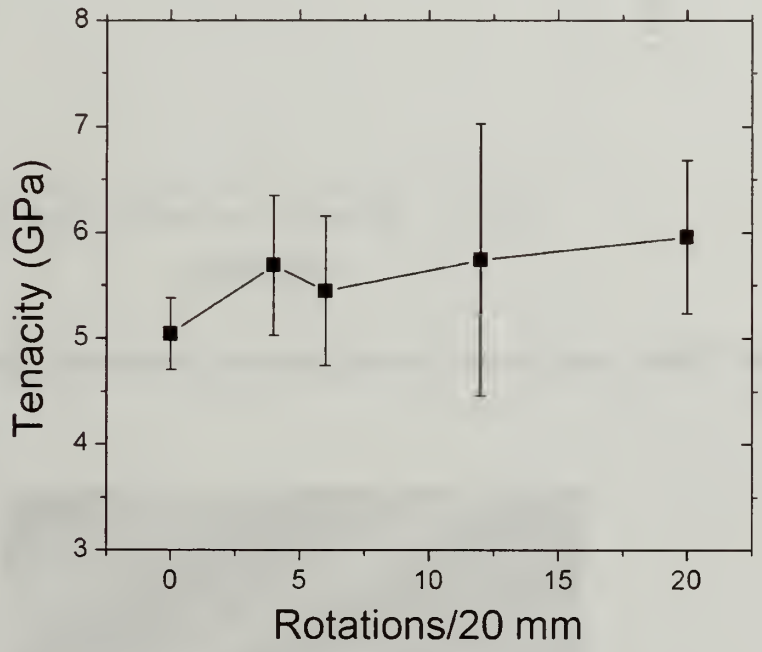

Figure 65: Tensile testing results showing effect of twist on fiber tenacity. Error bars indicate 1 standard deviation on the mean.

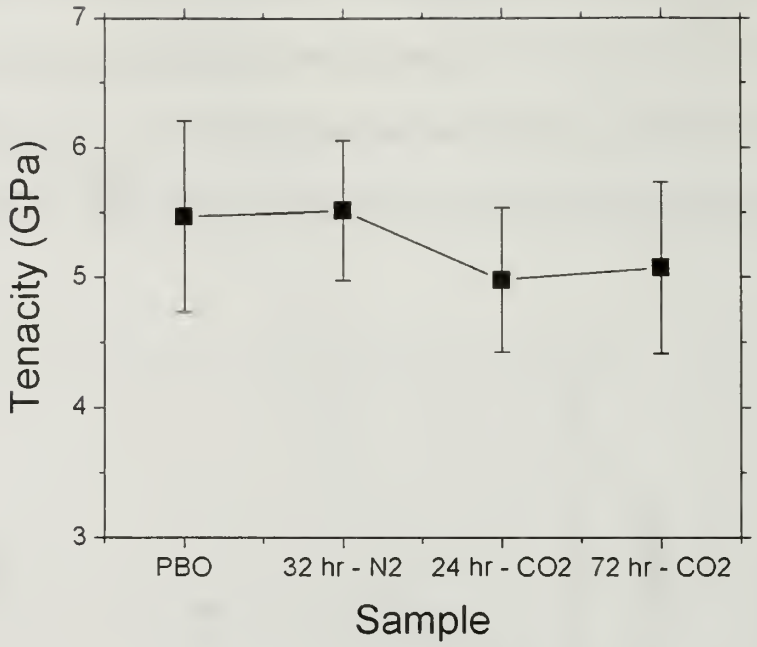

Figure 66: Tensile testing results showing effect of hydrostatic pressure on fiber tenacity

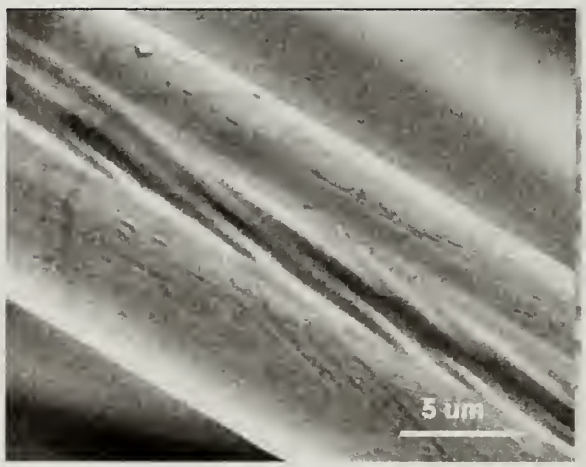

Figure 67: SEM micrographs of PBO AS fiber surfaces after compaction in $scCO_2$ and silicon oil.

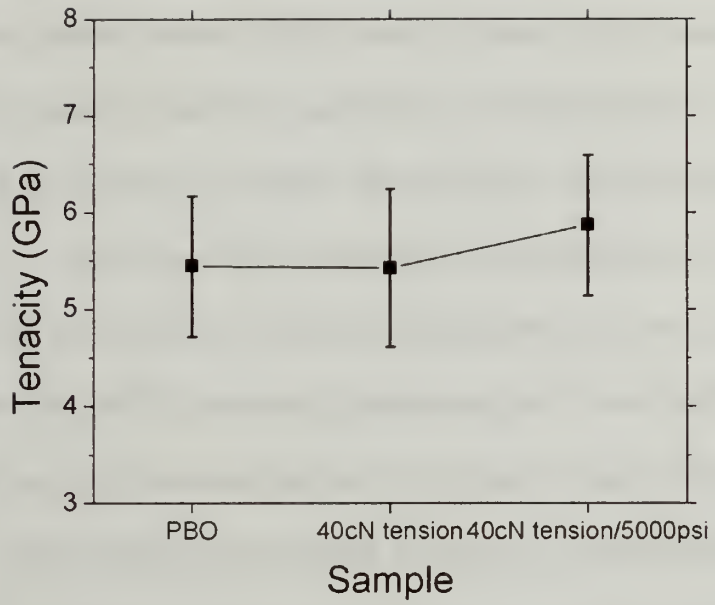

Figure 68: Tensile testing results showing effect comparing the tenacity of untreated PBO AS fiber with PBO AS fiber held at 40cN tension and PBO AS fiber held at 40 cN tension and soaked in a sub-critical CO_2 environment under 5000 psi hydrostatic pressure. Error bars indicate 1 standard deviation on the mean.

Super-critical Fluid Approach to PBO AS/Polysiloxane Composites

The results of Chapter 3 indicate that the degradation of PBO AS fiber properties by moisture is primarily due to non-recoverable loosening of the fiber structure and introduction of larger number and size defects. In the previous section increases in fiber tenacity are observed due to compaction of the fiber microstructure using twist and hydrostatic pressure applied by $scCO_2$. These results suggest that if the fibrillar microstructure could be compacted and a secondary inter-fibril force added to maintain the compaction, both the initial fiber tenacity and resistance to degradation by moisture might be improved.

Composites of PBO AS fiber and polysiloxanes crosslinked in a hydrosilation reaction have been prepared in super-critical carbon dioxide environment according to Scheme 4. This approach takes advantage of the high solubility of siloxanes in $scCO_2$ by introducing relatively small molecular weight vinyl substituted polysiloxane prepolymer and 1,2,5,7-Tetramethylcyclotetrasiloxane ($D4^H$) crosslinker to the fiber, swelling the fiber with them and subsequently initiating crosslinking by introduction of a platinum catalyst. The intent is that the resulting elastomeric PDMS will infiltrate the fiber, adhere to the fibrillar elements and provide a robust secondary force to prevent expansion of the fiber microstructure by exposure to liquid and vapor phase water.

Two polysiloxane resins systems were investigated: the first is a low molecular weight vinyl substituted polysiloxane prepared in a polycondensation reaction (PVMS) and the second is a commercially available PDMS resin system with higher molecular weight (Sylgard 184).

Scheme 4: Preparation of PBO AS/crosslinked PDMS Composites in $scCO_2$ environment

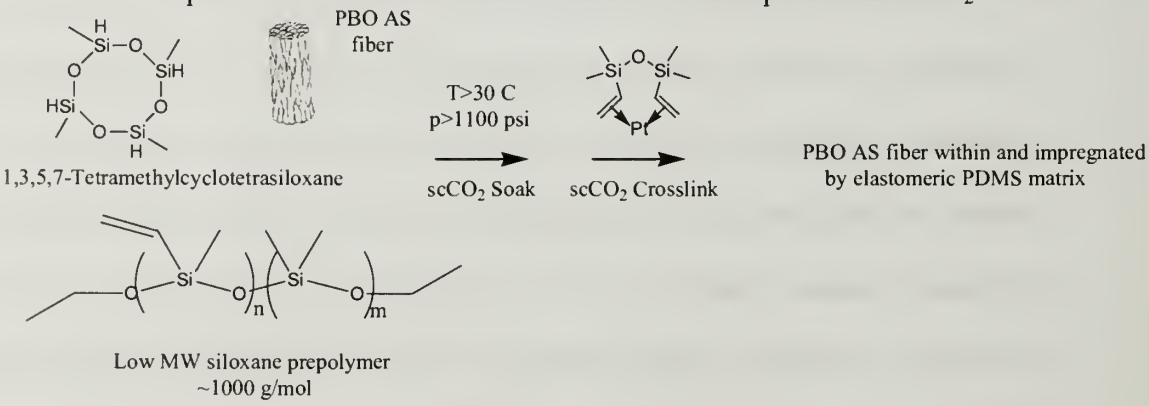

Preparation of Vinyl Substituted PVMS prepolymer

The PVMS prepolymer was prepared according to scheme 1, a polycondensation of dichlorodimethylsilane with dichloromethylvinylsilane. After the initial reaction the

majority of the aqueous phase was removed, zinc acetate added and heat applied to decrease the cyclic content and increase molecular weight. The prepolymer was then washed in absolute ethanol to end cap any active chain ends and remove the remaining hydrochloric acid polycondensation product.

Figure 69 shows the NMR spectra of the prepolymer material. The group of peaks at ~6 ppm shift are associated with the vinyl protons while the large peak at ~0 ppm is associated with methyl protons. The peaks at ~3.7 ppm, ~1.5 ppm and ~1.2 ppm are attributed to acetone, water and ethanol impurities respectively. Integration and comparison of the vinyl and methyl proton peaks indicates a ratio of methylvinyl to dimethyl repeats of approximately 1:10.

MALDI-TOF was used to characterize the molecular weight of the PVMS product. The distribution is shown in figure 70. The mass spectrum shows a series of four distributions of ions between *m/z* 500 to *m/z* 2000 all of which have a *m/z* spacing of approximately 74 corresponding to the mass of a polydimethylsiloxane repeat unit. The four distinct distributions indicate that the PVMS prepolymer is probably a mixture of cyclic and linear species. The number average molecular weight is calculated to be 1003 g/mol yeilding an average chain length of approximately 13.5 units containing on average 1.4 vinyl substituted repeat units each. Density of the liquid was estimated to be 1.179 g/ml.

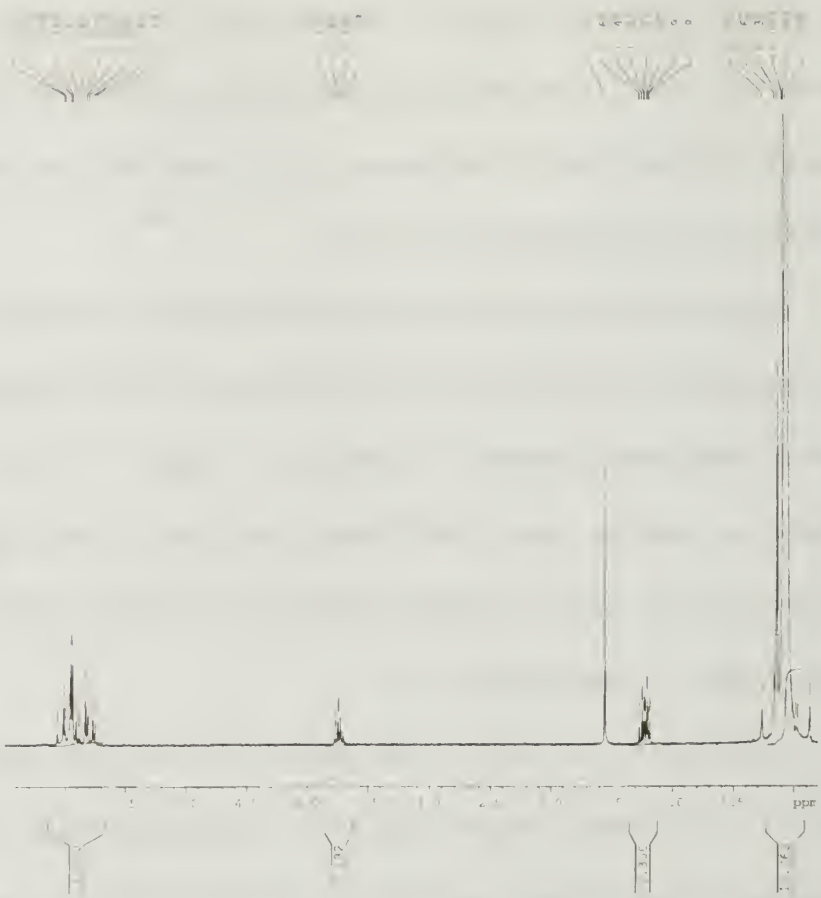

Figure 69: NMR spectra of vinyl substituted PDMS prepolymer. Peaks near 6 ppm shift are associated with vinyl protons, peaks near 0 ppm are associated with methyl protons. Integration indicates a 13.5:1 ratio of dimethyl siloxane repeats to methylvinyl siloxane repeats. Peak near 1.5 ppm is water.

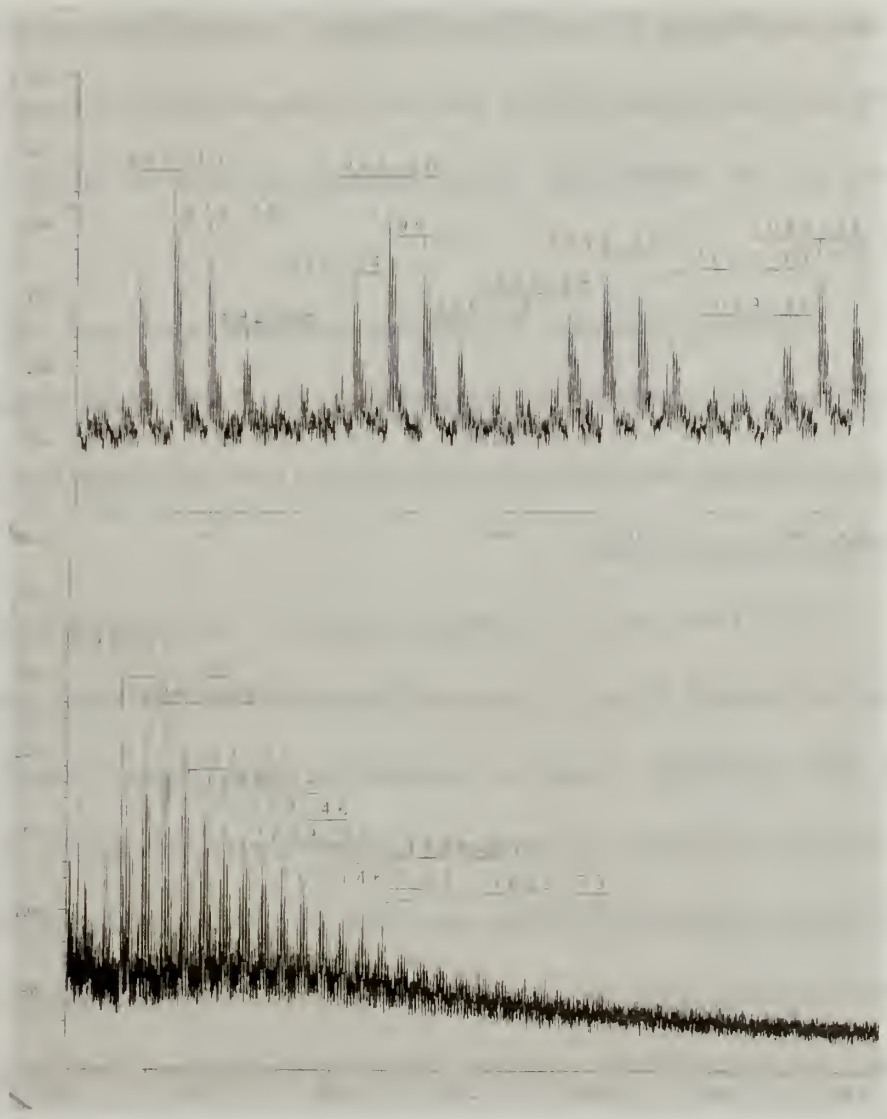

Figure 70: MALDI-TOF molecular weight distribution for vinyl substituted PDMS prepolymer. M_n is 1003 g/mol.

Polymerization of PBO AS/Crosslinked PDMS composites in $scCO_2$

On the basis of the PVMS prepolymer NMR and MALDI-TOF results the PVMS prepolymer was combined with an appropriate quantity of the $D4^H$ crosslinker such that there was an approximately 1:1 ratio of vinyl groups to $D4^H$ hydrides. The PBO AS fiber and PVMS prepolymer/$D4^H$ mixture was soaked in $scCO_2$ at 50 °C under pressures of 1500 psi, 2500 psi and 3500 psi for 4 hours. The pressure vessels were depressurized to

initiate crosslinking by the addition of Karstedt's catalyst then re-pressurized to T=50 °C, 1500 psi, 2500 psi and 3500 psi. The cross-linking reaction was complete in less than two hours and the vessels were slowly depressurized over 0.5 hours using the ER-3000 controller.

Identical procedures and process conditions were used with the Sylgard 184 PDMS resin and catalysis was accomplished using 5 wt% of the Sylgard 184 crosslinker. The crosslinking reaction in this case took less than 30 minutes and yielded a relatively stiffer elastomeric product.

SAXD was used to determine what effect cross-linked polysiloxane had on the fiber morphology. Figure 71 compares the control fiber diffraction patterns with those of the PBO AS/PVMS composite prepared at each pressure condition. As described previously in Chapter 3 the equatorial streak is known to be due to scattering by needle-like voids oriented along the fiber axis [124]. The composite fiber diffractions contain the same equatorial streak but also show an amorphous halo that might be associated with either particles of PDMS or cavities created by foaming upon the release of CO_2 pressure. The Guinier correlation lengths of the equatorial streak $(D_{Equatorial})$ and diffuse halo $(D_{Meridonal})$ are tabulated in Table 9 assuming the equatorial streak is scattering from cylindrical voids and the diffuse halo to spherical particles. The decrease in $D_{Equatorial}$ with increasing polymerization pressure is associated with a decrease in the radius of gyration of the longitudinal voids present in the PBO AS fiber. There is also a weak trend of decreasing $D_{Meridonal}$ with process pressure. Similar results SAXD results for Sylgard 184 are shown in figure 72 and Table 10.

These results are consistent with infiltration of the fiber by crosslinked polysiloxane; first the fiber was compressed by the high pressure conditions of polymerization, secondly upon crosslinking the polysiloxane will decrease in volume. The decreasing correlation lengths infer that the polysiloxane is preventing expansion of the fiber once the process pressure is released.

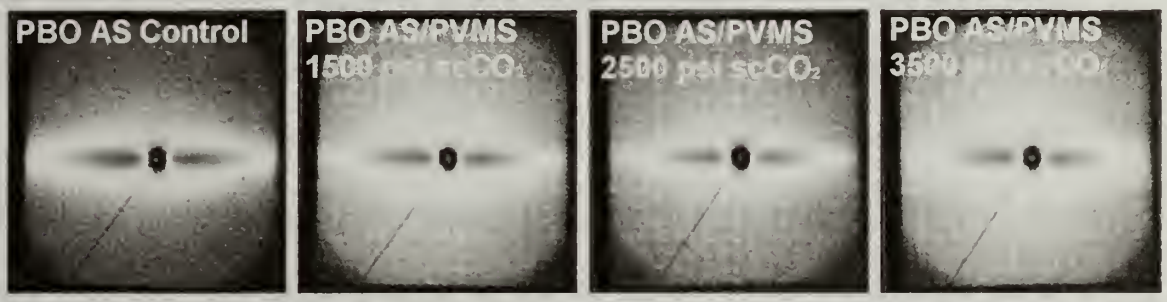

Figure 71: SAXD diffraction pattern for PBO AS control fibers compared to PBO AS/crosslinked PVMS composites fabricated in $scCO_2$.

Table 9: Change in equatorial and meridonal Guinier correlation length with increasing $scCO_2$ fluid pressure for PBO AS/vinyl substituted prepolymer PDMS composites fabricated in $scCO_2$

	$D_{Equatorial}$ (nm)	$D_{Meridonal}$ (nm)
PBO AS control fiber	3.60	1.16
PBO AS/Vinyl sub'd PDMS ***$ScCO_2$: 1500 psi/50 C***	3.23	1.07
PBO AS/Vinyl sub'd PDMS ***$ScCO_2$: 2500 psi/50 C***	3.15	1.01
PBO AS/Vinyl sub'd PDMS ***$ScCO_2$: 3500 psi/50 C***	3.17	1.03

SEM micrographs PBO AS control fibers are shown in Figures 73 and 74. The fibbrillar structure of the fiber can be clearly discerned by the striations on the fiber surface and by the fibrillation evident near kink bands. Figure 75 shows a fiber surface and kink band for a fiber scCO2 fluid soaked in crosslinked PVMS. The polysiloxane has wetted the surface well though there still appears to be splitting and fibrillation of the fiber near kink bands. Figure 76 shows a kink band on a fiber scCO2 fluid soaked in crosslinked Sylgard 184. Again the surface appears to have been wetted by the siloxane fluid. Fibrillation near the kink band does not appear to have been inhibited.

Although there is no direct visual evidence of siloxane impregnation of the fiber in the SEM results the Siloxaanes do wet the surfaces of the fiber very well. The length scale of the voids between fibrillar elements is less than 10 nm so would not expect to see changes using the SEM technique. The SAXD diffraction data are a strong indication that both the polysiloxane prepolymers used do infiltrate the fiber and add secondary inter-fibril forces that tend to maintain compaction imposed during crosslinking.

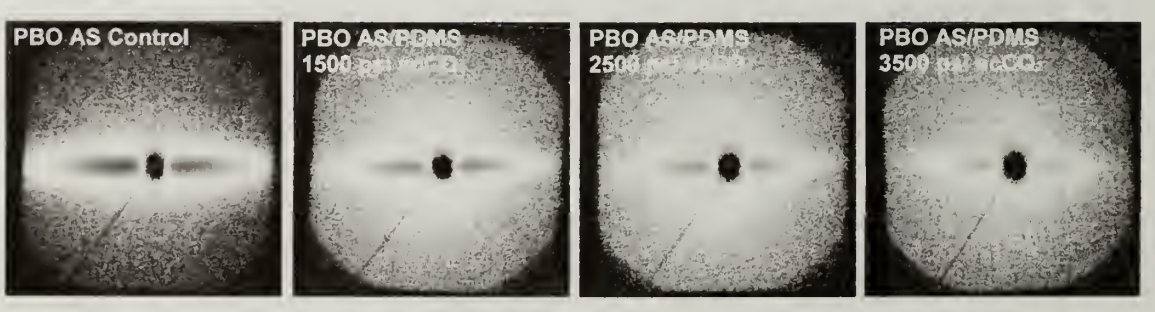

Figure 72: SAXD diffraction pattern for PBO AS control fibers compared to PBO AS/Sylgard 184 PDMS composites fabricated in $scCO_2$

Table 10: Change in equatorial and meridonal Guinier correlation length with increasing $scCO_2$ fluid pressure for PBO AS/Sylgard 184 PDMS Composites fabricated in $scCO_2$.

	$D_{Equatorial}$ (nm)	$D_{Meridonal}$ (nm)
PBO AS control fiber	3.60	1.16
PBO AS/Sylgard 184 PDMS $ScCO_2$: 1500 psi/50 C	3.16	1.13
PBO AS/Sylgard 184 PDMS $ScCO_2$: 2500 psi/50 C	3.03	1.11
PBO AS/Sylgard 184 PDMS $ScCO_2$: 3500 psi/50 C	2.93	1.10

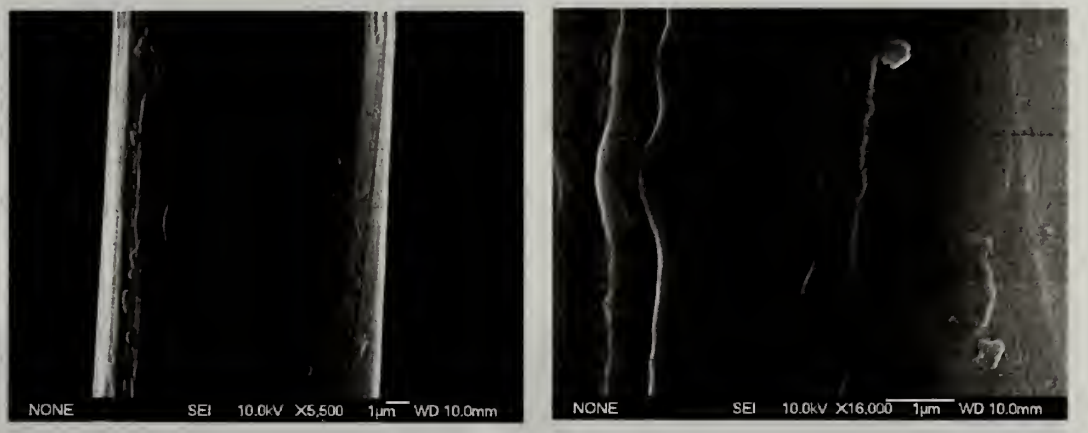

Figure 73: SEM micrographs of PBO AS control fiber surfaces

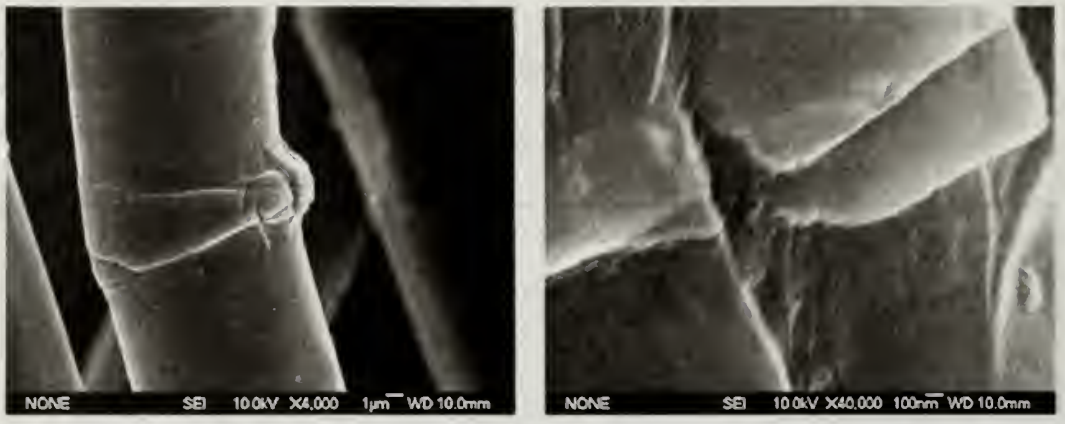

Figure 74: SEM micrograph of PBO AS control fiber kink bands

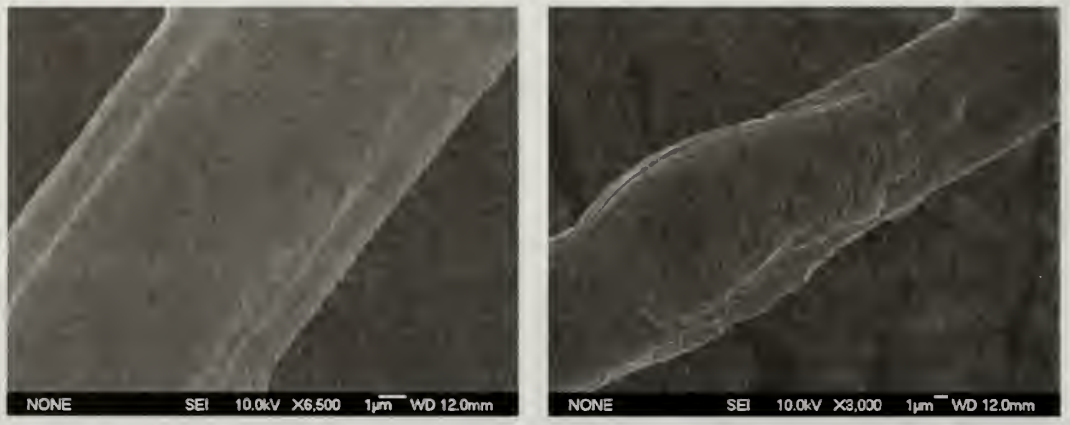

Figure 75: SEM micrograph of PBO AS fiber surfaces after soaking and crosslinking of PVMS monomer in $scCO_2$ environment. P=1500 psi, T=50 C.

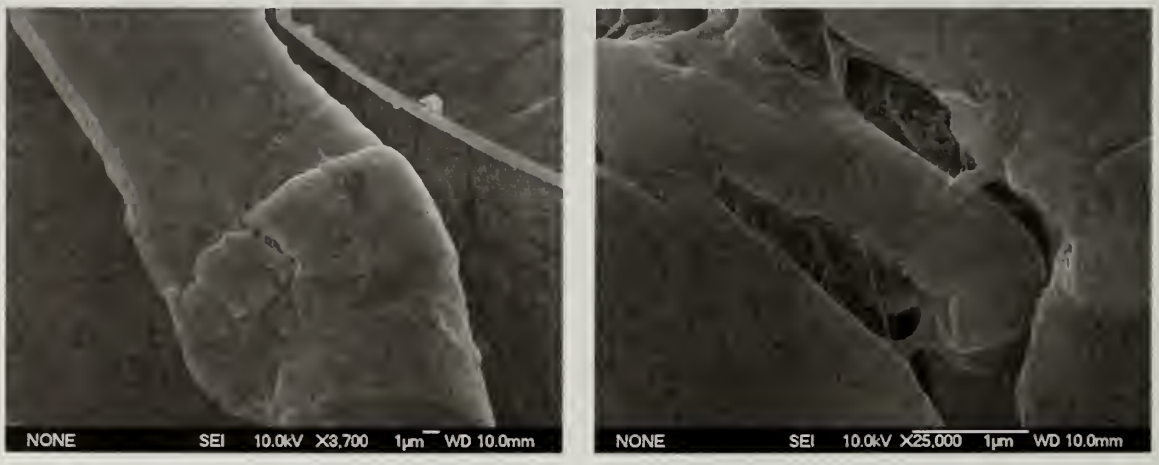

Figure 76: SEM images of PBO AS fiber kink band after soaking and crosslinking of Sylgard 184 PDMS in $scCO_2$ environment. P=1500 psi, T=50 C.

Conclusions

In light of the potential of residual phosphoric acid to either react with the oxazole ring of the PBO mer and/or attract water into the fiber super critical CO_2 extraction was used as a means of removal. Elemental analysis shows that the weight % of phosphorus present in the PBO fibers was reduced from 0.4% for neat PBO AS fiber to 0.25% for $scCO_2$ washed fiber. Mechanical testing showed that the $scCO_2$ extraction process did not degrade the fiber mechanical properties and in fact showed a weak trend to increase fiber tenacity. The high pressure and relatively high temperatures used during the $scCO_2$ extraction process may have the effect of compacting the fiber and decreasing the number and size of defects.

A second approach to the problem of residual phosphoric acid was to introduce a small molecule with a pKa value chosen such that it might complex with residual phosphoric acid and then be removed using $scCO_2$ extraction. Fibers exposed to a series of weakly basic small molecules: trimethyl phosphate, pyridine and morpholine showed no initial reduction in strength, however subsequent exposure to UV-Vis spectrum light showed these compounds to have a significant detrimental effect on UV-Vis stability of PBO fibers. ATR-FTIR spectroscopy on the treated fibers prior to UV-Vis indicated that exposure to these small molecules in aqueous conditions resulted in chemical degradation at the fiber surface.

UV-Vis stabilization of PBO fibers was attempted using UV blocking or absorbing materials to protect the fiber surface. Fibers were coated with both carbon black powder and exfoliated graphite flakes. Mechanical testing of coated fibers exposed to UV-Vis radiation and observation of the coated fiber surface by SEM shows that UV-

Vis stability was not enhanced due to imperfect coverage of the fiber surface. A second attempt at UV-Vis stabilization was made using a glassy titanium dioxide coating made by dip coating fibers in a sol-gel precursor solution. SEM revealed that thin coatings of glassy titanium dioxide with thickness on the order of 100 nm were achieved. The material does absorb strongly in the UVB region but mechanical testing of TiO_2 coated fibers exposed to UV-Vis radiation showed no improvement in UV-Vis stability. The failure of this coating material is due shrinkage and subsequent breaks in coverage occurring as the solvent was driven out of the sol-gel to form the glassy TiO_2 coating. In addition the glassy TiO_2 material lacks enough compliance to accommodate bending of the fibers leading to fracture of the coating when the fiber is handled.

The finding that degradation by moisture exposure is primarily due to physical separation of the fibrillar elements (Chapter 3) suggests that any process resulting in compaction of the fibrillar bundle may improve the fiber properties. Several approaches were undertaken. Twist was applied to the fibers to apply the compacting force. Single fiber tensile testing showed moderate increase in tensile strength. Fibers were exposed to hydrostatic pressure in nitrogen and CO_2 at room temperature. No increases in strength were observed. Fibers were placed in tension to 60% of fiber breaking load and exposed to hydrostatic pressure in $scCO_2$. Again a weak trend toward increase in fiber properties was observed.

Composites of PBO AS fiber and polysiloxanes crosslinked in a hydrosilation reaction have been prepared in super-critical carbon dioxide environment. This approach takes advantage of the high solubility of siloxanes in $scCO_2$ to swell the fiber with low molecular weight vinyl substituted polysiloxane resin and crosslinker. Crosslinking by

hydrosilation was initiated by introduction of a platinum catalyst. The intent is that the elastomeric PDMS phases will adhere to the fibrillar elements and provide a secondary inter-fibrillar force able to prevent expansion of the fiber by moisture.

Two siloxane prepolymer systems were evaluated. The first was a vinyl substituted PDMS prepared from dichlorodimethylsilane and dichloromethylvinylsilane in a polycondensation reaction to form a mixture of linear and cyclic siloxane species with a ratio of 10:1 dimethylsiloxane to vinylmethylsiloxane repeats and number average molecular weight of 1000 g/mol. The second was Sylgard 184 a commercially produced PDMS resin that was also crosslinked in a hydrosilation reaction.

SAXD results for both PBO AS fiber/Crosslinked PDMS composite systems indicate a reduction in the radius of gyration of the longitudinal voids present in the PBO AS fiber. The reduction in void size is consistent with infiltration of the fiber by the PDMS materials in two ways; during crosslinking the fiber is compacted by the super-critical fluid pressure and upon crosslinking the PDMS undergoes a reduction in volume. The observation of reduced void size after crosslinking and depressurization implies that the crosslinked PDMS has introduced a secondary inter-fibril force capable of maintaining fiber compaction. In addition SAXD of the composite systems displays diffuse scattering that may be due to the formation of PDMS particles or foaming of the PDMS upon release of the super-critical fluid pressure.

Comparison of SEM micrographs of PBO AS control fibers and PBO AS/Crosslinked PDMS indicate the polysiloxanes do wet the fiber surface. Unsurprisingly, as the length scale of the void spaces anticipated to be accessible under

super-critical carbon dioxide is less than 10 nm, there is no direct visual evidence in the SEM results of swelling of the PBO AS fiber by crosslinked siloxane.

CHAPTER 5

FRACTURE IN CONSTRAINED GEOMETRIES

Introduction

The effect of constraint on the fracture behavior of a bi-material interface is relevant to the design of structural adhesives and bond geometries, composite materials and the fabrication of robust microelectronics devices and packaging in which thin laminates with alternating layers of glassy inorganic oxides, ductile metals and polymers are common. A great deal of work has been done within the context of structural adhesives looking at the effects of bond-line thickness on mode I fracture for cracks propagating within the adhesive layer [139-143] but little work has been done to directly examine the effects of inter-layer thickness and interfacial adhesion on cracks propagating at the bi-material interface [144]. In this chapter an experimental technique to simultaneously measure the fracture energy of the bi-material interface and image the stress distribution around the crack is proposed, evaluated relative to an alternative method and applied to a model epoxy-metallic adherend system in which the level of constraint around the process zone and level of adhesion between the two phases can be altered.

As a crack propagates through a bulk polymer material energy is consumed both by the creation of new surface behind the crack tip and plastic deformation and small scale yielding in the region ahead of the crack tip. Equation 1 is often used to describe the combined effect of surface energy and viscoelastic dissipative mechanisms on the energy required to drive fracture processes [145]. G is the total energy required to propagate a

crack, G_o is a threshold energy similar in magnitude to the surface energy of the newly created surfaces and $\Psi(R,T)$ is a function describing various viscoelastic energy dissipation mechanisms during crack propagation. Typically $\Psi(R,T)$ is orders of magnitude larger than G_o . However, the magnitude of the G_o quantity is the primary factor controlling the activation of viscoelastic dissipations represented by $\Psi(R,T)$. Small magnitudes of G_o will not transfer enough energy to the bulk material to activate these mechanisms but once a critical magnitude has been reached, the overall energy required to propagate a crack may increase by orders of magnitude.

Eq. 1) $$G = G_o\{1 + \Psi(R,T)\}$$

The deformed regions ahead of and behind the crack tip are collectively the process zone: as shown in Figure 77 the active zone is the region ahead of the crack tip and the passive zone is the region on either side of the new surface area created behind the crack tip. Energy consumed in the process zone is the origin of the toughness of the material and the majority of this is absorbed in the active zone ahead of the crack tip. The magnitude of the critical energy release rate (G_c) and the shape of the process zone is dependent on the mechanical response of the bulk material and the mode of fracture [145,146,147].

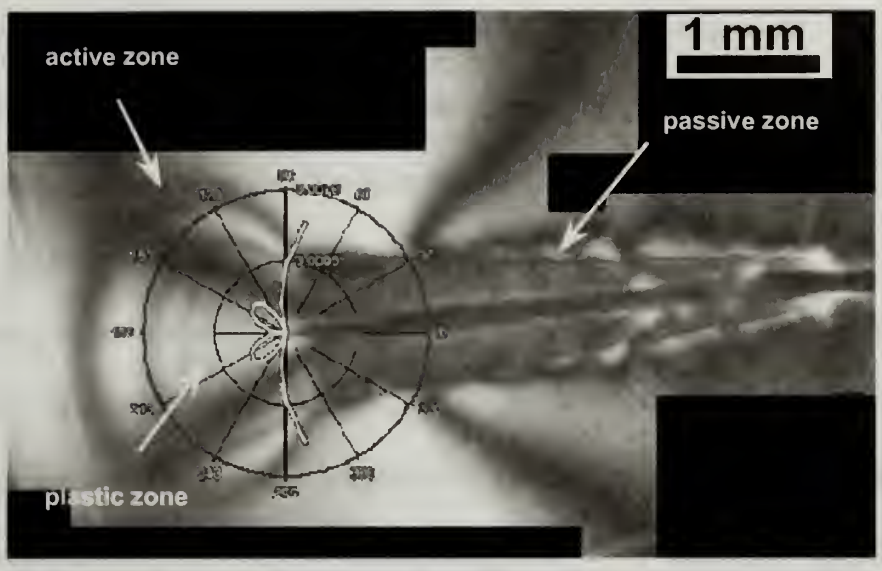

Figure 77: Photoelastic image showing the process zone of a crack propagating through a bulk thermoplastic [148].

In this work the questions of interest are: how does the critical energy release rate and shape of the process zone change with constraint imposed by the system boundaries including geometric constraint by a second phase orders of magnitude less compliant than the interlayer and changes in the ability of the interface to transfer load from one phase to the other. The particular geometry of interest, shown in figure 78 is the propagation of a crack along a bi-material interface as opposed to a fracture within the bulk. In this case there are two types of constraint: 1) the upper adherend may limit movement of polymer interlayer material points near the interface and distort the shape of the active zone radius 2) the adhesion between the polymer and adherend ahead of the crack tip constrains movement of material points in the active zone at the lower interfacial surface. Both types of constraint will result in additional stress concentrations near the crack tip. In addition residual stresses due to differences in the coefficients of thermal expansion for each phase may influence the overall stress state at the bi-material interface.

The experimental approach used is a modification of the Boeing wedge test [149] called in this work an Elastic Wedge Opened Double Cantilever Beam specimen (EWODCB). The EWODCB specimen is coupled with a model system comprised of an epoxy interlayer with metallic adherends. The sample dimensions, epoxy interlayer chemistry and cure schedule were selected such that the size of the plastic zone relative to the interlayer thickness and ability of the epoxy-metal interface to transfer load could be altered. Photoelastic techniques were applied to image the process zone surrounding the propagating crack. From these photoelastic images both the crack length, needed in the determination of G_c, the critical energy release rate for fracture, and changes in the shape of the process zone were observed.

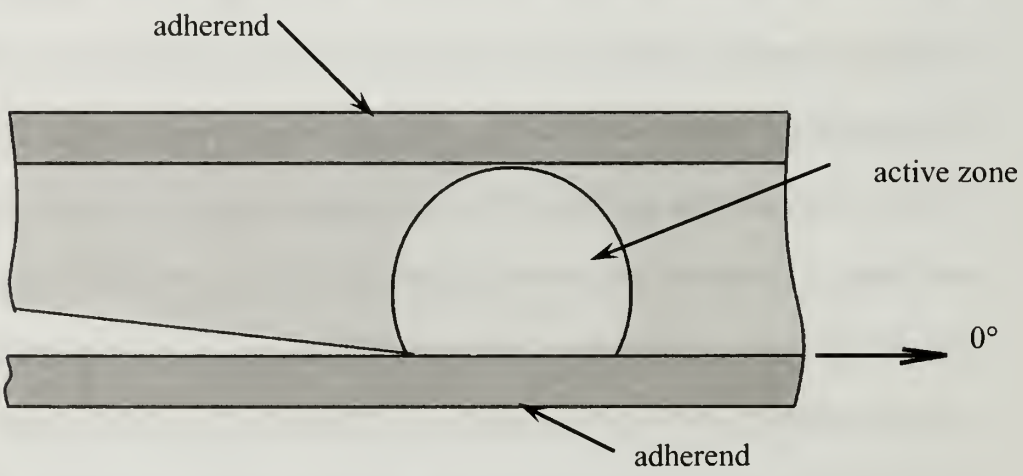

Figure 78: Schematic of fracture process zone at a bi-material interface.

Background

Previous works by Bascomb [140] and Kinloch [141] for pure Mode I fracture show that for a crack propagating through a rubber toughened epoxy interlayer, the value of G_c is similar to the bulk material if the adhesive thickness is much greater than the plastic zone radius, reaches a local maximum when adhesive thickness is twice the plastic zone radius and drops significantly when adhesive thickness is much smaller than the plastic zone radius. Figure 79 shows Kinloch's results [140]. A qualitative explanation is proposed in which the volume of the plastic zone ahead of the crack tip is correlated to the energy release rate as follows [140,150]: If $t>>2r_p$ the volume and shape of the plastic zone is similar to that in the bulk yielding critical energy release rate similar to the bulk. As t approaches r_p the volume of the plastic zone increases due to the constraint of movement at the adherend-polymer interfaces. The plastic zone volume reaches a maximum along with the energy release rate at $t\approx 2r_p$. As $t<r_p$ the adherends restrict the volume of material available for plastic deformation and the energy release rate is reduced. This concept is illustrated schematically in Figure 80 [150,151].

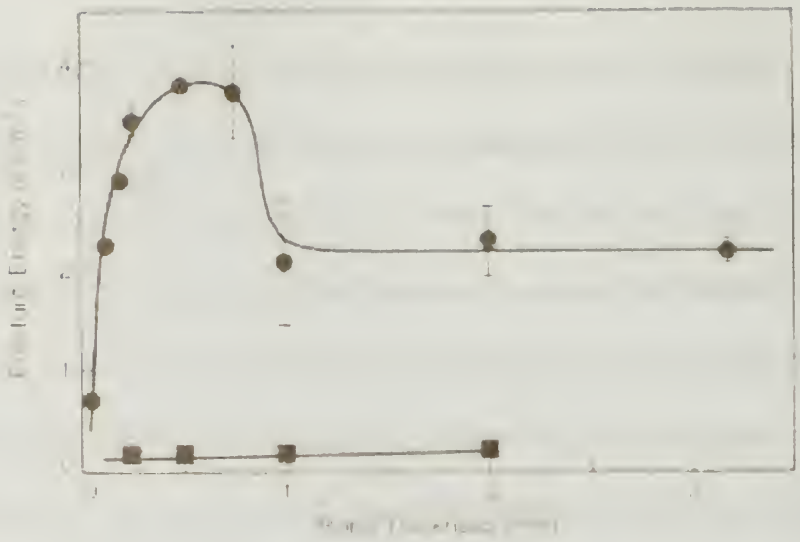

Figure 79: Kinloch's results for energy release rate with respect to adhesive thickness for a ductile rubber toughened epoxy (circles) and brittle epoxy (squares) adhesives with aluminum adherend boundaries [146].

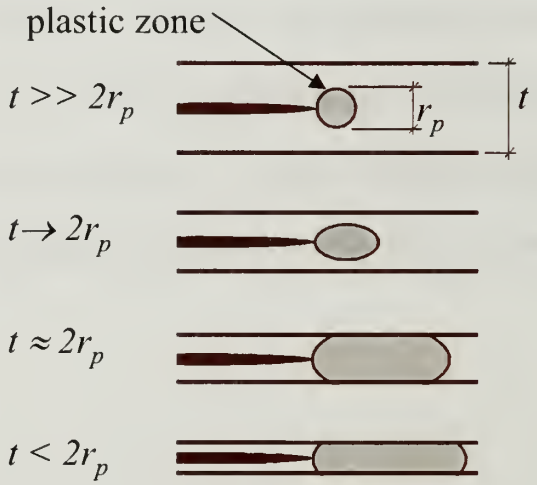

Figure 80: Qualitative effect of bond thickness on the plastic zone size of a crack propagating in an adhesive layer proposed by Kinloch et. al. [140,150], figure after Ikeda [151].

The idea of increases in plastic zone volume with constraint is plausible and can be thought of in terms of the effect of constraint on the stress distribution ahead of a

crack tip. Consider the simple Irwin plastic zone model [146] of Figure 81: the stress singularity at the crack tip decays rapidly with distance. Any material supporting stresses higher than yield undergoes plastic deformation and an estimate of the plastic zone size can be made using an energy balance. The effect of constraint imposed by a very stiff boundary placed at a distance from the crack tip commensurate with the size of the plastic zone radius is to limit the movement of material points near the boundary and create a stress concentration that shifts the stress distribution at the crack tip to even higher levels. More material is exposed to stresses above the yield stress and the volume of the plastic zone radius increases.

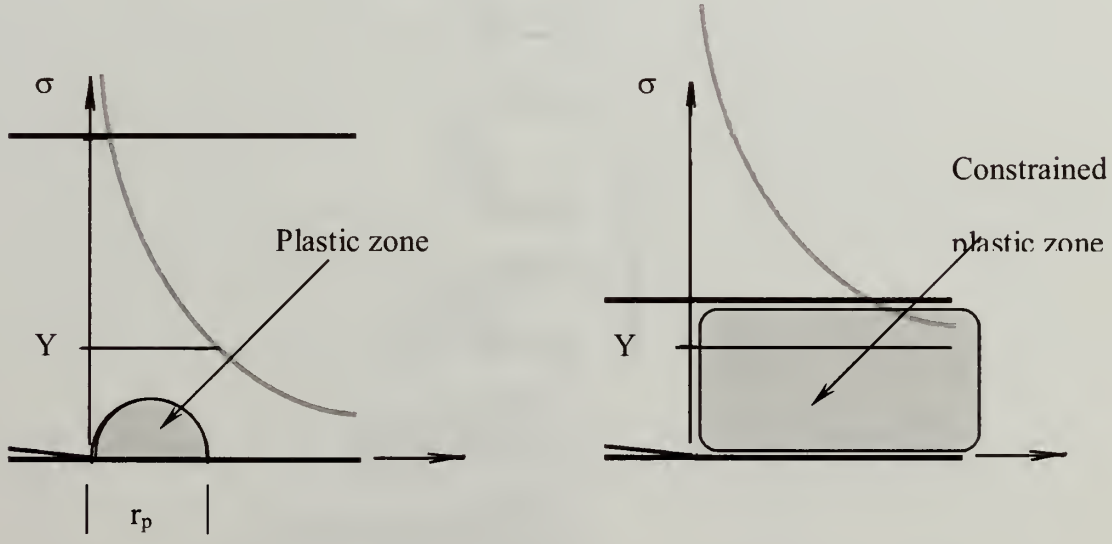

Figure 81: Schematic of the effect of constraint on plastic zone volume. Imposing constraint on material movement at the adherend boundary causes a stress concentration. As the stiff boundary approaches the length scale of the unperturbed process zone further stress concentration occurs and a larger volume of material near the crack tip yields.

Ikeda used Finite Element (FEM) and Boundary Element Methods (BEM) [151] to simulate the Bascomb and Kinloch experiments. Ikeda's simulation results are shown in Figure 82. The results are interesting in that as t approaches $2r_p$ there is increase in the

plastic zone volume, however as $t \approx r_p$ the plastic zone volume continues to increase while G_c drops. Ikeda concludes that there is no direct correlation between fracture energy and plastic zone volume, because the energy absorbed during fracture must be considered in terms of both the actual distribution of stress around the crack tip and the elastic strain energy stored in the vicinity of the crack tip. Also, Ikeda postulates that the drop in fracture energy for very thin adhesive layers may be due to a transition from cohesive failure of the adhesive to interfacial failure.

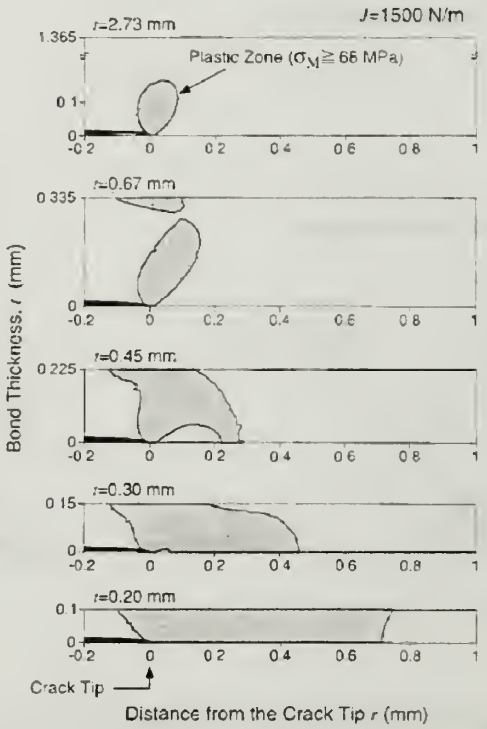

Figure 82: Ikeda's determination of distribution of plastic zone around crack tip from FEM and BEM methods [147].

Experimental approach

The objective of this work is to simultaneously measure the critical energy release rate for fracture at a bi-material interface as a function of interfacial adhesion, the relative sizes of the plastic zone radius and interlayer thickness and image the distribution of stress around the crack tip using photelastic methods. A qualitative knowledge of the stress distribution will give insight into the degree of mode-mixity imposed by the constraint. The underlying motivation is application of this technique to evaluate whether the fracture response for a crack propagating along an interface follows similar trends to those observed by Bascomb and Kinloch for a crack propagating within the interlayer.

The experimental approach used was the evaluation of the fracture behavior of a model epoxy-metal adherend system with varying degrees of plastic zone constraint and interfacial adhesion using the EWODCB testing method. The degree of constraint of the process zone was controlled by changing the thickness of the epoxy interlayer relative to the estimated plastic zone radius based on the elastic modulus, yield strength and fracture energy release rate of the bulk material,. The interfacial adhesion was altered through the use of partially cured epoxy networks which leave excess amines available to complex with oxides present on the metallic adherend surface [152].

Experimental

Materials

The model system is composed of two alloy 260 cartridge brass adherends laminated with an epoxy as illustrated in figure 83. The epoxy chemistry is detailed in Table 11. and was chosen because variation of the ratio of ethylenediamine cross-linker and N,N'-dimethylethylenediamine chain extender amine functionality to epoxide functionality allows control of the average molecular weight between crosslinks through which compressive yield strength, Young's modulus in the rubbery state, the fracture energy of the bulk material and ultimately the radius of the plastic zone around the crack tip can be manipulated.

The Derakane 322 Bisphenol-A resin (DGEBA) was obtained from Dow Corporation, ethylenediamine and N,N'-dimethylethylenediamine were purchased from Sigma-Aldrich and used as recieved. Alloy 260 cartridge brass was purchased in 12" x 12" sheets with a #8 polished surface from McMaster Carr Company. The Alloy 260 adherends were degreased with chloroform, etched in an dilute aqueous nitric acid solution, rinsed in deionized water and dried in a vacuum oven at 80°C immediately prior to bonding. PTFE spacers were used as spacers to mold the metal-epoxy laminates as described in Figure 83. The free surfaces of the epoxy are covered with glass plates treated with a silylating release agent, SurfaSil, obtained from Pierce Chemical Company, during cure to give a smooth molded surface free of defects that would be detrimental to the transmission of light during the photoelastic imaging process.

Table 11: Structures and molecular weights of monomers used in the DGEBA/EDA/DMEDA epoxy system.

Monomer	*Molecular Weight (g/mol)*
Derakane 332 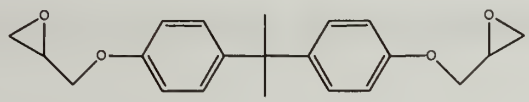	352
Ethylenediamine 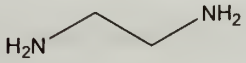	60.1
N,N'-dimethylethylenediamine 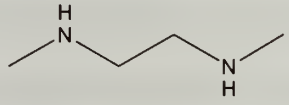	88.15

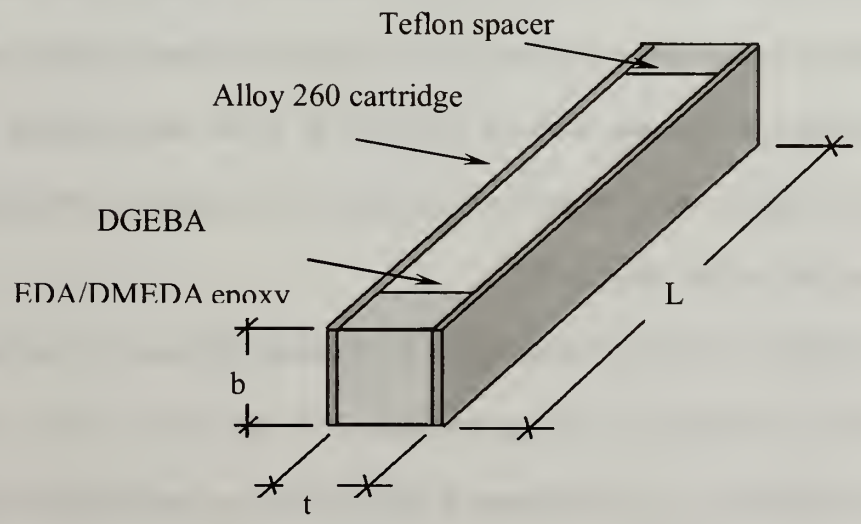

Figure 83: Elastic Wedge Opened Double Cantilever Beam (EWODCB) Specimen. DGEBA/EDA/DMEDA epoxy is cured between metallic adherends separated by PTFE spacers. The free surfaces of the epoxy are covered with glass plates during cure to give a smooth molded surface.

The structure-property relationships and cure kinetics of this class of aliphatic epoxy networks have been extensively studied by Kody and Lesser [153,154], Crawford and Lesser [155,156,157], Calzia and Lesser [158, 159], Detwiler and Lesser [160] and Baselga et al [161].

In this work two partially cured epoxy networks were used: a system with stoichiometry such that the nominal value of M_c is 380 g/mol and a second system with stoichiometry such that the nominal M_c is 818 g/mol. Both systems were cured under identical conditions: 8 hours at 50°C followed by slow cooling to room temperature. The result is two partially cured epoxy networks with a T_g near the highest temperature seen during the cure cycle. The intent of using these partially cured networks is to increase the effective molecular weight between crosslinks relative to the Mc 380 g/mol system (which contains no chain extender) with the goal of reducing yield strength while leaving Young's modulus in the glassy state relatively unchanged. In addition the partially cured network allows excess amine functionalities to complex with metal oxides present at the adherend surface. In previous work by Roche et. al. it has been observed that amine-metal oxide complexes serve to increase the ability of the interface to transfer load from the adherends to the bulk epoxy [152].

The degree of epoxide conversion of the nominal 380 g/mol Mc network cured at 50°C (323K) is estimated to be approximately 75% (the details of this estimate are described in Appendix A). This estimate is based on both an unpublished FTIR study of the DGEBA/EDA system cured at a series of temperatures from 25°C to 165°C by Detwiler and Lesser [160], and is supported by a study of the curing kinetics of

DGEBA/aliphatic amine systems undertaken by Baselga et. al.[161]. The reduced crosslink density due to incomplete conversion and network formation will result in a drop in the yield strength of the network.

Because the EDA crosslinker primary amine is more reactive than the secondary amine of the DMEDA chain extender the assumption has been made that both the nominal Mc 380 g/mol network and the nominal Mc 818 g/mol network have approximately similar crosslink density with the difference that the Mc 818 g/mol material has a significant larger excess of amine functionality available to increase adhesion at the bi-material interface.

The work of Crawford and Lesser characterizing the mechanical, thermal and fracture behavior of these controlled architecture aliphatic epoxy networks indicates that at room temperature they are in the glassy state and Young's modulus is approximately 2.1-2.7 MPa and is relatively insensitive large length scale molecular qualities like M_c [157]. The Young's modulus of the partially cured networks used in this work is therefore assumed to be of similar magnitude. Crawford and Lesser [156] and Calzia and Lesser [158] have also correlated the compressive and tensile yield strength of these aliphatic epoxy networks to T_g. An estimate of the tensile yield stress of the two partially crosslinked EDA/DMEDA/DGEBA networks has been made based on this data and indicates an approximate value of 47-55 MPa Details of this estimate are included in Appendix B. Based on this estimate of compressive yield stress the fracture energy of these two networks has been estimated from the Crawford-Lesser work relating Gc to yield strength [157] as approximately 3700 J/m^2. The resulting process zone radius as estimated by the Dugdale-Barenblatt approximation (equation 2) [159,160] is on the

order of 1mm as listed in Table 12. Table 12 also compares the mechanical and fracture properties of the incompletely cured epoxy networks with those developed by Calzia and Lesser for the fully crosslinked networks [161].

Eq 2) $$\rho \approx \frac{\pi}{8}\left(\frac{K}{\sigma_Y}\right)^2$$

Table 12: Bulk properties, and estimated plastic zone radius. of bisphenol-A/EDA/DMEDA epoxy systems with postcure at Tg + 50 K according to molecular weight between crosslinks [[a]161], and estimated bulk properties and plastic zone radius of partially cured bisphenol-A/EDA/DMEDA networks [[b]155,156,157].

M_c (g/mol)	σ^c_Y (MPa)	E (GPa)	G_q (J/m^2)	T_g (K)	R_p (mm)
[a]380	90	2.18	259	418	0.03
[b]Nom. 380	55	2.7	3700	323	0.8
[a]818	74	2.43	3115	359	0.6
[b]Nom. 818	55	2.7	3700	323	0.8

Methods

Photoelastic Imaging of Process Zone

The DGEBA/EDA/DMEDA epoxy used in these experiments is an excellent material for photo-elasticity studies being isotropic, transparent and a having good optical sensitivity to strain. Both plane and circular polariscopes were used to image the process zone surrounding the crack. The devices are illustrated in Figures 84 and 85 [164]. The strained sample is placed between a polarized and analyzer and acts as a wave plate during the propagation of the crack.

The intensity of light propagating through the sample and plane polariscope is governed by equation 3 The fringes observed in a sample are the superposition of the dark isoclinic lines ($\sin^2 2\alpha$ term of equation x) and the isochromatic lines ($\sin^2 \Delta/2$) term of equation 3). The isochromatic lines are regions with a constant magnitude principal stress difference and give a good indication of the distribution of distortional stresses. Areas with more closely spaced isochromatic lines are the regions of highest stress. Extinction bands observed for all polarizer-analyzer angles are isochromatic extinctions and correspond to regions with equal principal stresses. Isoclinic extinctions occur when the direction of the principal stresses coincides with the polarizer and analyzer directions.

The intensity of light propagating through the sample and circular polariscope is governed by equation 4. In this case the addition of two quarter-wave plates causes the removal of the isoclinic fringes leaving only the isochromatic fringes corresponding to states of equal principal stress difference or distortional stress.

Observation of the isochromatic fringes gives a qualitative indication of the shape of the process zone that can be compared to ideal Mode I, Mode II and mixed mode process zones as predicted from simulations by Dally and shown below in Figure 86 [165].

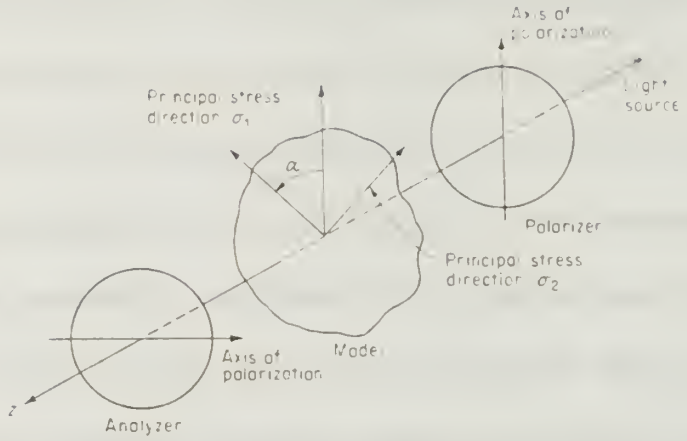

Figure 84: Schematic of a plane polariscope [164].

Eq. 3) $$I = K \sin^2 2\alpha \cdot \sin^2 \frac{\Delta}{2}$$

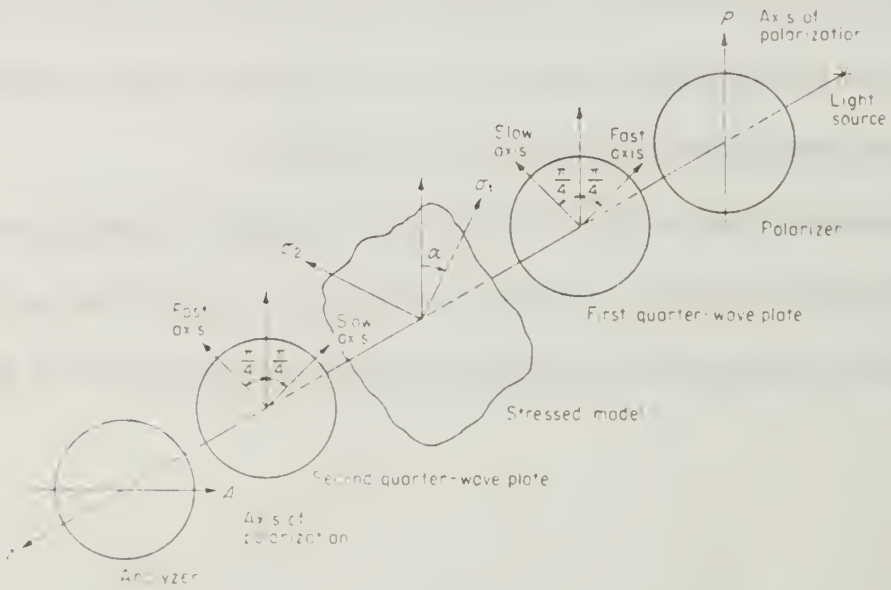

Figure 85: Schematic of a circular polariscope [164].

Eq. 4) $$I = K \sin^2 \frac{\Delta}{2}$$

Figure 86: Simulation of isochromatic fringes around a crack tip for mode I, mode II and mixed mode fracture [165].

Determination of G_c under constant load and constant displacement conditions

Determination of fracture energy for a crack advancing through a material begins with the energy approach proposed by Griffith [166]. Griffith's formalism gives the ability to define a critical energy release rate for fracture in terms of the load and displacement applied to the crack and to evaluate of the stability of the system in question.

Griffith's approach uses Gibbs free energy ($\Im$) as described in Equation 5 where $F\equiv$ the Helmholtz free energy or elastic strain energy, $W\equiv$ the work applied to the system, $\gamma\equiv$ the surface energy of new surface area and $\Sigma\equiv$ the crack surface area on one side. The sum of F and $-W$ is $-\pi$ or the elastic potential of the system. A crack may be propagated under either constant load or constant displacement conditions and π for each case is defined in Equation 5a and 5b.

For the system to be in equilibrium the change in Gibbs free energy with respect to change in surface area must be equal to zero indicating a local energy minima or maxima as in equations 6 and 7. Using the appropriate expression for the elastic potential π the expression for the critical energy release rate for fracture can be written as in equation 8. The stability of the system can be evaluated relative to these maxima or minima of energy using the second derivative of Gibbs free energy with respect to surface area of the crack as described in equation 9 and 10. Systems in which the second derivative of $\Im$ wrt. surface area created during fracture is negative are intrinsically unstable while those with a positive second derivative are stable. This stability criterion is relevant to the selection of test geometry as in an unstable system once the energy release rate threshold for fracture is reached the crack will propagate at near the wavespeed of the material. In a stable system the crack can be propagated in a quasi-steady state.

Eq. 5) $$\Im = F - W + 2\gamma \sum = -\pi + 2\gamma\Sigma$$

Where:

a) $-\pi = F - W$ Constant load conditions

b) $-\pi = F - W \; ; \; W = 0 \quad \rightarrow \quad -\pi = F$ Constant displacement conditions

Eq. 6) $$\frac{\partial \Im}{\partial \Sigma} = -\left.\frac{\partial \pi}{\partial \Sigma}\right|_{\substack{P=const. \\ T=const.}} + 2\gamma = 0$$ Energy equilibrium constant load

Eq. 7) $$\frac{\partial \Im}{\partial \Sigma} = -\left.\frac{\partial \pi}{\partial \Sigma}\right|_{\substack{\Delta=const. \\ T=const.}} + 2\gamma = 0$$ Energy equilibrium constant displacement

Eq. 8) $$G = \frac{\partial \pi}{\partial \Sigma} = 2\gamma$$

Eq. 9) $\frac{\partial^2 \Im}{\partial \Sigma^2} < 0$ Unstable system

Eq. 10) $\frac{\partial^2 \Im}{\partial \Sigma^2} > 0$ Stable system

Figure 87 shows a schematic of a linear-elastic load-displacement relationship for a crack propagating under conditions of (A) constant load or (B) constant displacement. The derivation of critical energy release rate for fracture under constant load is as follows in equations 11 through 12 where C is the compliance of the system:

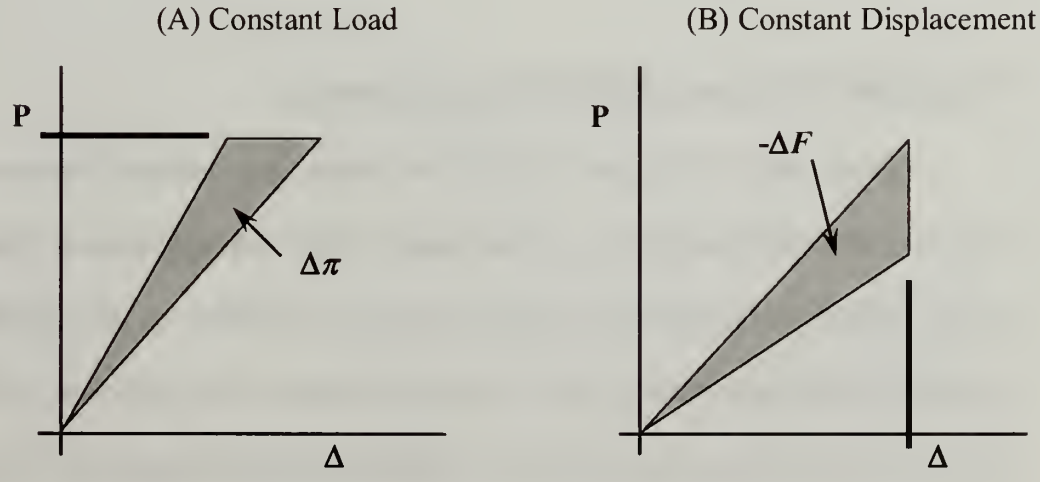

Figure 87: Schematic of Load-Displacement curves for linear-elastic crack propagation under (A) constant load and (B) constant displacement conditions.

Eq 11) $$\pi = \frac{1}{2} P\Delta = \frac{1}{2} P^2 \left(\frac{\Delta}{P}\right) = \frac{1}{2} P^2 C$$

Eq 12) $$G = \left.\frac{\partial \pi}{\partial \Sigma}\right|_{\substack{P=const. \\ T=const.}} = \frac{1}{2b} P^2 \frac{\partial C}{\partial a}$$

In a similar manner the critical energy release rate for fracture under constant displacement conditions is derived as in equations 13 and 14 Where S is global stiffness of the system:

Eq. 13) $$-\pi = F = \frac{1}{2} P\Delta = \frac{1}{2}\left(\frac{P}{\Delta}\right)\Delta^2 = \frac{1}{2}\Delta^2 S$$

Eq. 14) $$G = -\left.\frac{\partial F}{\partial \Sigma}\right|_{\substack{\Delta=const. \\ T=const.}} = -\frac{1}{2b}\Delta^2 \frac{\partial S}{\partial a}$$

Determination of G_c using EWODCB testing geometry

Beam theory can be used to define the change in compliance with crack length in terms of either the loads acting on the sample or the displacements as follows: A free body diagram representing the geometry and load condition of the sample is used to establish the moment acting along the length of the beam. The deflection of the beam can then be related to the moment using the Castigliano's theorem (equations 15 and 16):

> *Deflection at any point and direction is the partial derivative of strain energy including all loads with respect to a load acting at that point and in that direction*

Eq. 15) $$U = \int \frac{M^2}{2EI} dx$$

Eq. 16) $$\Delta = \frac{\partial U}{\partial Q}$$

If there is no load acting at the point of interest then a dummy load Q acting at the point of interest is included in the free body diagram used to define the moment distribution. The resulting expressions for bending energy are then derivated with respect to Q to derive an expression for the deflection at that point with respect to the load and geometric attributes of the sample geometry.

The EWODCB specimen consists of a laminate of two stiff elastic adherends surrounding a polymer interlayer. As shown in Figure 88, a thin wedge is translated at a constant velocity in such a way that one adherend and the polymer interlayer are separated under a constant displacement condition. The displacement created by the wedge is of a small enough magnitude relative to the dimensions and modulus and yield stress of the metallic adherends that any deformation in the adherend is considered to be elastic. Direct measurements of crack length during the test and the width of the wedge are used to determine the critical energy release rate. Alternatively a crack may be propagated within a similar Double Cantilever Beam (DCB) specimen under constant load conditions in which the crack opening displacement increases as the crack is propagated. In this last case the deformation of the adherend may have both a plastic and elastic component, in addition thermodynamic stability considerations dictate that the constant displacement mode EWODCB specimen is best suited to propagation of a crack in a quasi-steady state condition.

Figure 88 illustrates a free-body diagram and moment diagram of the EWODCB specimen. The fracture energy is calculated from the load-displacement relationship and the constant displacement critical energy release rate defined in equation 14. The total bending energy, load-displacement relationship, global system stiffness S_T and expression

for $\partial S_T/\partial a$ are calculated as in equations 17 through 19. The resulting expressions for plane strain and plane stress fracture energy under constant displacement conditions are given as equations 20 and 21. An analogous derivation of fracture energy for constant load conditions is described by equations 22 and 23 and the plane strain and plane stress fracture energy expressions are given by equations 24 and 25

It should be noted that these constant displacement and constant load analyses are based on the assumption of linear elasticity. If the displacement of the EWODCB specimen is such that plastic deformation occurs in the legs of the beam behind the crack tip this analysis would need to be modified. In this work the deflections under constant displacement conditions are small enough that complete elastic recovery is observed and the linear elastic assumption is valid.

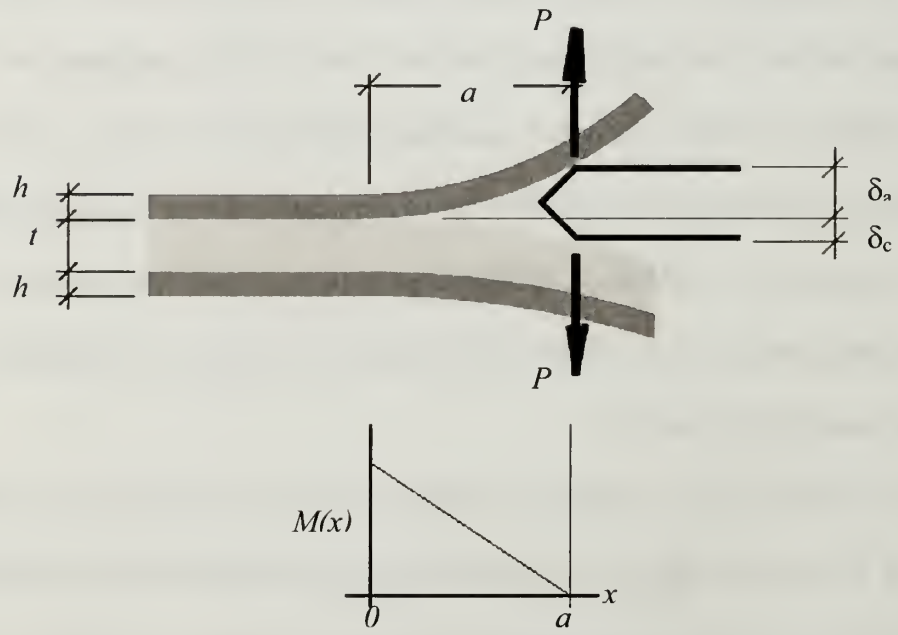

Figure 88: Elastic Wedge Opened Double Cantilevered Beam test used to determine critical energy release rate (G_c) of a bi-material interface under constant displacement conditions.

Eq. 17) $$U_a + U_c = \int_0^a \frac{(px)^2}{2E_aI_a}dx + \int_0^a \frac{(px)^2}{2E_cI_c}dx$$

Eq. 18) $$S = \frac{P}{\delta_T} = \frac{3}{a^3}\left(\frac{E_aI_aE_cI_c}{E_aI_a + E_cI_c}\right)$$

Eq. 19) $$\frac{\partial S_T}{\partial a} = -\frac{9}{a^4}\left(\frac{E_aI_aE_cI_c}{E_aI_a + E_cI_c}\right)$$

Eq. 20) $$G_c = \frac{9}{2a^4b}\delta_T{}^2\left(\frac{E_aI_aE_cI_c}{E_aI_a + E_cI_c}\right)$$ plane stress, in terms of displacement

Eq. 21) $$G_c = \frac{9(1-\upsilon^2)}{2a^4b}\delta_T{}^2\left(\frac{E_aI_aE_cI_c}{E_aI_a + E_cI_c}\right)$$ plane strain, in terms of displacement

Eq. 22) $$C = \frac{\delta_T}{P} = \frac{a^3}{3}\left(\frac{E_aI_a + E_cI_c}{E_aI_aE_cI_c}\right)$$

Eq. 23) $$\frac{\partial C}{\partial a} = a^2\left(\frac{E_aI_a + E_cI_c}{E_aI_aE_cI_c}\right)$$

Eq. 24) $$G_c = \frac{P^2a^2}{2b}\left(\frac{E_aI_a + E_cI_c}{E_aI_aE_cI_c}\right)$$ plane stress, in terms of load

Eq. 25) $$G_c = \frac{P^2a^2(1-\upsilon^2)}{2b}\left(\frac{E_aI_a + E_cI_c}{E_aI_aE_cI_c}\right)$$ plane strain, in terms of load

Stability criterion

A comparison of the stability criterion stated in Equations 9 and 10 evaluated under both constant load and constant displacement conditions indicates that the fracture in a DCB system is unstable under constant load and stable under constant displacement. In Equation 26 the second derivative of the Gibbs free energy of the DCB system under

constant load is stated. The negative quantity indicates an unstable system. The expression for the second derivative of Gibbs free energy of the DCB system under constant displacement is stated in equation 27 and the positive quantity indicates the specimen is stable under constant displacement conditions. The stability of the constant displacement loaded EWODCB specimen is convenient experimentally as once the full width of the wedge has been introduced both the translational force required to propagate the crack and the length of the crack reach a quasi-equilibrium state. The latter condition is convenient experimentally as the specimen can be arranged in a tensile testing machine in such a way that the wedge is fixed and the laminate translated. Once the steady-state crack length has been reached the process zone is then in an approximately fixed position and can be easily imaged throughout the test.

Eq. 26) $$\frac{\partial^2 \Im}{\partial \Sigma^2} = -\frac{\partial^2 \pi}{\partial \Sigma^2} = -\frac{P^2}{2b}\left(\frac{\partial^2 C}{\partial a^2}\right) = -\frac{P^2 a}{b}\left(\frac{E_a I_a + E_c I_{cc}}{E_a I_a E_c I_c}\right)$$

$$\therefore \frac{\partial^2 \Im}{\partial \Sigma^2} < 0 \quad \text{EWODCB unstable system under constant load}$$

Eq. 27) $$\frac{\partial^2 \Im}{\partial \Sigma^2} = \frac{\partial^2 F}{\partial \Sigma^2} = \frac{\partial}{\partial \Sigma}\left[-\frac{9}{2a^4 b}\delta_T{}^2\left(\frac{E_a I_a + E_c I_{cc}}{E_a I_a E_c I_c}\right)\right] = \frac{9}{2a^5 b^2}\delta_T{}^2\left(\frac{E_a I_a + E_c I_{cc}}{E_a I_a E_c I_c}\right)$$

$$\therefore \frac{\partial^2 \Im}{\partial \Sigma^2} > 0 \quad \text{EWODCB stable system under constant displacement}$$

The EWODCB specimen geometry has been developed in this work as an alternative to another test geometry that has been previously applied to measure the interfacial fracture energy of thin laminates of metals, polymers and metal oxides within the context of microelectronics applications. The Four Point Bend test or FPB geometry

was proposed by Charalambides et. al. [167] and has been used to characterize the fracture response of multilayered structures by Dauskardt et. al. [168]. The sample geometry, shown below in Figure 89, consists of two stiff adherends separated by a polymer interlayer. One of the adherends is notched at the midpoint and a pre-crack is incorporated. The Four Point Bend test geometry is one of crack propagation under constant load.

An analysis of the relationship of G_c to the load applied to the beam and the stability of the system similar to that applied to the EWODCB sample in the previous section is documented in Appendix C. The system stability as evaluated using second derivative of the Gibbs free energy with respect to crack length indicates that the crack propagates under a constant potential. This constant potential characteristic results in the primary advantage of the FBP test geometry - that G_c can be determined from measurement of the applied load only and crack length a need not be measured.

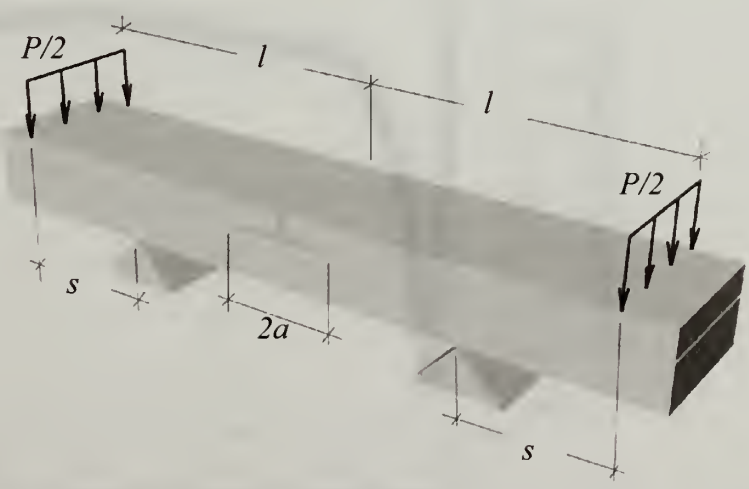

Figure 89: Four Pont Bend Test specimen consisting of two stiff adherends separated by a polymer interlayer. One of the adherends is notched at the midpoint and a pre-crack is incorporated using a release film.

Stability of EWODCB specimens during testing

The theoretical evaluation of EWODCB stability under constant displacement conditions is confirmed by observations of the force-displacement curves during testing. Figure 90 shows a typical curve. The translational force needed to push the wedge into the interface is large at first but once the full thickness of the wedge is introduced the crack attains an equilibrium length and the force needed to translate the wedge reaches a plateau. The EWODCB technique is both simple from an experimental and analytic perspective and convenient for the proposed imaging work because it can be arranged in such a way that the wedge and crack tip remain in a fixed position while the laminated specimen translates past the field of view of the imaging device.

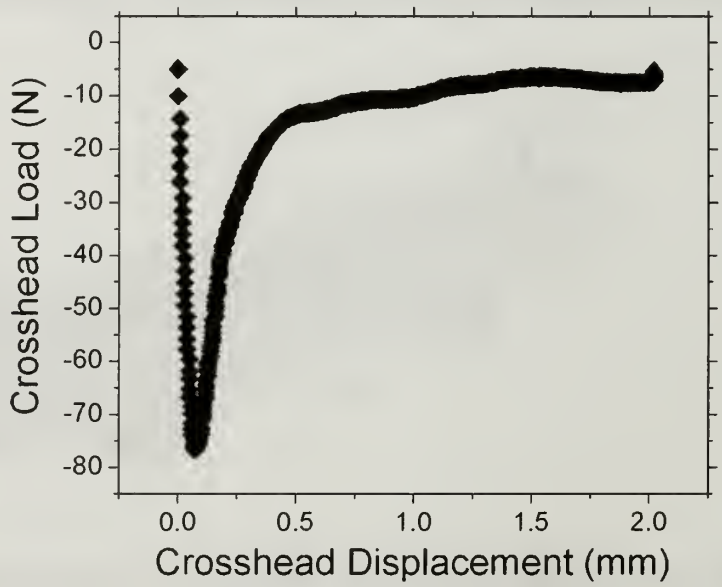

Figure 90: Force displacement curve recorded during EWODCB test showing the plateau in force when crack propagation has reached a steady state.

Residual Stress in EWODCB specimen

Laminates of materials having dissimilar coefficients of thermal expansion may be subject to large stresses imposed by both volume change during cure and differential thermal expansion when returned to ambient temperature [144]. Given very stiff system boundaries these stresses can easily become large enough to cause yielding in epoxies and in the context of fracture specimens would impose an additional load that must be accounted for during a study of fracture behavior.

To this end an estimate of the volume change upon cure for the EDA/DMEDA M_c 380 g/mol system due to the combined action of contraction during network formation and thermal expansion was made using a specimen prepared with the same materials and cure schedule as the EWODCB specimen but using a spacer made of compliant Viton rubber tubing. An example of this specimen is shown in Figure 91 as viewed through a plane polariscope with polarizing axes at 45 degrees to horizontal. The isochromatic fringes show that the stress state is not constant through the thickness and along the length of the beam. There is higher distortional stress at the adherend/epoxy interface and at the sample ends due to differences in the thermal expansion coefficients of the adherend and epoxy materials.

. The change in the thickness dimension after cure was measured and the result indicated approximately 4.5% volume change upon cure and return to ambient temperature. If the epoxy surface was rigidly constrained in all three axes the resulting residual hydrostatic stress can be estimated using equations 28 and 29, and assuming a Young's modulus of ~2.7 GPa [156], to be approximately 200 MPa well in excess of the 47-55 MPa yield strength of this partially cured epoxy system [156,158]. Because the

brass adherends are comparatively thin they do not impose a completely rigid boundary and so the residual stress imposed by volume change and differential thermal expansion during cure is lower.

Figure 91: Photoelastic image of stress distribution in an partially cured Mc 380 EDA epoxy/Alloy 260 cartridge brass laminate made using compliant viton tubing spacers and glass plate molding surfaces at the top and bottom. The specimen was used to estimate the magnitude of contraction of the epoxy network during cure.

Eq. 28) $$\sigma_m = Ke_m$$

Eq. 29) $$K = \frac{E}{3(1-2\upsilon)}$$

An estimate of the actual magnitude of residual stress in these samples was made using the deflection of the alloy 260 addherend. Figure 92 is a schematic representation of the deformation of the EWODCB specimen due the volume change experienced during cure. Considering each adherend to be an elastic beam supporting a distributed load equations 30 and 31 relate the deflection of the adherend to the hydrostatic pressure p_o imposed by the epoxy cure cycle. For EWODCB specimens fabricated using the nominal M_c 380 g/mol system Table 13 shows that p_o is estimated to be at less than 30 KPa, quite small relative to the yield stress of the epoxy material.

On this basis the stresses imposed on the EWODCB specimens by differential thermal expansion during cure are found to be small enough that they will not have a large effect on the fracture response EWODCB specimen.

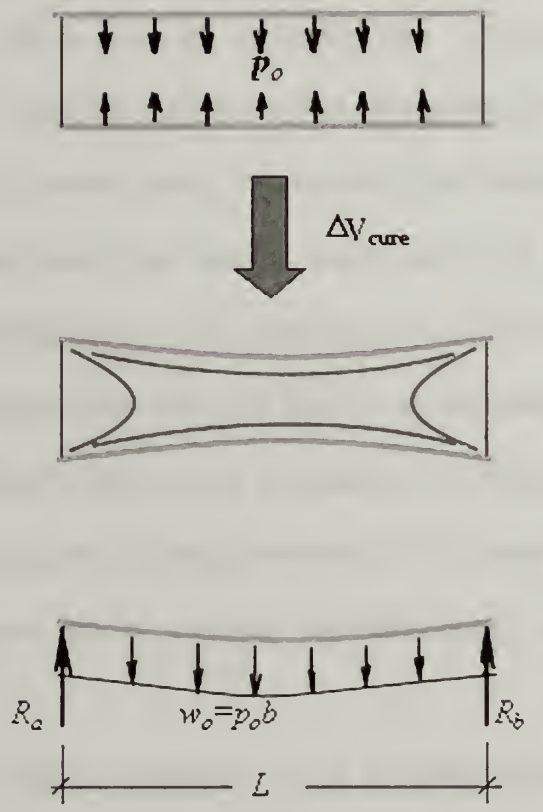

Figure 92: Estimation of hydrostatic tension present in EWODCB specimens due to contraction during cure at elevated temperature using adherend deformation.

Eq. 30) $$v = \frac{-p_o b}{24EI}\left[x^4 - 2Lx^3 + 6L^3\right]$$

Eq. 31) $$\delta\left(L/2\right) = \frac{p_o b L^4}{384EI}$$

Table 13: Estimate of hydrostatic tension due to change in volume during cure using adherend deflection at L/2 for a population of 1.5mm and 3.25mm thick Mc380 g/mol EDA epoxy EWODCB specimens. L/2 deflection standard deviations given in parenthesis

$t_{nominal}$ (mm)	$\delta(L/2)$ mm	p_o (KPa)
1.5	0.1567 (0.0522)	27.5
3.25	0.451 (0.0854)	18.5

Fracture energy from EWODCB testing

The critical energy release rate (G_c) with respect to the ratio of thickness to estimated plastic zone radius for a crack propagating at the adherend-interlayer interface in each of the partially crosslinked nominal 380 g/mol and 818 g/mol networks is shown in Figure 93. The nominal Mc 380 g/mol specimens showed very small interfacial fracture energy on the order of 10's of J/m^2. The magnitude of G_c is unaffected by the degree of process zone constraint as described by the ratio t/r_p. This result indicates that the interface is weak enough that dissipative mechanisms due to plastic deformation within the epoxy interlayer are not activated. The G_c observed is then commensurate with a threshold fracture energy for this epoxy-adherend interface in the absence of viscoelastic dissipation mechanisms.

In contrast the nominal 818 g/mol network has G_c magnitude on the order of 100's of J/m^2 indicating a stronger interface capable of activating viscoelastic dissipation mechanisms. There is an increase in G_c as the degree of constraint reaches a t/r_p of ~2 and a drop in G_c for $t/r_p < 2$. Although the data show considerable variability this result is qualitatively similar to the results for the effect of constraint in bulk systems examined by Bascomb and Kinloch [140,141].

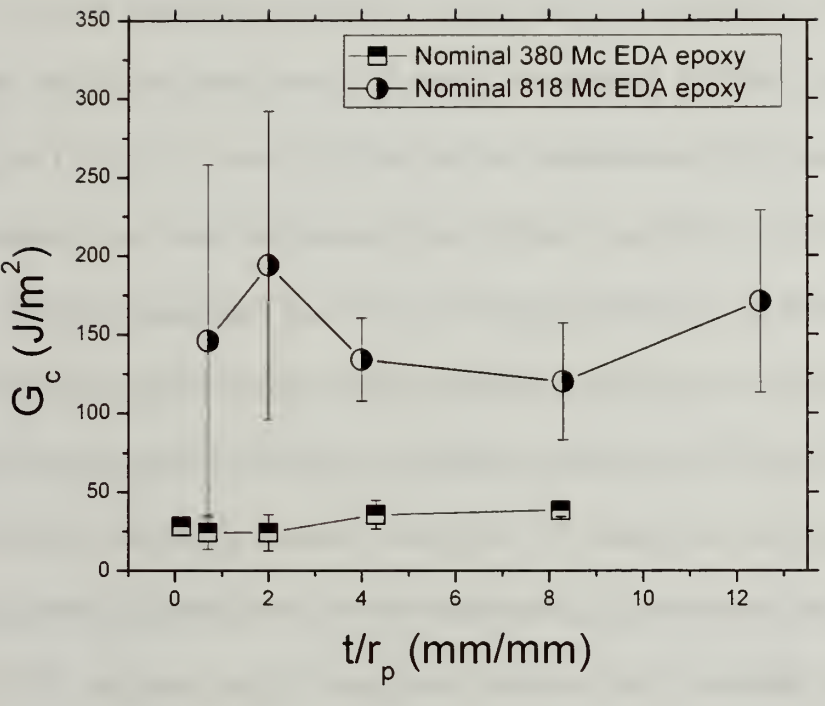

Figure 93: Plot of G_c with respect to the ratio t/r_p as measured using the EWODCB specimen based on nominal molecular weight between crosslinks of 380 g/mol and 818 g/mol.

Photoelastic imaging of process zone

Photoelastic imaging of the process zone around the crack tip enabled accurate observation of the crack length. Because the G_c is proportional to a^{-4} an reproducible and accurate measure of crack length is critical to the successful application of the EWODCB method to determine fracture energy. Figure 94 shows a crack tip viewed through a plane polariscope. The convergence of isochromatic fringes at the lower adherend indicates the location of the crack tip (marked by white arrows) and this feature was found to be easy to identify even in the smallest 0.5 mm thick DGEBA/EDA/DMEDA interlayers used in this work.

Figure 94 shows the distribution of distortional stresses crack tips propagating at the interface of nominal M_c=380 g/mol EWODCB specimens with $0.7<t/r_p<8.3$ as imaged using a circular polariscope. Figure 95 shows plane polariscope images of the same specimens with polarization axes at +45°/-45° and at 0°/90°. The isochromatic fringes in both sets of images indicate shear stresses and show that the process zone is inclined forward at ~30° from vertical even in the least constrained samples. Comparison with the process zone simulations of Dally indicates mixed Mode I and Mode II fracture exists in the EWODCB specimen. Examination of both the circular and plane polariscope images shows that the inclination of the process zone is similar for all ratios of t/r_p and implies that the mode-mixity is primarily due to the lower adherend restricting movement of the epoxy adhesive at the interface just ahead of the crack tip. The 0°/90° plane polarized images of figure 95 show isoclinic extinction ahead of the process zone and indicate the axes of principal stress are at approximately 0° and 90°. The isochromatic lines in the 0°/90° plane polarized images show shear stresses at ±45° both in the active zone surrounding the plastic zone and in the passive zone behind the crack tip. Inspection of both sets of plane and circular polariscope images shows that at t of approximately 1.5 mm ($t/r_p \approx 2$) the distribution of distortional stress ahead of the crack tip transitions from being a gradient to approximately constant across the specimen thickness. This saturation of distortional stress in this nominal M_c=380 g/mol network coincides with the transition to weak increase in G_c with specimen thickness at $t/r_p \approx 2$ shown in Figure 93.

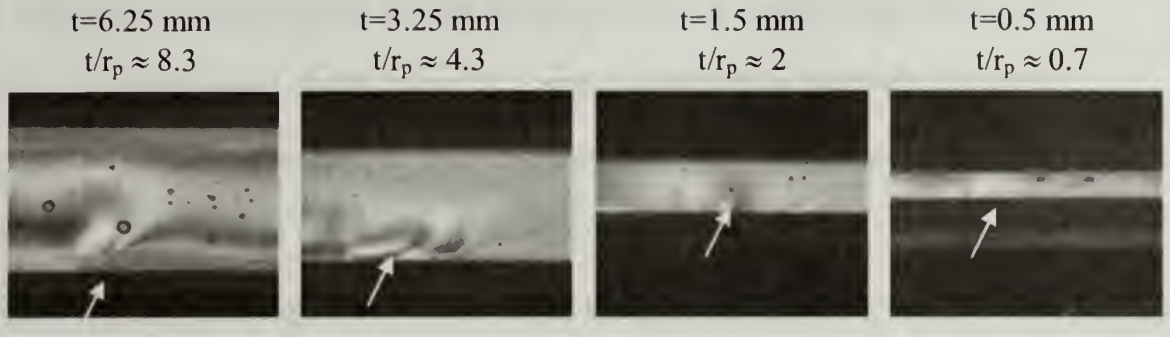

Figure 94: Circular polariscope images of the distribution of distortional stress around propagating crack tip for M_c=380 g/mol EDA epoxy system with varying thickness bondlines (0.7<t/rp<8.3). The crack is propagating from the lower left corner of each image. The crack tip region is indicated by white arrows.

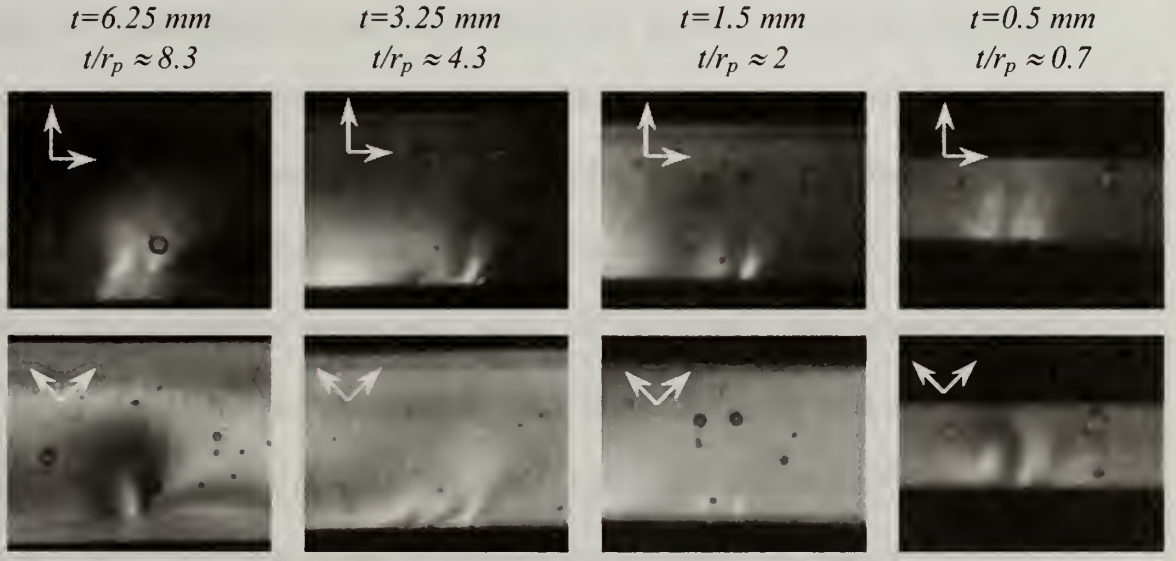

Figure 95: Plane polariscope images of the distribution of disortional stress around propagating crack tip for M_c=380 g/mol EDA epoxy system with varying thickness bondlines (0.7<t/rp<8.3). The crack is propagating from the lower left corner of each image arrows show direction of polarizer and analyzer axes.

Figure 96 shows the distribution of distortional stresses crack tips propagating at the interface of M_c=818 g/mol EWODCB specimens with $15 < t/r_p < 2$ as imaged using a circular polariscope. Figure 97 shows plane polariscope images of the same specimens with polarization axes at +45°/-45° and at 0°/90°. Similarly to the M_c 380 g/mol system

the isochromatic fringes in all three sets of M_c 818 g/mol process zone images indicate forward inclination of the process zone and mixed Mode I and Mode II Fracture. The angle of inclination is ~ 45° and is not strongly dependent on the degree of constraint until t/r_p of ~ 2 so the mode mixity is most probably due to constraint of motion at the lower adherend/epoxy interface and ahead of the crack tip rather than the effect of the upper adherend/epoxy interface. The larger angle relative to the M_c 380 g/mol system indicates a larger proportion of Mode II fracture. As the degree of constraint increases and $t/r_p \approx 2$ the inclination of the process zone decreases indicating that the constraint of the upper adherend is having an effect on the stress didstribution. The Figure 97 polariscope images with 0°/90° polarization axes show isoclinic extinction ahead of the crack tip indicating that the principal stress directions are coincident with the polarizer/analyzer axes in these regions. The isochromatic fringes present in these same images indicate shear stresses in the active zone region oriented at ±45°. Unlike the nominal M_c 380 system there are no shear stresses with ±45° orientation in the passive zone behind the crack tip until $t/r_p \approx 2$. Although the plastic zone radius is estimated to be commensurate with the length scale of the M_c 818 g/mol specimens it is not possible to directly discern the plastic zone regions from the photoelastic images so no conclusions about the volume of plastically deformed material as a function of t/r_p can be made.

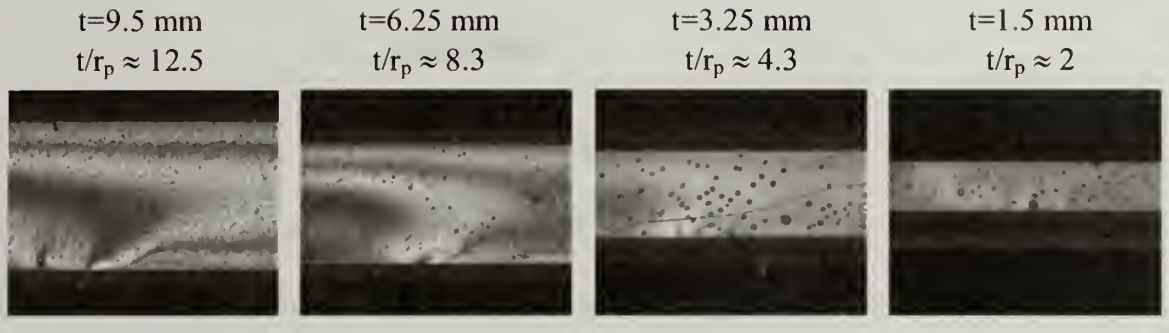

Figure 96: Circular polariscope images of the distribution of distortional stress around propagating crack tip for M_c=818 g/mol DMEDA epoxy system with varying thickness bondlines (2<t/rp<12.5). The crack is propagating from the lower left corner of each image.

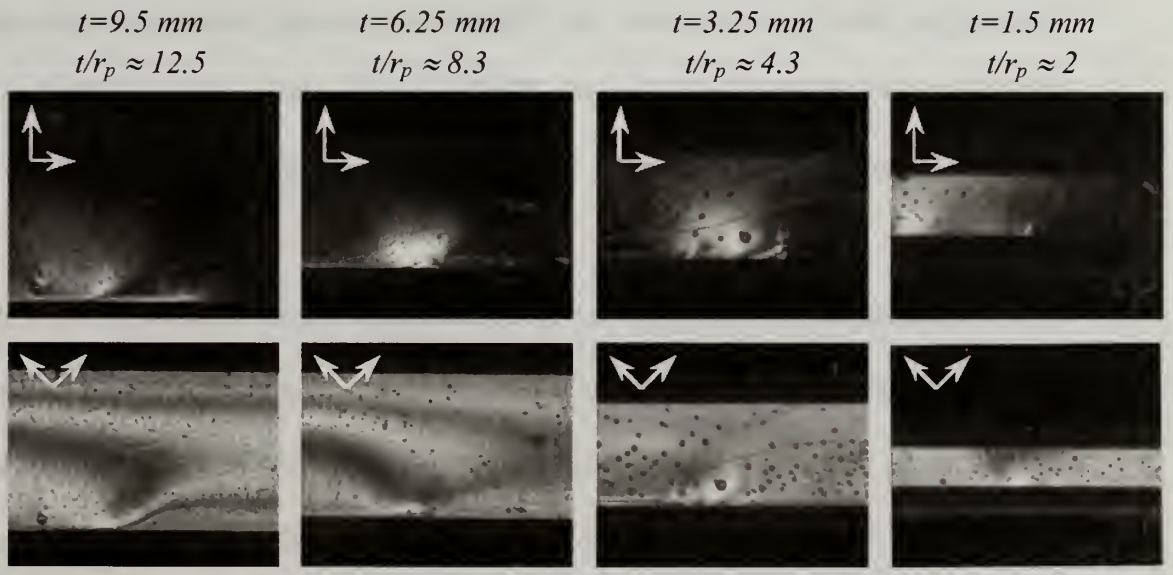

Figure 97: Plane polariscope images of the distribution of disotrtional stress around propagating crack tip for M_c=818 g/mol DMEDA epoxy system with varying thickness bondlines (2<t/rp<12.5). The crack is propagating from the lower left corner of each image.

Conclusions

Relative merits of EWODCB and FPB specimens

Both the EWODCB and FPB specimen geometries allow determination of interfacial fracture energy from relatively simple measurements of crack opening displacement and crack length or load respectively.

Stability analysis based on the Gibbs potential indicates the crack propagation in the EWODCB specimen is stable under constant displacement and unstable under constant load. The force-displacement curves observed during EWODCB testing confirm this analysis showing a plateau in crack length and force once steady-state propagation of the crack under constant crack opening displacement has been achieved. Similar analysis of the FPB system shows it to be at a constant Gibbs potential under constant load crack propagation.

Although the FPB system energetics have been shown to allow steady-state crack propagation, because there are two crack fronts propagating simultaneously, the points of contact of the FPB beam with the load must be in parallel planes or the moment between the two inner points of contact is no longer constant between $s<x<(2l-s)$ and the system will become unstable.

An advantage of the FPB system is that because of the constant moment and hence constant Gibbs potential characteristics fracture energy can be determined directly from the load measured during crack propagation which can be easily and accurately measured.

In contrast determination of fracture energy from the EWODCB specimen requires accurate measurements of crack opening displacement and crack length. Because the EWODCB functional relationship between fracture energy and crack length goes as a^{-4} the method of measuring a is of first importance. A simple solution to the problem of directly measuring crack length is the use of a polariscope to both locate the crack tip and qualitatively image the stress distribution around it.

Residual Stress in EWODCB specimens

Evaluation of the volume change during cure shows that a sample made with rigid boundaries would experience residual stresses due to volume change on cure and thermal expansion mismatches well in excess of the yield strength of the epoxy networks used. However, because the metallic adherends used in the EWODCB are relatively thin they do not represent a rigid boundary. Evaluation of deflection of the adherends after cure was used to estimate the residual stress acting normal to the adherend surface at a relatively low magnitude of 20-30 KPa.

Effect of constraint on G_c and stress distribution near the crack tip

In the partially cured M_c 380 g/mol aliphatic system the magnitude of interfacial fracture energy was on the order of 10's of KJ/m^2. The fracture energy was approximately constant regardless of the degree of constraint implying that the interface was not strong enough to activate viscoelastic dissipation mechanisms in the polymer interlayer. This magnitude of fracture energy is thought to be similar to the threshold fracture energy G_o for this aliphatic epoxy network and alloy 260 brass adherend.

Differing response was observed in the partially cured M_c 818 g/mol aliphatic system. The magnitude of interfacial fracture energy was observed to be on the order of 100's of KJ/m^2. Also there was in increase in fracture energy as the degree of constraint was increased to $t/r_p \approx 2$ followed by a drop in fracture for $t/r_p < 2$. This implies that the increased concentration of amines available to complex with the metallic adherend surface increased the threshold fracture energy of the bi-material interface enough that viscoelastic dissipation mechanisms were activated. There is variability in the measurement of G_c but the observations show that fracture energy of a bi-material interface has a response to constraint that is qualitatively similar to that observed in bulk materials.

Photoelastic imaging of the process zone during crack propagation was used to observe the effect of constraint on the stress distribution around the process zone. Comparison of the photelastic stress distribution with simulations by Dally indicates that in the EWODCB specimens prepared with nominal 380 g/mol and 818 g/mol epoxy networks interlayers the constraint imposed by the adherend adjacent to and ahead of the crack tip resulted in a mixed mode fracture process. The angle of inclination away from the ideal Mode I distribution was greater in the nominal 818 g/mol interlayer that had a larger fracture energy.

CHAPTER 6

CONCLUSIONS AND SUGGESTIONS FOR FUTURE WORK

ESC of Glassy Thermoplastics

The critical stress for unbounded swelling embodied in the Gent hypothesis was evaluated by observing the wetting behavior of ESC liquids on polycarbonate substrates as a function of substrate stress. Wetting was quantified using JKR based Contact Adhesion Testing and measurements of three phase contact angle by a refraction method. The CAT results indicated that contact angle is independent of substrate for the small strain level tested and three phase contact angle can be observed directly as a potential indicator for the Gent transition to unbounded swelling. The observations of three phase contact angle using both the refraction method and conventional goniometry showed that while contact angle is a good metric for swelling there was no discernable transition to in wetting behavior with stress to support the Gent hypothesis. Elastic and inelastic strain conditions were also observed and a transiton in inelastic strain response at stress levels commensurate with the Gent hypothesis was noted.

The time to crazing was observed for a series of homolgous ESC liquids on polycarbonate substrates. The ratio of substrate stress to the square of solubility difference between polymer and ESC liquid was found to be a good indicator of thermodynamic potential for crazing though not for time to the onset of crazing. Larger ESC liquid molecules at higher potential crazed in a similar time period as smaller ESC liquid molecules at lower potential. Diffusion coefficients of these liquid/polymer pairs were estimated and correlated to the molar volumes of the ESC liquids. The correlation

was then used to normalize the thermodynamic potential term and the observations of time to the onset of crazing for this homolgous series of ESC liquids was found to collapse reasonably well onto a single curve.This result is limited to relatively short time scales and a series of similar ESC liquids on a single substrate, but if it can be shown to be more general the approach has the potential to be used as a crazing failure criterion. Future work in this area would include observations time to crazing and diffusion coefficients of a wider range of polymer substrate/ ESC liquid pairs

Environmetal Degradation and Stabilization of Poly-p-phenylenebenzobisoxazole Fibers

The degradation mechanisms for PBO AS fibers exposed to moisture and UV-Vis spectrum light were investigated. Degradation by moisture was found to be primarily physical in nature. The effect of liquid and vapor phase water is to loosen the fiber's fibrillar microstructure and introduce larger size and number of defects. Spectroscopic studies indicate that residual phosphoric acid does not cause a significant amount of chemical degradation. The role of residual acid in degradation may be primarily in attracting moisture to the interior of the fiber. In contrast degradation by UV-Vis light is a chemical process involving disruption of the oxazole ring structure and possible formation of an amide linkage.

Approaches to the stabilization of PBO AS fibers were formulated and tested including super-critical fluid extraction of residual phosphoric acid, application of UV-Vis blocking coatings, compaction of the fiber micro-structure and composites of PBO AS fiber and polysiloxanes prepared in $scCO_2$. Super-critical fluid extraction did remove a portion of the residual phosphoric acid but the stability of the fiber was not markedly improved though the $scCO_2$ itself did not degrade the fiber appreciably. The exfoliated

graphite, carbon black and titanium dioxide coatings used to block UV-Vis radiation were unsuccessful due to incomplete coverage. Requirements for a successful coating approach to fiber stabilization are a compliant material that can form a compliant coating able to both absorb UV-Vis damage and exclude water over a long period of time. A good candidate material for this application is a conformal coating of poly-p-xylylene applied to the fiber surface using plasma polymerization. Compaction of the fiber using twist, tension, pressure and heat showed some small improvements in initial fiber properties but not enough to warrant much further investigation. Preparation of PBO AS/siloxane composites in $scCO_2$ is a promising route to improving the fiber's resistance to degradation by moisture. This preliminary work showed that it is possible to infiltrate the PBO fiber with crosslinked siloxane to some extent and that the process does compact the fiber micro-structure. Whether this has resulted in either an increase in fiber tenacity or the introduction of inter-fibrillar secondary forces capable of preventing expansion by moisture is not indicated in this work.

Future work would include exploration of the poly-p-xylylene approach to a UV-Vis radiation and moisture resistant coating. The effect of impregnation of the PBO fiber by crosslinked siloxanes on environmental stability and initial mechanical properties would also be an appropriate avenue of future work. Application of EDAX techniques to ascertain how far into the fiber the siloxanes have penetrated and the use of single fiber tensile testing, single fiber torsion and single fiber recoil tests to determine the impact on tensile and compressive properties.

Fracture in Constrained Geometries

The interfacial fracture energy of a model epoxy/metallic-adherend system was measured as a function of the degree of constraint imposed by the adherend for two partially cured aliphatic epoxy systems Using the EWODCB test geometry. Partially cured networks were used to increase the effective molecular weight between crosslinks in the network thereby lowering yield strength while leaving the glassy modulus essentially unchanged. Excess diamine present in the nominal M_c 818 g/mol network containing DMEDA chain extender served to increase adhesion at the polymer-metal adherend interface.

The results show that if the polymer-adherend interface is strong enough similar trends to those previously observed for the effect of constraint on cohesive fracture within an epoxy adhesive bond-line, though the fracture energy an orders of magnitude smaller. The nominal M_c 380 g/mol system having a weaker polymer-adherend interface showed a weak increase in fracture energy as the ratio of t/r_pincreased. A possible threshold was observed at $t/r_p \approx 2$. The more ductile system showed essentially constant fracture energy until the t/r_p was reduced to ~2 when fracture energy showed a large increase followed by a drop for $t/r_p < 1$. The photoelastic imaging results did generally show how the shape of the process zone changed with constraint but gave no indication of the actual size of the plastic zone that could be compared with the plastic zone simulations of Ikeda and plastic zone observations of Kinloch.

Further work would include measuring fracture energy with a system having more interfacial strength and even more ductile epoxy interlayers. A quantitative application of the photelastic technique to indicate the plastic zone size would also be appropriate.

APPENDIX A: EPOXIDE CONVERSION IN INCOMPLETELY CROSSLINKED EDA/DMEDA EPOXY NETWORKS

The degree of conversion of epoxide groups in the partially cured EDA/DGEBA epoxy networks used in this work has been estimated from an unpublished FTIR study undertaken by Detwiler and Lesser [162]. An mixture of EDA crosslinker and DGEBA epoxy was prepared with stoichiometry such that full conversion would result in a 380 g/mol molecular weight between crosslinks. The mixture was cured at several temperatures and FTIR spectra collected of the partially cured networks and an unreacted mixture of EDA and DGEBA. The areas of the amine peak at 6480 cm^{-1} and the aromatic C-H Peak at 4680 cm^{-1} were used to calculate the degree of epoxide conversion. The results are tabulated in Table 14. Figure 98 shows an exponential curve, described by Equation 1, fit to the data. This equation was used to roughly estimate the degree of cure in the EDA/DGEBA networks cured at 50°C (232 K) and subsequently used in the EWODCB specimens at approximately 72%.

A similar degree of epoxide conversion was observed by Baselga et. al. [163]: The percent epoxide conversion of an EDA/DGEBA network with identical stoichiometry cured at 40°C (313 K) was ~65%-70%.

Table 14: Epoxide conversion in Mc 380 g/mol EDA/DGEBA epoxy network with respect to curing temperature. The % epoxide conversion is calculated based on FTIR spectra of an unreacted mixture of EDA and DGEBA and networks crosslinked at varying temperatures [162].

Crosslinking Temperature (K)	% Epoxide Conversion
293	66
353	82
438	86

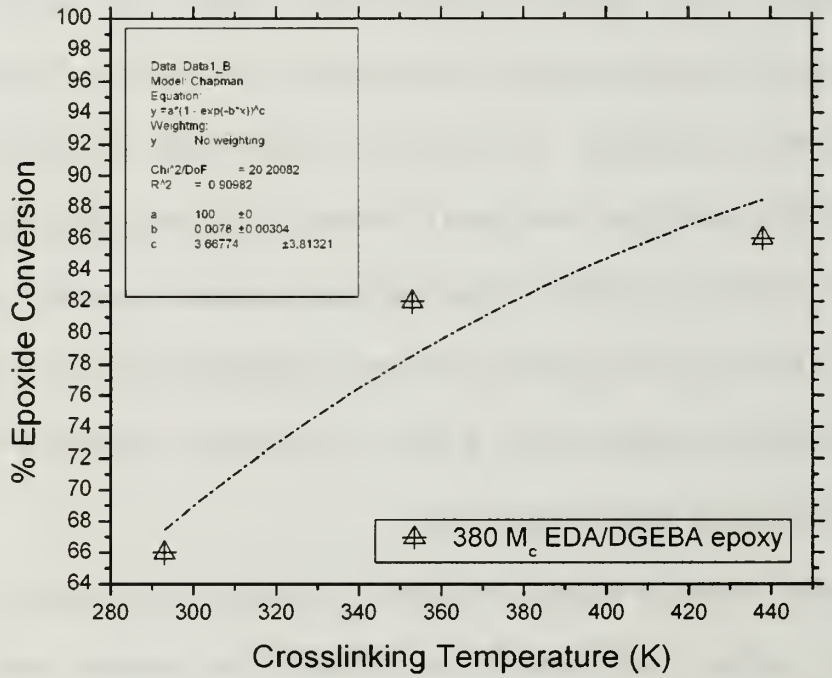

Figure 98: Curve fit of the epoxide conversion data from Table A-I

Eq. 1) $EC = 100(1 - e^{-bT})^c$

$b=0.0078; \quad c=3.667; \quad T=323\ K \quad \rightarrow EC \approx 72$

APPENDIX B: ESTIMATE OF NOMINAL M_C 380 G/MOL NETWORK BULK PROPERTIES FROM T_G

The work of Crawford and Lesser [156] and Calzia and Lesser [158,161] correlating the compressive yield stress of EDA/DMEDA/DGEBA networks to their glass transition temperature has been used to estimate the yield stress of the partially cured nominal 380 g/mol M_c and 818 g/mol M_c networks. The highest temperature seen during the crosslinking reaction was 50 C (323 K) and the resulting networks would exhibit a glass transition near this temperature.

Figure 99 shows a plot and curve fit to the compressive yield stress-T_g correlation measured by Crawford and Lesser using equation 1. Assuming a 323 K glass transition for the partially cured EDA/DMEDA/DGEBA networks, the curve fit of this data indicates a compressive yield stress of ~ 55 MPa. Inspection of similar data collected by Lesser and Calzia and presented as a plot of T_{test}/T_g vs compressive yield stress in reference indicates the compressive yield stress of the 323 T_g network to be ~47 MPa. σ_{cy} for the partially cured networks is then estimated at 47-55 MPa.

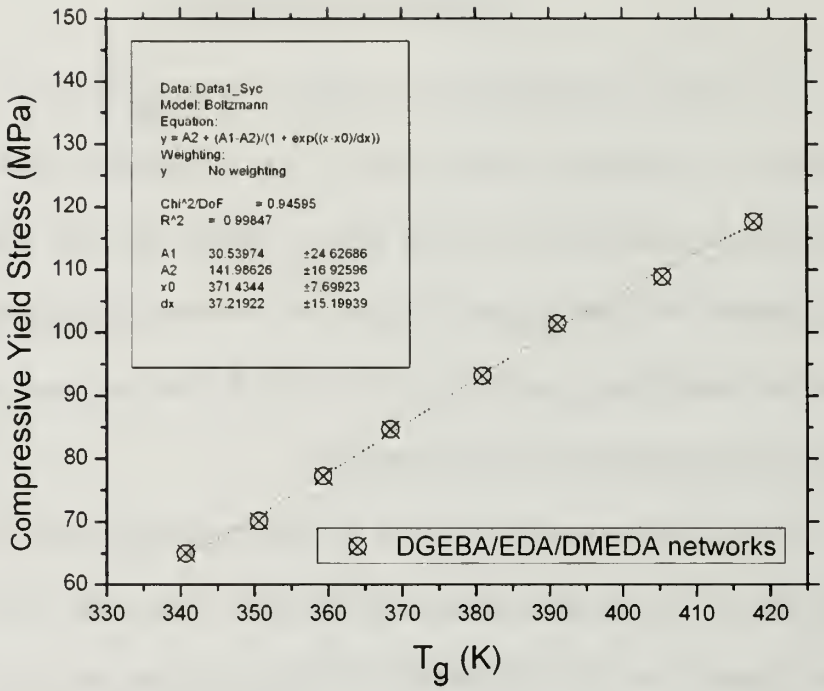

Figure 99: Correlation of compressive yield stresses and glass transition temperatures for a series of EDA/DMEDA/DGEBA networks with varying crosslink densities [156,158,161].

Eq. 1) $$\sigma_{cy} = \frac{A_1 - A_2}{1 + e^{(T_g - x_o)/dx}} + A_2$$

T_g=323 K; A_1=30.539; A_2=141.986; x_o=370.4; dx=37.219

APPENDIX C: FRACTURE ENERGY AND STABILITY CRITERION FOR FOUR POINT BEND TEST

Four Point Bend test

The Four Point Bend testing geometry (FPB) has been extensively used in the microelectronics industry to test the fracture properties of laminates composed of thin layers of metals, polymers and metal oxides. The test has been well described in the work of Charalambides et. al. [167] and Dauskardt [168]. The specimen configuration is illustrated below in Figure 100. The specimen consists of two stiff adherends with a polymer interlayer. One of the adherends is notched at the midpoint and a pre-crack is incorporated using a release film to ensure that the crack propagates at the adherend-polymer interface. Load is applied at the ends of the beam and at a distance s from each end to propagate the crack. The specimen may be loaded, the crack propagated and unloaded in a cyclic manner to allow multiple measurements of G_c on each sample.

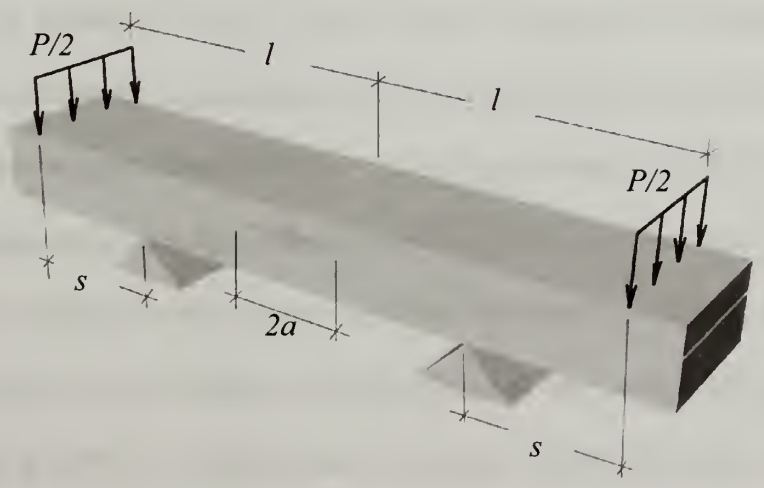

Figure 100: Four Pont Bend Test specimen consisting of two stiff adherends separated by a polymer interlayer. One of the adherends is notched at the midpoint and a pre-crack is incorporated using a release film.

Figure 101 shows a free-body diagram and moment diagram for the FPB specimen. The fracture energy is calculated from the load-displacement relationship. The total bending energy, load-displacement relationship and system compliance C_{XII} are calculated as in equations 7 through 9 and expressions for plane strain and plane stress fracture energy are given as equations 10 and 11. Because the moment in the region $s<x<2l-s$ is constant the change in compliance of the beam with crack length is a constant so long as the crack is within the range of $s<x<2l-s$.

The stability of this constant load experimental geometry can be assessed by evaluating the second derivative of the expression describing the Griffith's free energy of the system with respect to the surface area created. The result is given in equation 11b and it indicates that the system is in neither in a local energy minima or maxima but at a constant potential.

The resulting system allows stable propagation of cracks under constant load. The technique is also experimentally convenient because the crack length a need not be measured to determine fracture energy. Since the change in system compliance with crack length is constant for a crack propagating in the region $s<x<2l-s$ the value of G is independent of crack length and can be calculated from the specimen geometry and load P alone. However, because there are two crack fronts propagating simultaneously, care must be taken with the test fixture to ensure that the points of contact at both the beam ends and points s are in parallel planes, else there will be unequal curvature of the beam and each crack will be propagate unequally due to differing potentials. In addition, the existence of two crack fronts and translating in opposite directions makes imaging of the stress field around the crack tips difficult.

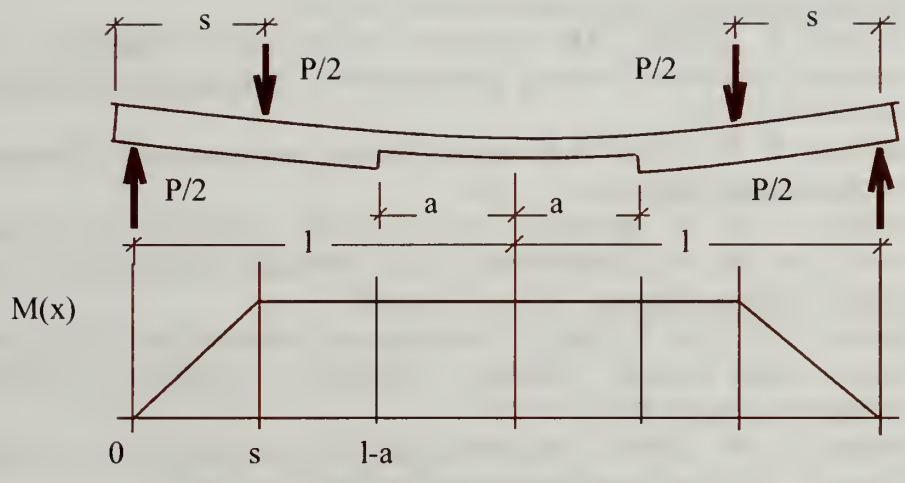

Figure 102: Free body diagram and bending moment diagram of Four Point Bend Test specimen.

Eq 7) $$\frac{1}{2}(U_o + U_c) = \frac{1}{2EI_o}\int_0^s \left(\frac{Px}{2}\right)^2 dx + \frac{1}{2EI_o}\int_s^{l-a} \left(\frac{Ps}{2}\right)^2 dx + \frac{1}{2EI_c}\int_{l-a}^{l} \left(\frac{Ps}{2}\right)^2 dx$$

Eq. 8) $$C_{XH} = \frac{\Delta_{XH}}{P} = \frac{-s^2}{6EI_cI_o}\{2I_cs + 3[a(I_c - I_o) - lI_c]\}$$

Eq. 9) $$\frac{\partial C}{\partial a} = \frac{s^2(I_o - I_c)}{2EI_cI_o}$$

Eq. 10) $$G_c = \frac{P^2s^2}{4Eb}\frac{(I_o - I_c)}{I_oI_c}$$ plane stress

Eq. 11) $$G_c = \frac{P^2s^2(1-\nu^2)}{4Eb}\frac{(I_o - I_c)}{I_oI_c}$$ plane strain

Eq 12) $$\frac{\partial^2 \Im}{\partial \Sigma^2} = -\frac{\partial^2 \pi}{\partial \Sigma^2} = -\frac{P^2}{2b}\left(\frac{\partial^2 C}{\partial a^2}\right) = 0$$ FPB at constant potential

BIBLIOGRAPHY

1. Jansen, J. A. (2006). "Ductile-to-brittle Transition of Plastic Materials." Advanced Materials & Processes 164(2): 39-42.
2. Altstadt, V. (2005). "The Influence of Molecular Variables on Fatigue Resistance in Stress Cracking Environments." Advances in Polymer Science 188(17): 105-102.
3. Kambour, R. P. (1973). "A Review of Crazing and Fracture in Thermoplastics." Macromolecular Reviews 7: 1-148.
4. Jacques, C. H. M., Wyzgoski, M. G. (1979). "Prediction of Environmental Stress Cracking of Polycarbonate From Solubility Considerations." Journal of Applied Polymer Science 23(4): 1153-1166.
5. Hansen, C. M., Just, L. (2001). "Prediction of Environmental Stress Cracking in Plastics With Hansen Solubility Parameters." Industrial & Engineering Chemistry Research 40(1): 21-25.
6. Hansen, C. M. (2002). "On Predicting Environmental Stress Cracking in Polymers." Polymer Degradation and Stability 77(1): 43-53.
7. Gent, A. N. (1970). "Hypothetical Mechanism of Crazing in Glassy Plastics." Journal of Materials Science 5(11): 925-932.
8. Percha, P. A., Yeakle., D. S. (1989). "The Materials Science and Engineering of Rigid-Rod Polymers." Materials Research Society Symposium Proceedings 134: 307-312.
9. Denny, L. R., Goldfarb, I. J., Soloski, E. J. (1989). "Thermal Stability of Rigid Rod Polymers." Materials Research Society Symposium Proceedings 134: 395-406.
10. Kumar, S., Helminiak, T.E. (1989). "Compressive Strength of High Performance Fibers." Materials Research Society Symposium Proceedings 134: 363-374.
11. Krause, S. J., Haddock, T. B., Vezie, D. L., Lenhert, P. G., Hwang, W. F., Price, G. E., Helminiak, T. E., O'Brien, J. F., Adams, W. W. (1989). "Morphology and Properties of Rigid-rod Poly(p-phenylenebenzobisoxazole) (PBO) and Stiff-chain Poly(2,5(6)-benzoxazole) (ABPBO) fibers." Polymer 29(8): 1354-1364
12. Toyobo (2001). Technical Information PBO Fiber Zylon, Toyobo Co. LTD. 2005.
13. Martin, D. C., Thomas, E. L. (1988). "Morphology of Rigid-Rod Polymer Fibers: An Overview." Materials Research Society Symposium Proceedings 134: 415-430.
14. Shimamura, K. M., J. R., Thomas, E. L. (1983). "Lattice Imaging of High Modulus Poly(p-phenylene Benzobisthiazole) fibers." Journal of Materials Science Letters 2(2): 54-58.
15. Kitigawa, T., Murase, H., Yabuki, K. (1998). "Morphological Study on Poly- p-phenylenebenzobisoxazole (PBO) Fiber." Journal of Polymer Science: Part B: Polymer Physics, 36: 39–48.
16. Allen, S. R., Filippov, A. G., Farris, R. J., Thomas, E. L., Wong, C. P., Berry, G. C., Chenevey, E. C. (1981). "Mechanical Studies of High-Strength, High

Modulus Poly(p-phenylenebenzobisthiazole) Fibers." Macromolecules 14(4): 1135-1138.

17. Allen, S. R., Filippov, A. G., Farris, R. J., Thomas, E. L. (1981). "Macrostucture and Mechanical Behavior of Fiberss of Poly-p-phenylene benzobisthiazole." Journal of Materials Science 26(1): 291-301.
18. Pottick, L. A., Farris, R. J. (1985). "The Effect of Tension During Drying on the Structure and Mechanics of Poly(p-phenylene benzobisthiazole) Fibers." Polymer engineering and Science 25(5): 284-288.
19. DeTeresa, S. J., Porter, R. S., Farris, R. J., (1985). "A Model for the Compressive Buckling of Extended Chain Polymers." Journal of Materials Science 20(5): 1645-1659.
20. Frame, B. J., Hansen, J. G. R. (2002). "Fire Resistant Composite Materials For Energy Absorption Applications." International SAMPE Symposium 47(2): 542-555.
21. Savage, G. M. (1989). "Fabric and fiber-reinforced laminate armors." Metals and Materials 5(5): 285-290.
22. AP (2003). Company's Bulletproof Vests are Questioned. New York Times. New York: A37.
23. Holmes, G. A., Rice K., Snyder, C. R. (2006). "Ballistic Fibers: A Review of the Thermal, Ultraviolet and Hydrolytic Stability of the Benzoxazole Ring Structure." Journal of Materials Science 41(13): 4105-4116.
24. Walsh, P. J., Hu, X., Cunniff, P., Lesser, A. J. (2006). "Environmental Effects on Poly-p-phenylenebenzobisoxazole Fibers. I. Mechanisms of Degradation." Journal of Applied Polymer Science 102(4): 3517-3525.
25. Denny, L. R., Goldfarb, I. J., Soloski, E. J. (1989). "Thermal Stability of Rigid Rod Polymers." Materials Research Society Dymposium Proceedings 134: 395-406.
26. Bourbigot, S. (2001). "Thermal Degradation of Poly(p-phenylenebenzobisoxazole) and Poly(p-phenylenediamineterephthalamide) Fibres." Polymer International 50(1): 157 - 164.
27. Villar-Rodil, S. (2003). "Studies on the Thermal Degradation of Poly (p-phenylene benzobisoxazole)." Chemistry of Materials 15(21): 4052-4059.
28. Cohen, Y., Thomas, E. L. (1985). "Structure Formation During Spinning of Poly(p-phenylenebenzobisthiazole) Fiber." Polymer Engineering and Science 25(17): 1093-1096..
29. Cohen, Y., Thomas, E. L. (1988). "Microfibrillar Network of a Rigid Rod Polymer.1. Visualization by Electron Microscopy." Macromolecules 21(2): 433-435.
30. Cohen, Y., Thomas, E. L. (1988). "Microfibrillar Network of a Rigid Rod Polymer. 2. Small-angle X-ray Scattering." Macromolecules 21(2): 436-441
31. Morgan, R. J., Pruneda, C. O., Steele, W. J., (1983). "The Relationship between the Physical Structure and the Microscopic Deformation and Failure Processes of Poly(p-phenylene terephthalamide) Fibers." Journal of Polymer Science: Polymer Physics Edition 21(9): 1757-1783.
32. Morgan, R. J., Pruneda, C. O., Kong, F. M. (1984). "Aging Studies of Kevlar 49 Fibers." Polymer Preprints 25(1): 189-190.

33. Morgan, R. J., Pruneda, C. O. (1987). "The Characterization of the Chemical Impurities in Kevlar 49 Fibres." Polymer 28(2): 340-346.
34. Wang, S. G., P.; Wu, P.; Han, Z. (2004). "Supramolecular Regulation of Photophysical Properties and Electron Paramagnetic Resonance Studies of Novel Rod-Coil Ordered Copolymers Based on Poly(p-phenylene benzobisoxazole)." Macromolecules 37(10): 3815-3822.
35. Hull, D., Clyne, T. W. (1996). An Introduction to Composite Materials. Cambridge, Cambridge University Press.
36. Kovar, R. F., Haghighat, R. Lusignea, R. W. (1989). "Improvement of Compressive Strength In Ordered Polymer Films and fibers By Sol-Gel Glass Processing." Materials Research Society Symposium Proceedings 134: 389-394.
37. Haghighat, R. R., Kovar, R. f., Lisignea, R. W. (1988). "Poly[benzobisthiazole] (PBT)/sol-gel microcomposites." Materials Research Society Symposium Proceedings 121(3): 755-760.
38. Hwang, C. R., Malone, M. F., Farris, R. J., Martin, D. C., Thomas E. L (1991). "In-situ Network Composite Fibres of PBZT With Nylon." Journal of Materials Science 26: 2635-2371.
39. Hwang, C. R., Malone, M. F., Farris, R. J. (1988). "Processing and Properties of Poly(p-pehenylenebenzobisthiazole) (PBT)/Nylon Composite Fibers." Polymeric Materials Science 59: 440-444.
40. Farris, R. J., Cohen, Y., Deteresa, S. J. (1989). US Pat # 4,842,924. Novel Compositions Based on Reinforcement With Microfibrillar Networks of Rigid Rod Polymers. United States, Farris et al.
41. Jenkins, S., Jacob, K. I., Polk, M. B., Kumar, S., Dang, T. D., Arnold, F. E. (2000). "Reaction Induced Strain in Rigid-rod Polymeric Fibers." Macromolecules 33: 9060-9068.
42. Sweeny, W. (1992). "Improvements in Compressive Properties of High-Modulus Fibers by Crosslinking." Journal of Polymer Science, Part A: Polymer Chemistry 30(6): 1111-1122.
43. Dauskardt, R. H. L., M.; Ma, Q.; Krishna, N. (1998). "Adhesion and Debonding of Multi-layer Thin Film Structures." Engineering Fracture Mechanics 61(1): 141-162.
44. Bascom, W. D., Cottington, R. L., Jones, R. L., Peyser, P. (1975). "The Fracture of Epoxy-and Elastomer-Modified Epoxy Polymers in Bulk and as Adhesives." Journal of Applied Polymer Science 19(9): 2545-2562.
45. Hunston, D. L., Kinloch, A. J., Wang, S. S. (1981). "The Fracture Resistance of a Toughened Epoxy Adhesive." Journal of Adhesion 12: 59-77.
46. Hunston, D. L., Kinloch, A. J., Wang, S. S. (1989). "Micromechanics of Fracture in Structural Adhesive Bonds." Journalof Adhesion 28: 103-114.
47. Ikeda, T., Yamashita, A., Lee, D, Miyazaki, N. (2000). "Failure of a Ductile Adhesive Constrained by Hard Adherends." Journal of Engineering Materials and Technology 122: 80-85.
48. Pardoen, T. F., T.; Landis, C. M.; Delannay, F. (2005). "Constraint Effects in Adhesive Joint Fracture." Journal of The Mechanics and Physics of Solids 53: 1951-1983.

49. Gent, A. N. (1970). "Hypothetical Mechanism of Crazing in Glassy Plastics." Journal of Materials Science 5(11): 925-932.
50. Raman, A., Farris, R. J., Lesser, A. J. (2001). "Environmental Stress Cracking in Polycarbonate - Developing a Theory." Polymeric Materials: Science & Engineering 85: 632-633.
51. Kambour, R. P. (1973). "A Review of Crazing and Fracture in Thermoplastics." Macromolecular Reviews 7: 1-148.
52. Moskala, E. J. (1989). "A Fracture Mechanics Approach to Environmental Stress Cracking in Poly(ethylene terephthalate)." Polymer Degradation and Stability 39(3): 675-680.
53. Kefalas, V. A. (1995). "Solvent Crazing as a Stress-Induced surface Adsorption and Bulk Plasticization Effect." Journal of Applied Polymer Science 58(4): 711-717.
54. Bandyopadhyay, S., Brown, H. R. (1981). "Studies of Environmental Stress-Crack Propagation in Low Density Polyethylene." Journal of Polymer Science 19(5): 749-761.
55. Bernier, G. A., Kambour, R. P. (1968). "The Role of Organic Agents in the Stress Crazing and Cracking of Poly(2,6-dimethyl-1,4-phenylene oxide)." Macromolecules 1(5): 393-400.
56. Kambour, R. P., Romagosa, E. E., Gruner, C. L. (1972). "Swelling, Crazing and Cracking of an Aromatic Copolyether-Sulfone in Organic Media." Macromolecules 5(4): 335-340.
57. Kambour, R. P. G., C. L., Romagosa, E. E. (1974). "Bisphenol-A Polycarbonate Immersed in Organic Media Swelling and Response to Stress." Macromolecules 7(2): 248-253.
58. Jacques, C. H. M., Wyzgoski, M. G. (1979). "Prediction of Environmental Stress Cracking of Polycarbonate From Solubility Considerations." Journal of Applied Polymer Science 23(4): 1153-1166.
59. Hansen, C. M., Just, L. (2001). "Prediction of Environmental Stress Cracking in Plastics With Hansen Solubility Parameters." Industrial & Engineering Chemistry Research 40(1): 21-25.
60. Hansen, C. M. (2002). "On Predicting Environmental Stress Cracking in Polymers." Polymer Degradation and Stability 77(1): 43-53.
61. Arnold, J. C. (1995). "Craze Initiation During the Environmental Stress Cracking of Polymers." Journal of Materials Science 30(3): 655-660.
62. Kawagoe, M., Kitigawa, M (1987). "Craze Initiation in Poly(methyl methacrylate) Exposed to n-Alkanes." Journal of Materials Science 22(8): 3000-3004.
63. Kawagoe, M., Morita, M (1993). "Fatigue Failure of Poly(methyl methacrylate) in Alcohol Environments." Journal of Materials Science 28(9): 2347-2352.
64. Sternstein, S. S., Ongchin, L. (1969). "Yeild Criteria for Plastic Deformation of Glassy High Polymers in General Stress Fields." ACS Polymer Preprints 10(2): 1117-1124.
65. Oxborough, R. J., Bowden, P. B. (1973). "A General Critical-Strain Criterion for Crazing in Glassy Polymers." Philosophical Magazine 28(3): 547-559.

66. Flory, P. J. (1953). Principles of Polymer Chemistry. Ithaca, New York, Cornell University Press: p576.
67. Flory, P. J. (1979). "The Elastic Free Energy of Dilation of a Network." Macromolecules 12(1): 119-122.
68. Barton, A. F. M. (1975). "Solubility Parameters." Chemical Reviews 75(6): 731-754.
69. Altstadt, V. (2005). "The Influence of Molecular Variables on Fatigue Resistance in Stress Cracking Environments." Advances in Polymer Science 188(17): 105-102.
70. Caskey, T. & Lesser, A. J. (2004). unpublished work at the University of Massachusetts, Dept. of Polymer Science & Engineering. Amherst, Ma.
71. Kwok, D. Y. (1999). Surface Characterization Methods. Surfactant Science Series. New York, Marcel Dekker. 87: 37-50.
72. Johnson, K. L. (1971). "Surface Energy and the Contact of Elastic Solids." Proceedings of the Royal Society of London: Series A: Mathematical and Physical Sciences 324: 301-313.
73. Schull, K. R. A., D.; Chen, W; Flanigan, C. M; Crosby, A. J. (1998). "Axisymetric Adhesion Tests of Soft Materials." Macromolecular Chemical Physics 199(4): 489-511.
74. Tirrel, M. (1996). "Measurement of Interfacial Energy at Solid Polymer Surfaces." Langmuir 12(19): 4548-4551.
75. Schull, K. R., Crosby, A. J. (1999). "Adhesive Failure Analysis of Pressure Sensitive Adhesives." Journal of Polymer Science: Part B 37(24): 3455-3472.
76. Maugis, D. (1978). "Fracture Mechanics and The Adherence of Viscoelastic Bodies." Journal of Physics B: Applied Physics 11: 1989-2023.
77. Crank, J. (1976). The Mathematics of Diffusion. New York, Oxford University Press, p239.
78. Mandel, J. (1964). The Statistical Analysis of Experimental Data. New York, John Wiley & Sons. p74.
79. de Gennes, P. G. (1985). "Wetting: Statics and Dynamics." Reviews of Modern Physics 57(3): 827-863.
80. Turnbull, A., Maxwell, A. S. (1999). "Test Methods for Environmental Stress Cracking of Polymer Materials." National Physical Laboratory Technical Review No. 3: p21.
81. Percha, P. A., Yeakle., D. S. (1989). "The Materials Science and Engineering of Rigid-Rod Polymers." Materials Research Society Symposium Proceedings 134: 307-312.
82. Denny, L. R., Goldfarb, I. J., Soloski, E. J. (1989). "Thermal Stability of Rigid Rod Polymers." Materials Research Society Symposium Proceedings 134: 395-406.
83. Kumar, S., Helminiak, T.E. (1989). "Compressive Strength of High Performance Fibers." Materials Research Society Symposium Proceedings 134: 363-374.
84. Krause, S. J., Haddock, T. B., Vezie, D. L., Lenhert, P. G., Hwang, W. F., Price, G. E., Helminiak, T. E., O'Brien, J. F., Adams, W. W. (1989). "Morphology and

Properties of Rigid-rod Poly(p-phenylenebenzobisoxazole) (PBO) and Stiff-chain Poly(2,5(6)-benzoxazole) (ABPBO) fibers." Polymer 29(8): 1354-1364.
85. Toyobo (2001). Technical Information PBO Fiber Zylon, Toyobo Co. LTD. 2005.
86. AP (2003). Company's Bulletproof Vests are Questioned. New York Times. New York: A37.
87. Wolfe, J. F., Arnold, F. E. (1981). "Rigid Rod Polymers. 1. Synthesis and Thermal Properties of Para-Aromatic Polymers with 2,6-Benzobisoxazole Units in the Main Chain." Macromolecules 14: 909-915
88. Cohen, Y., Thomas, E. L. (1985). "Structure Formation During Spinning of Poly(p-phenylenebenzobisthiazole) Fiber." Polymer Engineering and Science 25(17): 1093-1096.
89. Martin, D. C., Thomas, E. L. (1988). "Morphology of Rigid Rod Polymers: An Overview." Materials Research Society Symposium Proceedings 134: 415-429.
90. Cohen, Y., Thomas, E. L. (1985). "Structure formation during spinning of poly(p-phenylenebenzobisthiazole) fiber." Polymer Engineering and Science 25(17): 1093-1096.
91. Cohen, Y., Thomas, E. L. (1988). "Microfibrillar network of a rigid rod polymer.1. Visualization by electron microscopy." Macromolecules 21(2): 433-435.
92. Fratini, A. V., Galen-Lenhert, P., Resch, T. J., Adams, W. W. (1989). "Molecular Packing and Crystalline Order in Polybenzobisoxazole and Polybenzobisthiazole Fibers." Materials Research Society Symposium Proceedings 134: 431-445.
93. Pottick, L. A. (1986). Ph.D. Thesis: The influence of Drying on the Structure and Mechanics of Poly (p-phenylenebenzobisthiazole) Fibers. Polymer Science and Engineering. Amherst, University of Massachusetts.
94. Pottick, L. A. (1985). "The Effect of Tension During Drying on the Structure and Mechanics of Poly(p-phenylene benzobisthiazole) Fibers." Polymer Engineering Science 25(5): 284-288.
95. Kitigawa, T. M., H.; Yabuki, K. (1998). "Morphological Study on Poly- p-phenylenebenzobisoxazole (PBO) Fiber." Journal of Polymer Science: Part B: Polymer Physics, 36: 39–48.
96. Minter, J. R. (1982). Ph.D. Thesis: Structure Investigation of Fibers and Films of poly (p-phenylene-benzobisthiazole). Polymer Science & Engineering. Amherst, University of Massachusetts Amherst.
97. Minter, J. R., Shimamura, K., Thomas, E. L. (1981). "Microstuctural Study of As-Extruded and Heat Treated Ribbons of Poly(p-phenylenebenzobisthiazole)." Journal of Materials Science 16(12): 3303-3308.
98. Walsh, P. J., Hu, X., Cunniff, P., Lesser, A. J. (2006). "Environmental Effects on Poly-p-phenylenebenzobisoxazole Fibers. I. Mechanisms of Degradation." Journal of Applied Polymer Science 102(4): 3517-3525.
99. Walsh, P. J., Hu, X., Cunniff, P., Lesser, A. J. (2006). "Environmental Effects on Poly-p-phenylenebenzobisoxazole Fibers. II. Attempts at Stabilization." Journal of Applied Polymer Science 102(4): 3819-3829.

100. Berry, G. C., Metzger, P. C., Venkatraman, P., Cotts, D. B (1979). "Polymer Preprint." ACS 20: 42-44.
101. Metzger, P. C. (1980). PhD. Thesis: Effects of Aggregation and Electrostatic Repulsions on Solution properties of Flexible and Rodlike Polymer. Pittsburgh, Carnegie-Mellon University.
102. Ying-Hung, S., Martin, S. J., Owen, K., Smith, P. B., Karas, C. L. (1999). "A Study of Benzobisoxazole and Benzobisthiazole Compounds and Polymers Under Hydrolytic Conditions." Journal of Polymer Science:Part A 37(14): 2637-2643.
103. Venkatasubramanian, N., Polk, M. B., Kumar, S., Gelbaum, L. T. (1993). "Structural Investigations on Lewis Acid Mediated Solubilization of Poly(p-phenylenebenzobisthiazole) in an Aprotic Solvent." Journal of Polymer Science, Part B: Polymer Physics 31(13): 1965-1973.
104. Bourbigot, S. F., X.; Duquesne , S. (2001). "Thermal degradation of poly(p-phenylenebenzobisoxazole) and poly(p-phenylenediamineterephthalamide) fibres." Polymer International 50(1): 157-164.
105. Wang, S. G., P.; Wu, P.; Han, Z. (2004). "Supramolecular Regulation of Photophysical Properties and Electron Paramagnetic Resonance Studies of Novel Rod-Coil Ordered Copolymers Based on Poly(p-phenylene benzobisoxazole)." Macromolecules 37(10): 3815-3822.
106. Morgan, R. J., Pruneda, C. O., Steele, W. J., (1983). "The Relationship between the Physical Structure and the Microscopic Deformation and Failure Processes of Poly(p-phenylene terephthalamide) Fibers." Journal of Polymer Science: Polymer Physics Edition 21(9): 1757-1783.
107. Morgan, R. J., Pruneda, C. O., Kong, F. M. (1984). "Aging Studies of Kevlar 49 Fibers." Polymer Preprints 25(1): 189-190.
108. Morgan, R. J., Pruneda, C. O. (1987). "The Characterization of the Chemical Impurities in Kevlar 49 Fibres." Polymer 28(2): 340-346.
109. ASTM (1989). "D 3379-75: Standard Test Method for Tensile Strength and Young's Modulus for High-Modulus single-Filament Materials." pp818-822.
110. ASTM (2003). "C 1557-03: Standard Test Method for Tensile Strength and Young's Modulus of Fibers." pp793-802.
111. Shioya, M. T., A., (1985). "Characterization of microvoids in carbon fibers by absolute small-angle x-ray measurements on a fiber bundle." Journal of Applied Physics 58(11): 4074-4082.
112. Villar-Rodil, S. T.-M., K.; Paredes, J. I.; Martinez-Alonso, A.; Tascon, J. M. D. (2003). "Studies on the Thermal Degradation of Poly (p-phenylene benzobisoxazole)." Chemistry of Materials 15(21): 4052-4059.
113. Walsh, P. J., Hu, X., Cunniff, P., Lesser, A. J. (2006). "Environmental Effects on Poly-p-phenylenebenzobisoxazole Fibers. I. Mechanisms of Degradation." Journal of Applied Polymer Science 102(4): 3517-3525.
114. Wang, S. G., P.; Wu, P.; Han, Z. (2004). "Supramolecular Regulation of Photophysical Properties and Electron Paramagnetic Resonance Studies of Novel Rod-Coil Ordered Copolymers Based on Poly(p-phenylene benzobisoxazole)." Macromolecules 37(10): 3815-3822.

115. Walsh, P. J., Hu, X., Cunniff, P., Lesser, A. J. (2006). "Environmental Effects on Poly-p-phenylenebenzobisoxazole Fibers. II. Attempts at Stabilization." Journal of Applied Polymer Science 102(4): 3819-3829.
116. Cooper, A. I. (2000). "Polymer synthesis and processing using supercritical carbon dioxide." Journal of Materials Chemistry 10: 207-234.
117. Allen, N. S. and M. Edge (1992). Fundamentals of Polymer Degradation and Stabilization. London:New York, Elsevier Applied Science.
118. Davis, A. and D. Sims (1983). Weathering of polymers. London; New York, Elsevier Applied Science.
119. Allen, N. S. (2004). "Degradation and stabilisation of polymers and coatings: nano versus pigmentary titania particles." Polymer Degradation and Stability 85: 927-946.
120. Allen, N. S. (2001). "Studies of synergism between carbon black and stabilizers in LDPE photodegradation." Polymer Degradation and Stability 72(2): 259-270.
121. Pajonk, G. M. (2002). "Chemistry of Aerogels and Their Applications." Chemical Reviews 102: 4243-4265.
122. Xin, J. H., Daoud, W. A., Kong, Y. Y. (2004). "A New Approach to UV-Blocking Treatment for Cotton Fabrics." Textile Research Journal 74(2): 97-100.
123. Daoud, W. A., Xin, J. H. (2004). "Low Temperature Sol-Gel Processed Photocatalytic Titania Coating." Journal of Sol-Gel Science and Technology 29(1): 25-29.
124. Kitigawa, T., Murase, H., Yabuki, K. (1998). "Morphological Study on Poly- p-phenylenebenzobisoxazole (PBO) Fiber." Journal of Polymer Science: Part B: Polymer Physics, 36: 39–48.
125. Martin, D. C., Thomas, E. L. (1989). The Materials Science and Engineering of Rigid-Rod Polymers. Materials Research Society Symposium Proceedings.
126. Holdaway, H. W. and M. S. Robinson (1965). Journal of the Textile Institute 56: 168.
127. Landstrett, C. B., P. R. Ewald, et al. (1957). Journal of the Textile Institute 27: 486.
128. Kovar, R. F., Haghighat, R. Lusignea, R. W. (1989). "Improvement of Compressive Strength In Ordered Polymer Films and fibers By Sol-Gel Glass Processing." Materials Research Society Symposium Proceedings 134: 389-394.
129. Haghighat, R. R., Kovar, R. f., Lisignea, R. W. (1988). "Poly[benzobisthiazole] (PBT)/sol-gel microcomposites." Materials Research Society Symposium Proceedings 121(3): 755-760.
130. Hwang, C. R., Malone, M. F., Farris, R. J., Martin, D. C., Thomas E. L (1991). "In-situ Network Composite Fibres of PBZT With Nylon." Journal of Materials Science 26: 2635-2371.
131. Hwang, C. R., Malone, M. F., Farris, R. J. (1988). "Processing and Properties of Poly(p-pehenylenebenzobisthiazole) (PBT)/Nylon Composite Fibers." Polymeric Materials Science 59: 440-444.
132. Farris, R. J., Cohen, Y., Deteresa, S. J. (1989). US Pat # 4,842,924. Novel Compositions Based on Reinforcement With Microfibrillar Networks of Rigid Rod Polymers. United States, Farris et al.

133. Jenkins, S., Jacob, K. I., Polk, M. B., Kumar, S., Dang, T. D., Arnold, F. E. (2000). "Reaction Induced Strain in Rigid-rod Polymeric Fibers." Macromolecules 33: 9060-9068.
134. Sweeny, W. (1992). "Improvements in Compressive Properties of High-Modulus Fibers by Crosslinking." Journal of Polymer Science, Part A: Polymer Chemistry 30(6): 1111-1122.
135. Cassidy, P. E. (2003). "New Poly(silanes-siloxanes) via Hydrosilation in Super Critical CO_2 and Subsequent Crosslinking." Macromolecular Symposia 192: 115-121.
136. Toyobo (2001). Technical Information PBO Fiber Zylon, Toyobo Co. LTD. 2005.
137. Calzia, K. J. (2006). Ph.D Thesis: Molecular Aspects of Yield and Fracture in Glassy Thermosets and Their Nano-Composites. Dept. of Polymer Science & Engineering. Amherst, University of Massachusetts.
138. Allen, S. R., Filippov, A. G., Farris, R. J., Thomas, E. L., Wong, C. P., Berry, G. C., Chenevey, E. C. (1981). "Mechanical Studies of High-Strength, High Modulus Poly(p-phenylenebenzobisthiazole) Fibers." Macromolecules 14(4): 1135-1138.
139. Hunt, s. M., Graeme, A. G. (2000). "Characterization of Siloxane Residues From Polydimethylsiloxane Elastomers by MALDI-TOF-MS." Polymer International 49: 633-635.
140. Hunston, D. L., Kinloch, A. J., Wang, S. S. (1981). "The Fracture Resistance of a Toughened Epoxy Adhesive." Journal of Adhesion 12: 59-77.
141. Bascom, W. D., Cottington, R. L., Jones, R. L., Peyser, P. (1975). "The Fracture of Epoxy-and Elastomer-Modified Epoxy Polymers in Bulk and as Adhesives." Journal of Applied Polymer Science 19(9): 2545-2562.
142. Wang, S .S., Mandel, J. F., McGarry, F. J. (1978). "An Analysis of the Crack Tip Stress Field in DCB Adhesive Fracture Specimens" International Journal of Fracture 14:39-58.
143. Bascom, W. D., Cottington, R. L. (1976). "Effect of Temperature on the Adhesive Fracture Behavior of an Elastomer-Epoxy Resin" Journal of Adhesion. 7:333-346.
144. Kinloch, A. J., Thrusabanjong, Williams, J. G. (1991). " Fracture at Bi-material Interfaces: The Role of Residual Stresses." Journal of Materials Science 26: 6260-6270.
145. Kinloch, A. J., (1987). Adhesion and Adhesives: Science and Technology. New York, Chapman & Hall.
146. Parker, A. P. (1981). The Mechanics of Fracture and Fatigue. New York, E. F. & N. Spon LTD.
147. Hertzberg, R. W. (1996). Deformation and Fracture Mechanics of Engineering Materials. New York, John Wiley & Sons Inc.
148. Wrublewski, D. & Lesser, A. J. (2004). unpublished work at the University of Massachusetts, Dept. of Polymer Science & Engineering. Amherst, Ma.
149. ASTM D3762-03 Standard Test Method for Adhesive-Bonded Surface Durability of Aluminum (Wedge Test).

150. Hunston, D. L., Kinloch, A. J., Wang, S. S. (1989). "Micromechanics of Fracture in Structural Adhesive Bonds." Journalof Adhesion 28: 103-114.
151. Ikeda, T., Yamashita, A., Lee, D, Miyazaki, N. (2000). "Failure of a Ductile Adhesive Constrained by Hard Adherends." Journal of Engineering Materials and Technology 122: 80-85
152. Roche, A. A., Bouchet, A., Bentadjine, S. (2002). "Formation of Epoxy Diamine-Metal Interphases." International Journal of Adhesives and Adhesion 22: 431-441.
153. Cody, R. S. Lesser, A. J. (1997) "Deformation and Yield of Epoxy Networks in Constrained States of Stress." Journal of Materials Science. 32:5637-5643.
154. Cody, R. S. Lesser, A. J. (1997) "A generalized model for the yield behavior of epoxy networks in multiaxial stress states." Journal of Polymer Science: Part B. 35:1611-1619.
155. Crawford, E, Lesser, A. J. (1997). "The Role of Network Architecture on the Glass Transition Temperature of Epoxy Resins." Journal of Applied Polymer Science 66:387-395.
156. Crawford, E., Lesser, A. J. (1998). "The Effect of Network Architecture on the Thermal and Mechanical Behavior of Epoxy Resins." Journal of Polymer Science Part B 36:1371-1382.
157. Crawford, E., Lesser, A. J. (1999) "Brittle to Ductile: Fracture Toughness Mapping on Controlled Epoxy Networks." Polymer Engineering and Science 39:385-392.
158. Calzia, K., Lesser, A. J., (2004). "Molecular Parameters Governing the Yield Response of Epoxy-Based Glassy Networks." Journal of Polymer Science: Part B. 42:2050-2056.
159. Dugdale, D. S. (1960). "Yeilding of Steel Sheets Containing Slits." Journal of the Mechanics and Physics of Solids 8(2): 100-108.
160. Barenblatt, G. I. (1962). "The Mathematical Theory of Equilibrium Cracks in Brittle Fracture." Advances in Applied Mechanics 7: 55-129.
161. Calzia, K. J. (2006). Ph.D Thesis: Molecular Aspects of Yield and Fracture in Glassy Thermosets and Their Nano-Composites. Dept. of Polymer Science & Engineering. Amherst, University of Massachusetts.
162. Detwiler, A. & Lesser, A. J. (2007). unpublished work at the University of Massachusetts, Dept. of Polymer Science & Engineering. Amherst, Ma.
163. Prolongo, S. G., Mikes, F. Cabanelas, J. C., Paz-Abuin, S., Baselga, J. (2003) "Diffusion Control on the Cure Kinetics of DGEBA with Ethylenediamines." Journal of Materials Processing Technology. 143: 546-550.
164. Dally, J. W. (1991). Experimental Stress Analysis. New York, McGraw Hill. P429, p435.
165. Dally, J. W.; Sanford, R. J. (1978). "Classification of Stress Intensity Factors From Isochromatic Fringes." Experimental Mechanics 18(12): 441-448.
166. Griffith, M., (1921). "The Phenomena of Rupture and Flow in Solids." Philosophical Transactions of the Royal Society of London: Series A 221:163-198.

167. Charalambides, P. G. L., J.; Evans, A. G.; McKeeking, R. M (1989). "A Test Specimen for Determining the Fracture Resistance of Bi-material Interfaces." Journal of Applied Mechanics 56(3): 77-82.
168. Dauskardt, R. H. L., M.; Ma, Q.; Krishna, N. (1998). "Adhesion and Debonding of Multi-layer Thin Film Structures." Engineering Fracture Mechanics 61(1): 141-162.